NUMERICAL MODELING OF SLOSHING USING THE RADIAL BASIS FUNCTION COLLOCATION METHOD

by

Kerem R. Çakıroğlu

B.S., Civil Engineering, Bogazici University, 2010

Submitted to the Institute for Graduate Studies in
Science and Engineering in partial fulfillment of
the requirements for the degree of
Master of Science

Graduate Program in Computational Science and Engineering

Boğaziçi University

2012

to Dr. Ömer Lütfü Çakıroğlu

and Ayşe Çakıroğlu

ACKNOWLEDGEMENTS

I would like to express my most sincere gratitude to my thesis supervisor, Osman Börekçi and co-advisor, Sami And Kılıç for introducing me to the exciting world of numerical modeling and computer aided engineering. I would also like to thank for their guidance, support and encouragement throughout the development of this thesis.

I would like to thank the committee members for their support and valuable comments.

I am also thankful to all my friends in the Civil Engineering department, including Ayşe Aydın, Ceki Erginbaş, Cenk Güngör, Ekin Özer, and Yavuz Tokmak.

And finally, I would like to thank Yasemin Doğrul for her endless support and patience throughout my studies.

ABSTRACT

A series of numerical models have been developed to study sloshing in 2D and 3D Rigid Tanks. The problem is approached with Potential Flow Theory and Laplace's equation is solved with Neumann type lateral and bottom boundary conditions and with Dynamic and Kinematic free surface boundary conditions. For the numerical method to solve the initial-boundary value problem; Meshless Radial Basis Function Collocation Method is used and a predictor-corrector type time marching scheme is used with Adams-Bashworth predictors and Adams-Moulton correctors. The 2D models were verified by performing some numerical tests and comparing the results with available second or third order asymptotic analytical formulae from the literature, numerical experiments from the literature, and with lab experiments from the literature. For the 3D models, linear analytic formulae were used for verification. The results were supported with laboratory experiments, and by employing another numerical model developed using the Virtual Mass technique. Fully nonlinear boundary conditions with deformable boundaries have been used in the 2D sloshing models. The numerical tanks have been tested with linear standing wave, lateral excitation, vertical excitation and combined lateral and vertical excitation inputs. Fast convergence and excellent accuracy is obtained for the low amplitude test cases. For the high amplitude sloshing cases, some experimental techniques are used and a good accuracy is achieved. For the 3D sloshing studies, linearized mathematical formulation was used; and the RBFCM, Virtual Mass, and the Laboratory Experiment models were benchmarked by demonstrating their performances in estimating the sloshing mode shape frequencies. Finally, a sample tank from the industry was analyzed by applying real earthquake motions using the RBFCM and Virtual Mass models, and the calculated maximum wave amplitudes were compared. The numerical experiments show that the models created in this study may be utilized for the research on the optimum tank design; which may eventually lead to improvements on the design code.

ÖZET

RİJİT TANKLARDAKİ ÇALKALANMANIN RADYAL TABANLI FONKSİYON KOLOKASYON YÖNTEMİ İLE SAYISAL MODELLENMESİ

Bu çalışmada kap içerisinde bulunan sıvıların çalkalanma hareketleri incelenmiştir. Rijit tanklar ele alınmış, ve sıvı davranışı ağsız radial tabanlı fonksiyon kolokasyon yöntemi (RBFCM) ile sayısal olarak modellenmiştir. Çalışmada öncelikle iki boyutlu tanklar incelenmiş, potansiyel akış teorisi kullanılarak çevirisiz, sıkıştırılamaz akış için Laplace denklemi doğrusal olmayan yüzey sınır şartları ile birlikte çözülmüştür. Tank içindeki sıvının yanal, dikey ve yanal ve dikey birlikte sarsılma altındaki hareketleri incelenmiş, ve literatürdeki çözümsel, sayısal, ve deneysel sonuçlar ile kıyaslanmıştır. Küçük ve orta genlikteki dalgalar için çok iyi sonuçlar elde edilmiştir, büyük genlikteki dalgalar için ise tatmin edici sonuçlar elde edilmiştir. Sonuçta elimizdeki modelleriin literatürdeki diğer yaygın modellere rakip olabileceği gösterilmiştir. Çalışmanın geri kalanında üç boyutlu tanklar incelenmiş, bu sefer doğrusal yüzey sınır şartları ele alınmıştır. Dikdörtgen prizma ve silindir şeklindeki tanklar modellenmiştir. Bu çalışmada ek olarak Sanal Kütle (Virtual Mass) modelleri de kullanılmış, ayrıca laboratuvar deneyleri gerçekleitirilmiştir. Elde edilen modeller doğrusal kuramla kıyaslanmıştır ve çok iyi sonuçlar elde edilmiştir. Son olarak ta, gerçek boyutlardaki bir petrol tankının içindeki sıvının gerçek bir deprem altındaki davranışı incelenmiştir. Sonuçta ele alınan iki ve üç boyutlu model deneylerinde RBFCM yönteminin çalkalanma konusunun modellenmesinde etkili bir yöntem olduğu gözlemlenmiştir. Yöntem yeni olmasına rağmen ağsız oluşu ve yüksek boyutlardaki problemler için kolayca uygulanabilir olması, üstün özelliklerinden bir kaçıdır.

TABLE OF CONTENTS

LIST OF FIGURES

LIST OF TABLES

LIST OF SYMBOLS

A_i	Tributary area under a surface node in Virtual Mass formulation
α	Scaling Parameter
a_c	Excitation amplitude
B	Boundary operator
b	Displacement amplitude
β	Polynomial coefficient vector
c	Shape parameter
d	Dimension
η	Free-surface elevation with respect to the mean surface level
E	Elasticity modulus
f	Basis function
f_g, f_e	Grid point and element forces
F	System Matrix
φ	Displacement Potential Function
Φ	Velocity Potential function
ϕ	Disturbance potential function
Φ_0	Potential function defining the motion of the tank
g	Gravitational Acceleeration
J	Bessel Function
k_n	Standing wave
K	Stiffness matrix
l	Tank length
$\mathcal{L}$	Governing differential operator
M_{gg}	Virtual mass matrix
n	The wave number
n	Unit normal vector

$O'X'Z'$	Coordinate system fixed in space
$O\ x\ z$	Coordinate fixed relative to the tank
ω	Frequency
Ω	Domain
$\partial\Omega_W$	Wetted boudnary
$\partial\Omega_F$	Free surface boundary
p	Pressure
Ψ	Mode shape function
ρ	Density
r	Radial Distance
$r_{\min}$	Minimum internodal distance in the domain
$\boldsymbol{q}$	Velocity of a fluid particle
t	Time
$\overline{u}$	Fluid displacement at the boundary
$\boldsymbol{V}$	Tank Velocity
V_x, V_z	Horizontal and vertical velocity components
W_i, W_p	Impulsive and total weight
ζ	Coordinate of the free surface with respect to the global frame

LIST OF ACRONYMS/ABBREVIATIONS

2D	Two Dimensional
3D	Three Dimensional
ADVDYN	NASTRAN Advanced Dynamics Manual
BC	Boundary Condition
BDF	Nastran Bulk Data File
BEM	Boundary Element Method
BVP	Boundary Value Problem
CFL	Courant–Friedrichs–Lewy Condition
DFSBC	Dynamic Free-Surface Boundary Condition
FDM	Finite Difference Method
FEA	Finite Element Analysis
FFT	Fast Fourier Transform
FEM	Finite Element Method
FPS	Frames Per Second
FVM	Finite Volume Method
GE	Governing Equation
GUI	Graphical User Interface
IC	Initial Condition
IVP	Initial Value Problem
MLPG	Meshless Local Petrov–Galerkin
MSTM	Multi-Scaling Trefftz Method
MQ	Multiquadrics
PDE	Partial Differential Equation
PFT	Potential Flow Theory
PS	Phantom Surface
RANS	Reynolds Averaged Navier-Stokes
RBF	Radial Basis Function
RBFCM	Radial Basis Function Collocation Method

RHS	Right Hand Side
QRG	Nastran Quick Reference Guide
TMS	Time Marching Scheme
TPS	Thin Plate Spline
VMASS	Virtual Mass
VOF	Volume of Fluid
ZFS	Zero Free Surface

1. INTRODUCTION

Sloshing phenomena, simply stated, refers to the movement of some liquid inside a container. Any disturbance of the partially filled container causes sloshing. And depending on the type of disturbance and the shape of the container, the free surface of the liquid undergoes different types of motion.

Sloshing can be extensively observed in the routines of everyday life. When carrying a cup of coffee for example, the frequency and amplitude of the motion of the container is intuitively and carefully adjusted to avoid sloshing.

Examples in the industry are also numerous. In ships or submarines, the forces required to balance the vessel are adjusted by using ballast tanks. Arbitrary ship motions may cause the water in these tanks to slosh. This is also true for fuel tanks of ground, sea or space vehicles. In Civil Engineering applications, movements of the containers are often caused by seismic activity. Oil storage tanks for example experience sloshing effect upon earthquake induced vibrations.

Predicting the free surface motions of enclosed liquids is a problem of practical importance. When the amplitudes of the external excitations are large, or the excitation frequencies are close to the natural resonance frequencies of the fluid, large dynamic pressures can occur. In ships, sloshing may cause large rolling moments that can cause capsizing. In the aerospace industry, sloshing of the propellant liquid may cause the rocket to lose trajectory (Abramson, 1966).

Sloshing effect has also been utilized in some engineering applications. An example for this is the usage of tuned liquid dampers. They are used for mitigating wind and earthquake induced vibrations in tall buildings and other structures like long span bridges and offshore structures (Fujii *et al.*, 1990).

In the oil storage tank examples, when present sheet steel prices are considered; it can be calculated that a 1 mm increase in the steel thickness for a tank with 15 m radius will result in an approximately 15000$ increase in the cost of building that tank. The industries that utilize tanks range from petro-chemical to food industry, and size of the tank market suggests that a good know how in sloshing will contribute to the economy.

Our time witnessed many poor design examples in the field of storage tanks. In the 1999 İzmit earthquake, the sloshing effects on the oil storage tanks in Tüpraş refinery have caused structural failures resulted in terrible losses. Similar events occurred during the Kobe earthquake in 1995 and in Taiwan earthquake in 1999. These tanks were all designed due to the design code, and it is evident that there's a lot room for development in this field.

The studies performed in this thesis propose a new and effective method of solution to the problem of predicting free surface motions of liquids in containers undergoing surge and heave motion. The numerical method is the mesh-free radial basis function collocation method (RBFCM). The method is simple, computationally cost effective, and flexible in the sense that it can easily be adapted to non-uniform tank geometries. RBFCM is proven effective for the solution of partial differential equations (PDE), and this thesis demonstrates its applications to fluid flow problems in two and three dimensions and with high free surface deformations.

The results from the models are benchmarked and compared with results from the literature, with laboratory experiments, and with another numerical method commonly used in industry called the Virtual Mass Method.

In Chapter 2, 3, 4, and 5, the background information on previous studies on sloshing are reviewed; the mathematical formulation is derived for a hypothetical 2D sloshing tank, overview on the numerical method is provided, and the procedure for modeling the tank is explained.

In Chapter 6 and 7, idealized 3D sloshing tanks with cylindrical or rectangular-prismatic shapes are formulated. Numerical formulation using RBFCM and Virtual Mass are explained, and information on the laboratory experiments are provided.

Finally, in Chapter 8, the numerical tests and results are presented. RBFCM models are first benchmarked with analytical, numerical and experimental studies from the literature; then they are compared to the laboratory experiments and to the VMASS models, and in the end a sample tank from the industry is analyzed by applying the notorious 1999 earthquake and estimating the peak surface amplitudes.

A number of numerical ingredients that represent recent improvements in the RBFCM technology are experimented with during the studies; and their effects for solving especially the nonlinear high amplitude sloshing are documented in the appendix section. The studies provide know-how in the field of numerical modeling with high deformable free surface boundaries. They may provide a basis for future modeling studies, and also in other fields like fluid structure interaction coupling methods.

2. LITERATURE REVIEW ON MODELING OF SLOSHING

Sloshing has been a fascinating area of research that has acquired interest of many civil/marine/aerospace engineers, geophysicists, seismologists, and mathematicians over the decades. Attempts to model the problem in a fluid dynamics context can be traced back to the book Hydrodynamics by Sir Horace Lamb (1879). Jeffreys (1923), analyzed free oscillations of water in an idealized elliptical lake. Jacobsen (1951) performed experimental studies on rigid cylindrical tanks subjected to transient motions. In the industry, Abramson (1966) released a monograph for NASA solely on sloshing, and analyzed the effect of sloshing on the aerospace industry design details and concepts.

There are various analytical and numerical efforts to solve sloshing, and numerous different approaches and techniques have been developed. Early attempts were aimed at introducing vast approximations on fluid behavior for basic tank design purposes. Later came studies aiming to solve sloshing for arbitrary container shapes and taking into account the highly nonlinear phenomena experienced during sloshing.

In general, liquid sloshing problems are described using the Navier–Stokes equations, kinematic and dynamic conditions at liquid free surface, and the no-slip condition on the walls. However, due to mathematical and computational complexities, simpler models are utilized more commonly. The analytical solutions to the sloshing problem are limited to the derivations of asymptotic solutions to the initial value problem (IVP) developed from the potential flow equations. Faltinsen (1978) is one of the pioneers, and determined the third order asymptotic solution to nonlinear sloshing in 2D tanks under harmonic lateral excitations. The analytical solution from that study is widely used in numerical model validations. Ockendon and Ockendon (1973) also derived analytical schemes for sloshing under lateral or vertical excitations. Frandsen *et al.* (2003) derived third order analytical solutions for sloshing under combined lateral and vertical excitations. In addition, Faltinsen *et al.*, (2000) derived a multimodal algorithm approach for arbitrary tank motions including roll motions.

As for the numerical studies on sloshing, the common approach is again to use the potential flow theory. The problem is modeled in terms of the velocity potential, which satisfies the Laplace's equation within the liquid domain. On the liquid free surface, the kinematic and dynamic conditions; and on the tank walls, the non-penetration condition must also be satisfied to solve Laplace's equation.

Faltinsen (1978) developed a boundary element method (BEM) model for lateral sloshing on 2D tanks. Nakayama and Washizu (1981) also adopted BEM to model rectangular tanks subjected to lateral or vertical excitations. Nakayama and Washizu (1980) further modeled Laplace's equation using the finite element method (FEM). Wu *et al.* (1998) used FEM to model sloshing in 3D with potential flow equations and nonlinear free surface boundary conditions. Frandsen and Borthwick (2003) developed a sigma-transformed nonlinear finite difference model (FDM) and tested the results for vertical sloshing.

When fully nonlinear free surface boundary conditions are used, sloshing becomes a problem involving a deformable free surface boundary. Problems with deformable boundaries are challenging to solve numerically, especially when the deformations get large. Many models require special techniques to track the boundary locations, and common examples of such techniques are Volume of Fluid Method (Hirt and Nichols, 1981) and the Level Set Methods.

Mathematically, different approaches to solve sloshing include using Euler's equations and equations derived from the Navier-Stokes equations. For example Armenio and La Rocca (1996) analyzed laterally excited sloshing solving Reynolds Averaged Navier-Stokes equations (RANS) and using FDM. Chen and Chiang (1999) used Euler equations and nonlinear kinematic free surface boundary condition using FDM. Chen (2005) solved two-dimensional incompressible Navier-Stokes equations with nonlinear free surface conditions using time dependent FDM. Çelebi and Akyıldız (2002) also used FDM to solve Navier Stokes with the Volume of Fluid (VOF) method and modeled rolling motion.

A popular and recent study is that of Liu and Lin (2008), who developed a 3D numerical wave tank solving the Navier-Stokes equations under six degrees of freedom external excitations, their results were verified by using experimental tanks with wave gauges.

Research on sloshing employing Meshless methods is limited. Pal *et al.* (2010) used the Meshless local Petrov–Galerkin (MLPG) method to solve the Laplace equation with nonlinear free surface boundary conditions. Chen *et al.* (2012) solved Laplace's equation with multi-scaling Trefftz method (MSTM), and Wu *et al.* (2011) used a domain type meshless method that is a derivative of the RBFCM.

3. POTENTIAL FLOW THEORY

3.1. Mathematical Model

This chapter provides an overview on the mathematical model that has been used to formulate the numerical models. Sloshing is a phenomenon that involves strong nonlinearities in its nature. But a good mathematical model must at least encompass estimating the free surface motions of the fluid upon an external excitation, and the hydrodynamic pressure distributions along the walls of the container. The mathematical formulation should also be easily adoptable for a computational model. In this thesis, one of the most common mathematical approaches for sloshing, the Potential Flow Theory (PFT) is used.

The PFT approach simplifies fluid flow problems by reducing the problem solutions to the determination of a single scalar variable Φ. PFT assumes irrotational flow, which is defined by the zero curl of velocity:

$$\nabla \times \boldsymbol{q} = 0 \tag{3.1}$$

where $\boldsymbol{q}$ is the velocity of a fluid particle. For irrotational fluid motion, a velocity potential function Φ exists, whose gradient gives the fluid velocity:

$$\mathbf{q} = \nabla \Phi \tag{3.2}$$

PFT also assumes inviscid and incompressible flow. The internal friction and shear stresses are not taken into account, and for individual fluid particles a state of uniform compression at each point is taken. With these assumptions, the conservation of mass is expressed by the divergence of velocity being equal to zero:

$$\nabla \cdot \boldsymbol{q} = 0 \tag{3.3}$$

When this expression is combined with the velocity potential definitions, the Laplace's equation is obtained:

$$\nabla^2 \Phi = 0, \text{ in } \Omega \tag{3.4}$$

Laplace's equation is a second order linear partial differential equation and it governs the domain of the sloshing problem, which is denoted by Ω in Figure 3.1.

Solution to the Laplace's equation should be found through the usage of proper boundary conditions. The boundaries may be classified as the wetted boundaries $\partial\Omega_W$, and the free surface boundary $\partial\Omega_F$. The wetted boundaries comprise the interface between the fluid and the container, and the free surface boundary comprises the interface between the fluid and air. Each of these has to be treated separately and embedded into the problem.

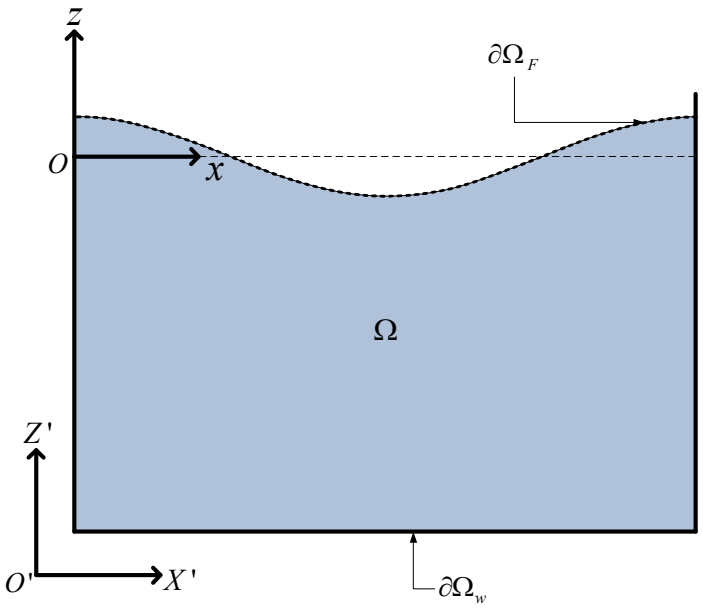

Figure 3.1. The Domain, Boundaries, and the Coordinate Systems for the Sloshing Problem.

One thing to note in Figure 3.1 is that two Cartesian coordinate systems are defined: $O'X'Z'$ fixed in space and Oxz moving with the tank, such that the origin is the left most point of the still water level.

The tank is taken rigid and. The wetted surfaces do not deform during sloshing. Hence, the velocity of the fluid in the liquid-structure interface is taken to be same with that of the tank velocity $\boldsymbol{V}$ for the global coordinate system.

$$\nabla\Phi \cdot \mathbf{n} = \boldsymbol{V} \cdot \mathbf{n} \text{ on } \partial\Omega_I \tag{3.5}$$

where $\mathbf{n}$ is the unit vector normal to the fluid boundary.

Sloshing models for containers that are not fully rigid are also available. One approach is the Virtual Mass Method (VMASS), which is explained in Section 4.3. Virtual Mass formulates a coupled system between the fluid governed by the potential flow theory and the structure, and allows fluid-structure interaction. In this thesis, this method has also been used, to compare the results from the RBFCM models. The numerical tests on the performance of VMASS are provided in Section 8.2.

In PFT, the time dependence of the problem comes through a set of two surface boundary conditions. The first one is the Dynamic Free Surface Boundary Condition (DFSBC) and is derived from the unsteady Bernoulli equation by matching the pressures at the liquid-gas interface:

$$\frac{\partial\Phi}{\partial t} + \frac{1}{2}\nabla\Phi \cdot \nabla\Phi + g\zeta = 0, \text{ on } \partial\Omega_F \tag{3.6}$$

where ζ is the vertical coordinate of the free surface with respect to the global frame $O'X'Z'$.

The second condition is the Kinematic Free Surface Boundary Condition (KFSBC), which is derived from the kinematic condition:

$$\frac{\partial \Phi}{\partial t} = \frac{\mathrm{D}\zeta}{\mathrm{D}t}, \text{ on } \partial\Omega_F \tag{3.7}$$

It is assumed that a particle on the free surface remains on the free surface throughout the motion. The velocity of the particle located on the free surface should be equal to the vertical velocity of the free surface itself:

$$\frac{\partial \zeta}{\partial t} + \frac{\partial \Phi}{\partial X}\frac{\partial \zeta}{\partial X} - \frac{\partial \Phi}{\partial Z} = 0, \text{ on } \partial\Omega_F \tag{3.8}$$

There is no flux of matter of the macroscopic scale and evaporation of the fluid is neglected. The free surface acts like a deformable boundary, on which the free surface boundary conditions KFSBC and DFSBC have to be evaluated. However, the location of the free surface is not a priori information, and in fact the aim of creating the model is to find it. This fact causes a complexity in the time marching algorithms, and its treatment is explained in Section 5.3.

It should be remembered that the external excitations that cause sloshing, changes the location of the container in space. To avoid treatment of complexities arising from boundary conditions on moving walls, a non-inertial reference frame that follows the tank motion is adopted. The coordinate system is shown in Figure 3.1 as Oxz. All variables are measured relative to the moving frame. This procedure can be summarized by first defining the rigid tank velocity with respect to the global frame as:

$$\boldsymbol{V}(t) = V_x \boldsymbol{i} + V_z \boldsymbol{k} \tag{3.9}$$

where V_x and V_z are the horizontal and vertical velocity components. Next, η is defined as the free surface elevation with respect to the reference stationary level. The total

velocity potential function Φ is split into a disturbance potential function ϕ and a potential function defining the motion of the tank Φ_0. The system of equations is transformed to work on moving coordinates. For a sample 2D tank, the IVP can be formulated as:

$$\text{G.E}\begin{cases}\dfrac{\partial^2\phi}{\partial x^2}+\dfrac{\partial^2\phi}{\partial z^2}=\nabla^2\phi=0\end{cases}$$

$$\text{B.C's}\begin{cases}\dfrac{\partial\phi}{\partial x}=V_x,\ \text{on } x=0 \text{ and } x=L\\ \dfrac{\partial\phi}{\partial z}=V_z,\ \text{on } z=-h\\ \dfrac{\partial\eta}{\partial t}=\dfrac{\partial\phi}{\partial z}-\dfrac{\partial\phi}{\partial x}\dfrac{\partial\eta}{\partial x},\ \text{on } z=\eta\\ \dfrac{\partial\phi}{\partial t}=-\dfrac{1}{2}\left[\left(\dfrac{\partial\phi}{\partial x}\right)^2+\left(\dfrac{\partial\phi}{\partial z}\right)^2\right]-g\eta,\ \text{on } z=\eta\end{cases} \tag{3.10}$$

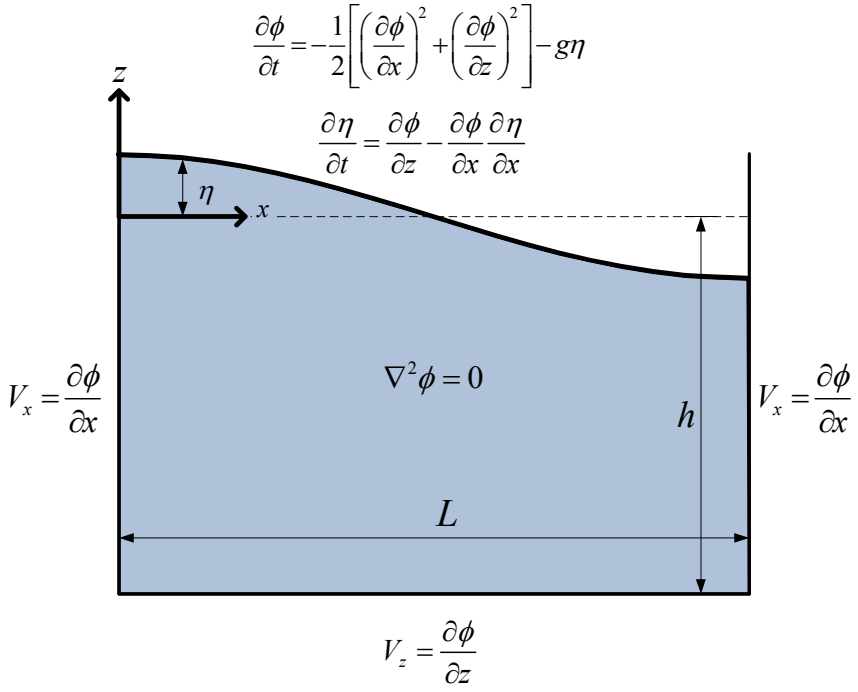

Figure 3.2. The IVP on a 2D sloshing Tank.

For complex geometries and non-harmonic excitations, it is required to numerically model the initial-boundary value problem. However, analytical explicit solutions to the

mathematical model are available for regular and uniform geometries such as rectangular prismatic and cylindrical containers.

3.2. Overview on the Analytical Solutions

Early analytical solutions sought normal modes of oscillation, by using the linearized form of the problem.

The linear small amplitude wave theory formulations are explained in (Stoker, 1957) and (Dean *et al.* 1966) in two stages. First, procedures for linearizing the nonlinear terms of the free surface boundary conditions are developed and second, the procedures for neglecting the free surface deformations are developed. With the small amplitude surface wave assumptions, The DFSBC is modified to:

$$\frac{\partial \phi}{\partial t} = -\frac{1}{2}\left[\cancel{\left(\frac{\partial \phi}{\partial x}\right)^2} + \cancel{\left(\frac{\partial \phi}{\partial z}\right)^2}\right] - g\eta, \text{ on } z = \cancel{\eta} 0 \tag{3.11}$$

and the KFSBC is modified to:

$$\frac{\partial \eta}{\partial t} = \frac{\partial \phi}{\partial z} - \cancel{\frac{\partial \phi}{\partial x}\frac{\partial \eta}{\partial x}}, \text{on } z = \cancel{\eta} 0 \tag{3.12}$$

The BVP that is linearized becomes:

$$\text{G.E}\begin{cases}\dfrac{\partial^2\phi}{\partial x^2}+\dfrac{\partial^2\phi}{\partial z^2}=\nabla^2\phi=0\end{cases}$$

$$\text{B.C's}\begin{cases}\dfrac{\partial\phi}{\partial x}=V_x,\ \text{on } x=0 \text{ and } x=L\\ \dfrac{\partial\phi}{\partial z}=V_z,\ \text{on } z=-h\\ \dfrac{\partial\eta}{\partial t}=\dfrac{\partial\phi}{\partial z},\ \text{on } z=0\\ \dfrac{\partial\phi}{\partial t}=-g\eta,\ \text{on } z=0\end{cases} \tag{3.13}$$

After the linearization, closed form linear analytical solutions to the potential function can be obtained. In the case of seeking normal modes of standing waves, the excitation velocities are set to zero. Solution to the Laplace equation is found by satisfying the surface and wall boundary conditions using the method separation of variables. The time variable expression in velocity potential is taken to be simple harmonic:

$$\phi(x,z,t)=\cos(\omega t)\Psi(x,z) \tag{3.14}$$

where Ψ is the mode shape function, and ω is the mode frequency. When the solution to the Laplace is combined with DFSBC, one will find and expression for the natural frequency:

$$-\omega^2\Psi+g\frac{\partial\Psi}{\partial z}=0 \tag{3.15}$$

The separation of variables solution to the Laplace's equation varies according to the shape of the container and the type of co-ordinate system used. For example for cylindrical containers the solution involves Bessel function and roots of the Bessel function. For cases with variable depth, methods such as the Ritz method are suggested to be used (Ibrahim, 2005). In Section 8.2, the mode shape functions and the mode frequencies are provided and discussed in more detail for cylindrical and rectangular-prismatic containers.

All normal and nonlinear resonance conditions should be avoided in a container design. Therefore, for tank design purposes, determining liquid free surface natural frequencies is important. Determining hydrodynamic loads on the container under forced excitations is also crucial. The hydrodynamic forces are estimated by integrating the pressure distribution over the wetted area. The free surface wave heights come in to play in determining pressure distributions, and they can modify the location of the center of mass.

A linear analytical formulation for forced sloshing is similar to that of analyzing normal modes of oscillation. The boundary value problem is formed by linearizing the boundary conditions. In Ibrahim (2005), the velocity components of $V(t)$ are integrated and combined with Φ_0 to include the excitations only in the KFSBC. In the case of only the lateral excitation, KFSBC becomes:

$$g\eta - \frac{\partial \phi}{\partial t} - x\dot{V}_x = 0 \tag{3.16}$$

where $\dot{V}_x$ is the lateral acceleration. The lateral term x is expressed in Fourier series and the boundary value problem is solved for the velocity potential. The free surface oscillations are found from the velocity potential solution combined with the KFSBC. The dynamic pressure distribution is found from the relation:

$$p = \rho \frac{\partial \phi}{\partial t} \tag{3.17}$$

The weakly nonlinear sloshing problem has also been approached by past researchers, and the studies were based on asymptotic expansion techniques. Hutton (1962) expanded the DFSBC and KFSBC in Taylor series about a stationary surface position. Moiseev (1958) expressed the solution to the potential function in double Fourier series in space and time, and constructed normal mode functions by integral equations in terms of Green's functions. Faltinsen (1978) used Moiseev's theory and obtained steady state solutions of the nonlinear sloshing in a two dimensional rectangular tank. A third order

asymptotic solution was derived for horizontal tank excitations, and this formulation is widely used in numerical model validations. Frandsen (2004) used a similar principle to derive a third order solution for combined lateral and vertical oscillations, and is also a popular benchmark study. Another popular study is from Wu (2007), where the first and the second order potential are derived.

4. NUMERICAL METHODS

Discussion on Potential Flow Theory stated that the analytical solutions to the sloshing problem are limited to simple geometries and excitations. Therefore a numerical scheme has to be employed to analyze non-uniform domains and excitations that may involve nonlinearities. One may choose from a wide list of numerical techniques to attempt solving the problem. The most common methods are the Finite Difference Method (FDM), Finite Element Method (FEM), and Finite Volume Method (FVM); which may be classified as domain discretization techniques. Another popular scheme is the Boundary Element Method (BEM), which provides numerical solutions to boundary integral equations. BEM differs from other methods in the sense that only the boundary has to be discretized. Because it is an integral method, the dimension of the problem is reduced. An overview of a fluid-structure interaction method based on BEM is provided in Section 1.3.

Regardless of the nature of discretization, these methods are derived from assumptions of local interpolation schemes, which require a mesh to support the localized approximations. Hence, meshing has been an integral part of conventional numerical modeling. Often these methods rely on low order approximation schemes like linear and quadratic ones, and catching the high order details and maintaining accuracy relies on the quality and fineness of the utilized mesh.

Mesh generation may only be practical for problems with simple geometries. Especially in high dimensions, constructing the mesh becomes a job that is far from being trivial. The entire computational domain has to be continuously spanned with nodal, area or volume elements, which in methods like FDM have to lie on structured grid points. Meanwhile, interconnectivity information between individual elements has to be tracked. And as the number of dimensions for the problem increase, the interpolation schemes which rely on a “series analysis” approach become more and more complicated. Meshing is an extremely time consuming and expensive task and constitutes most of the modeling effort. For problems with moving discontinuities in particular such as crack propagation

problems, repeated remeshing is required which amplifies the computational cost. In general it can be said that meshing is a factor that over-complicates the art of numerical modeling.

Avoiding mesh generation is possible by treating the problem domain in a “particle field” sense and not in the traditional “continuous mesh-based” sense. In mesh-free methods, rules for node placements across the domain are flexible, and neither the domain nor the surface meshes are required for solving initial value problems. Mesh-free methods have been utilized for some time, and a number of methods for modeling partial differential equations have appeared over the years. Examples of such methods are Smoothed Particle Hydrodynamics, Element-Free Galerkin method, Diffuse Element Method and the Radial Basis Function Collocation Method. A comparative analysis of these methods can be found in (Viana *et al.,* 2008) and (Nguyen *et al.,* 2008). RBFCM is the method used in the majority of this thesis.

4.1. Radial Basis Function Collocation Method

Originally developed for scattered data fitting, RBFCM is proven to be an effective means to numerically model Partial Differential Equations. It is a new but very promising method. The domain discretization phase is significantly shortened due to its simplicity and straightforward implementation. For problem cases which involve high dimensions, and complicated geometries, RBFCM drastically reduces the amount of required labor compared to the conventional techniques. It is exponentially convergent. It is flexible and open to innovation, therefore easily adoptable to different types of problems. Engineering problems in areas including fluid dynamics, heat transfer, solid mechanics, electro-magnetics and finance are within the a broad scope of fields RBFCM has been successfully used. Radial Basis Functions are also used in methods involving statistical learning theory, neural networks and data mining. The mathematical reasoning, derivations and applications to different fields can be found in Buhmann (2003), Wendland (2004) and Fasshauer (2007).

Conventional interpolation schemes are evolved to a new level with the approach of expressing the scattered data as a linear combination of some basis functions. In this context, Hardy (1971) demonstrated Multiquadric (MQ) interpolation method by choosing the basis functions dependent on the data locations and the internodal distances. This innovation is considered to have initiated the research which eventually lead to the formulation of the MQ method as a numerical method for the solution of PDEs. In the following sections, this concept will be elucidated. The derivations are given using Einstein's notation, which simplifies summation operations.

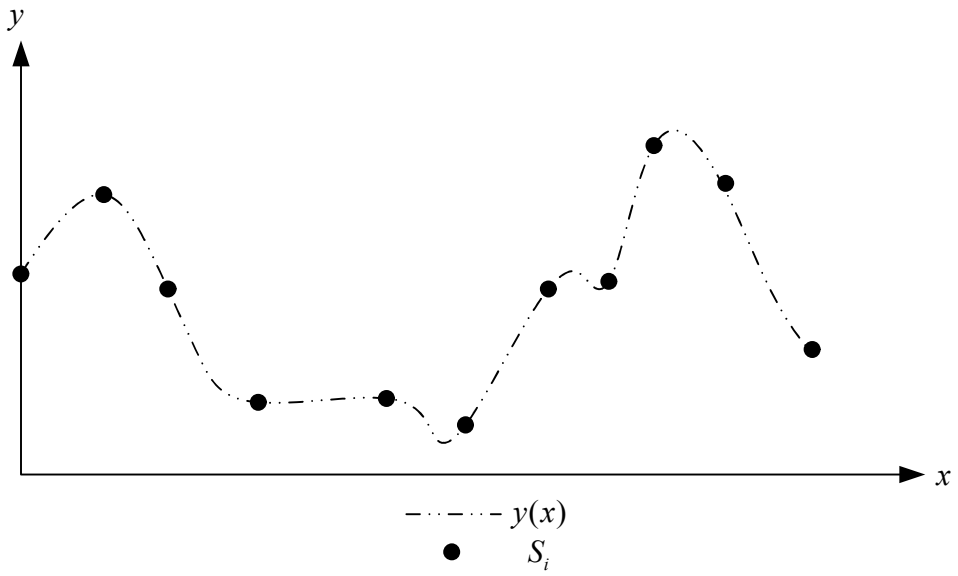

Figure 4.1. Sample function $y(x)$ to be Constructed on 11 Collocation Points S_i.

Figure 4.1. illustrates a simple data interpolation problem. Letting y be the unknown function to be reconstructed; it is first represented as the linear combination of basis functions f:

$$f_i = f(r) \tag{4.1}$$

which is based on information from N many nodes:

$$y(x) = \alpha_i f_i \qquad i = 1,...,N \tag{4.2}$$

Here the basis function f is related to the radial distance between the nodes, hence the name Radial Basis Functions. The radial distance is expressed by:

$$r = \| x - x_j \| \tag{4.3}$$

in which $\| \cdot \|$ denotes the Euclidean norm. In three dimensions, r is simply denoted with the Pythagorean relations:

$$r = \sqrt{(x - x_j)^2 + (y - y_i)^2 + (z - z_j)^2} \tag{4.4}$$

For problems involving dimensions higher than 3, r can also be extended.

To interpolate the value at location x, the linear combination has to be evaluated at that location. The α's, which are the unknown coefficients in the linear combination are evaluated with the interpolation conditions:

$$y(x_i) = s(x_i) \qquad i = 1, ..., N \tag{4.5}$$

where s denotes the known data at the locations x_i. They are represented as the nodes in Figure 4.1. These expressions lead to a system of linear equations of the form:

$$\boldsymbol{f\alpha = s} \tag{4.6}$$

where the entries of the interpolation matrix are given by:

$$f_{ij} = f(\| x_i - x_j \|), \; i, j = 1, ..., N \tag{4.7}$$

$$\alpha = [\alpha_1, ..., \alpha_N]^T \tag{4.8}$$

$$s = [s(x_1), ..., s(x_N)]^T \tag{4.9}$$

And in matrix form:

$$\begin{bmatrix} f(\| x_1 - x_1 \|) & \cdots & f(\| x_1 - x_N \|) \\ \vdots & \cdots & \vdots \\ f(\| x_N - x_1 \|) & \cdots & f(\| x_N - x_N \|) \end{bmatrix} \begin{Bmatrix} \alpha_1 \\ \vdots \\ \alpha_N \end{Bmatrix} = \begin{Bmatrix} s(x_1) \\ \vdots \\ s(x_N) \end{Bmatrix} \tag{4.10}$$

One may then determine the unknown coefficients α from known data, and the system matrix f. Once determined, one may perform interpolation at any location in the domain by using Equation (4.2), and evaluating the Radial Basis Functions at the location to be interpolated.

In the system matrix, each individual element denotes the RBF evaluated with respect to the distance between two nodes; one being the RBF center and the other being the data center. The column indices refer to the data centers and the row indices denote the center for the radial basis functions. RBF Centers and the data centers coincide in the conventional approach. However, one could choose the RBF centers different from the data centers, and the number for the two types of centers need not be equal. Research is still ongoing in this alternative approach and in this thesis, this alternative approach has also been experimented with.

Table 4.1. List of Common Radial Basis Functions.

RBF	$f(r)$	
Multiquadrics (MQ)	$(r^2 + c^2)^{\beta/2}$	$\beta > 0, \beta \in 2N+1$
Inverse Multiquadric	$(r^2 + c^2)^{-\beta/2}$	$\beta > 0, \beta \in 2N+1$
Splines	r^β	$\beta > 0, \beta \in 2N+1$
Thin Plate Splines (TPS)	$r^\beta \ln r$	$\beta > 0, \beta \in 2N$
Gaussian	$\exp(-c^2 r^2)$	

As for the basis function; one may choose from a list of RBFs, including the ones given in Table 4.1. It should be noted that these are globally supported RBF's, and information from all the data centers are taken into account for each RBF center which forms a full system matrix. RBF's with compact support are also available. In Wendland (2005) some compactly supported RFBs, which can be used to form a sparse or nearly sparse system matrices are proposed (Table 4.2).

Table 4.2. Compactly Supported RBF's

Space Dimension	Function	Smoothness
$d=1$	$\phi_{1,0}(r)=(1-r)_+$	C^0
	$\phi_{1,1}(r)=(1-r)^3_+(3r+1)$	C^2
	$\phi_{1,2}(r)=(1-r)^3_+(8r^2+5r+1)$	C^4
	$\phi_{3,0}(r)=(1-r)^2_+$	C^0
$d\le 3$	$\phi_{3,1}(r)=(1-r)^4_+(4r+1)$	C^2
	$\phi_{3,2}(r)=(1-r)^6_+(35r^2+18r+3)$	C^4
	$\phi_{3,3}(r)=(1-r)^8_+(32r^2+25r^2+8r+1)$	C^6

*The subscript (+) denotes that the first term on the right should be taken as zero for $r > R$

Compactly supported functions of minimal degree

To guarantee the positive definiteness of the interpolation matrix for satisfying the nonsingularity of the RBF approximation and to increase accuracy, a finite number of polynomials can be introduced, and the interpolant may be augmented:

$$y(x)=\alpha_i f_i+\beta_j p_j \qquad i=1,...,N,\ j=1,...,M \tag{4.11}$$

where p denotes the added polynomials and βs denote the polynomial coefficients to be determined. Enforcing the interpolation condition from Equation (4.5) leads to a system of N linear equations, and α's and β's produce $N+M$ unknowns. An underdetermined system matrix is formed. The uniqueness of the approximation given in Equation 4.11 is satisfied when the following M additional conditions are imposed to the system:

$$\sum_{k=1}^{N} \alpha_k p_j(x_k) = 0 \quad j = 1,...,M \tag{4.12}$$

For interpolation case, the system of linear equations now takes the form:

$$\begin{bmatrix} f & P \\ P^T & 0 \end{bmatrix} \begin{bmatrix} \alpha \\ \beta \end{bmatrix} = \begin{bmatrix} y \\ 0 \end{bmatrix} \tag{4.13}$$

where

$$\begin{aligned} A_{jk} &= f(\| x_j - x_k \|) \quad j,k = 1,...,N \\ P_{ij} &= p_j(x_i) \quad i = 1,...,N, j = 1,...,M \end{aligned} \tag{4.14}$$

$$\begin{aligned} \alpha &= [\alpha_1,...,\alpha_N]^T \\ \beta &= [\beta_1,...,\beta_M]^T \\ y &= [y_1,...,y_N]^T \end{aligned} \tag{4.15}$$

The contribution of augmentation in the model precision is problem-dependent. Therefore the type and the degree of the polynomial to use for augmentation should be carefully selected. Fang and Horstemeyer, (2007) and Fang *et al.*, (2005) provide comparative analyzes on the performance of augmented RBF's in fluid mechanics problems. In this thesis non-augmented interpolation form is used.

Hardy (1971) successfully used MQ RBF to fit scattered topography data in the demonstrated procedure. Franke (1982) compared various scattered data interpolation methods and concluded Hardy's MQ method was the best among the 30 different algorithms. One is free to choose from the list any RBF depending on the nature of the problem. However, MQ has been the most popular RBF used. Important detail to note is that, some RBFs, including MQ in Table 4.1 depend on the parameter c in addition to the radial distances r. The parameter c is called the shape parameter, and it significantly alters the behavior of the RBF, as shown in Figure 4.2.

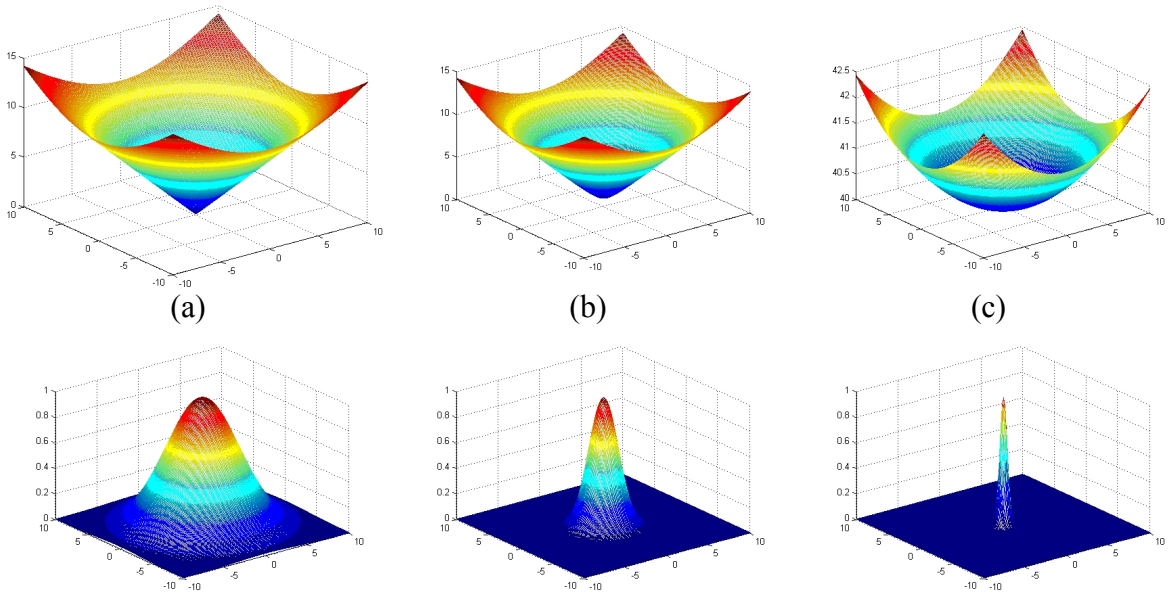

(a) (b) (c)

(d) (e) (f)

Figure 4.2. Effect of Increasing Shape Parameters on the RBFs: (a)c=0.1, (b)c=1, (c)c=40, for MQ RBF and (d) c=0.2, (e) c=0.5, (f) c=2 for Gaussian RBF.

Convergence of a numerical method is often verified by analyzing a sequence of experiments with increasingly large sets of data. For non-stationary approximation, a fixed shape parameter is used for all the experiments, and for stationary approximation, shape parameter is scaled according to a mesh size (Fasshauer, 2007). In densely spaced data, peaked basis functions are preferred and flat basis functions are preferred for coarsely spaced data (Fasshauer, 2007). As for the particular case of MQ RBF, choosing "small" shape parameters produce peaked RBFs and "large" c values form relatively flat RBFs. Having a-priori information about the behavior of the function to be collocated and choosing an RBF with a shape parameter that best fits the solution will eventually reduce the computational cost and result in a closer fit. Choice of the shape parameter is not a trivial task and is a topic still in need for extensive investigation. For MQ RBF, Different approaches for the selection of the shape parameters exist. Hardy (1971) proposed selecting the parameter based on average of smallest internodal distances. Franke and Schaback (1998) proposed a method based on the smallest circle spanning all the data points. Wu and Hon (2003) proposed choosing $4r_{\min}$ where $r_{\min}$ is the minimum internodal distance in the domain. Carlson and Foley (1991) found that the shape parameter is

problem dependent. The optimum shape parameter depends on the behavior of the function to be approximated. Madych (1992) demonstrated that significant improvement can be achieved in the accuracy of the RBF interpolant by increasing the c value. Tarwater (1985) showed that by increasing c, the Root-Mean Square error dropped to a minimum and then sharply increased afterwards. Cheng *et al.* (2003) showed that for very large c values RMS error is of exponential convergence but there's a trade-off between the accuracy gained in interpolation by increasing the c parameter and the stability lost due to the large matrix condition number created.

The shape parameters also need not be constant throughout the formulation of the solution. Since the collocation points may be distributed non-uniformly, the RBFs might be desired to behave different in regions of more densely spaced nodes. This fact adds tremendous amount of freedom in the numerical modeling. However, it will be time consuming to find the optimum selection of the shape parameters. A rule of thumb procedure for shape parameter selection for one particular type of problem will not work for other problems. In this thesis, the optimum shape parameters were sought in multiples of minimum internodal distances. The technique used for the models may be found in the model formation chapters, Chapter 5 and Chapter 6. Also, some shape parameter optimization algorithms were experimented during the studies, which are documented in the appendix section.

4.2. RBFCM For Solving PDE's

Kansa (1986) was the first attempt to solve PDE's based on Hardy's MQ interpolation method. It was shown in (Kansa 1990a, b) the MQ can be used to solve elliptic, parabolic and hyperbolic type PDE's. In the following studies the effectiveness of the technique was demonstrated by Goldberg and Chen (1997) and investigations on applications to IVP's have been carried out by Hon *et al.* (1997). Furthermore, applications were carried out on solving various equations including nonlinear Burger's equation, (Hon, 1997; Hon and Mao, 1998), heat transfer equation (Zerroukat *et al.*, 1998), shallow water equations (Hon *et al.*, 1999; Wong *et al.,* 2002).

In the RBFCM procedure for solving PDE's, the solution is constructed from GEs, BCs and/or the ICs. The data centers are placed inside the domain and on the boundaries. The locations for the RBF centers are more flexible and it is also possible to place them outside the domain.

Starting with the assumption that the solution of the unknown function $u(x,y,z,t)$ is in the form:

$$u_i = f_{ij}(r)\alpha_j(t) \tag{4.16}$$

as in the data fitting technique, the spatial derivatives of u at an individual node i can be derived with:

$$\frac{\partial^n u_i}{\partial \zeta^n} = \frac{\partial^n f_{ij}}{\partial \zeta^n}\alpha_j \tag{4.17}$$

where ζ is a sample coordinate and the derivative of order n can be evaluated with first finding $\frac{\partial \zeta}{\partial r}$ from the Pythagorean relations and using chain rule on the RBF. A list of the first two derivatives for common RBFs can be found in Table 4.3. MQ is continuously differentiable, which is an attractive property for estimating high-order derivatives. Recalling that f depends only on spatial coordinates, the time dependence is left for α 's.

Table 4.3. Derivatives of some widely used RBF's.

RBF	$\frac{\partial f}{\partial x}$	$\frac{\partial^2 f}{\partial x^2}$
TPS	$(x-x_j)r^{\beta-2}(\beta \ln r + 1)$	$r^{\beta-2}(\beta \ln r + 1) + (x-x_j)^2 r^{\beta-4}\left[2(\beta-1) + \beta(\beta-2)\ln r\right]$
r^3	$3(x-x_j)r$	$\frac{3(x-x_j)^2}{r} + 3r$
MQ	$\frac{(x-x_j)}{f}$	$\frac{1}{f} - \frac{(x-x_j)^2}{f^3}$

The complexity associated with the increased dimensions also enters the model formation at this stage with the differentiation of the RBFs. But it is a pretty straightforward and simple task and RBFCM may be considered dimension independent. Only the derivatives of the RBF have to be modified, when the model is to be converted for higher dimensions. That is because the only geometric properties used in the models are the internodal distances between the nodes. In this thesis, 2D and 3D sloshing tanks are modeled and the simple procedure of adapting to 3D from a working 2D model is explained in Chapter 8.

Wu (1992) states that as the spatial dimension of the problem increases, convergence order of RBFCM also increases. This allows the number of collocation points to be reduced for the same degree of accuracy. Madych and Nelson (1990) also states that the method is exponentially convergent and the increased dimension also increases the rate of convergence. In this thesis or in many engineering applications, the problem dimensions are limited to three. But in other fields like computational finance, problems in high dimensions may be of practical importance, and this property of RBFCM makes it a powerful alternative to conventional methods which require special treatments like employing the sparse grid technique. (Larsson, 2008)

For an IVP associated with the unknown function u ,

$$\mathcal{L}u = \varphi, \text{ on } \Omega \tag{4.18}$$

$$\mathcal{B}u = \xi, \text{ on } \partial\Omega \tag{4.19}$$

where L and B are differential operators, and Ω and $\partial\Omega$ are the problem domain and the boundary; a solution to the IVP may be formed with the use of Equation (4.16) in the form

$$u_i = f_{ij}\alpha_j \tag{4.20}$$

which transforms to

$$\begin{aligned} \mathcal{L}u &= (\mathcal{L}f_{ij})\alpha_j = \varphi_i \\ \mathcal{B}u &= (\mathcal{B}f_{ij})\alpha_j = \xi_i \end{aligned} \tag{4.21}$$

A system can be formed in the form

$$\begin{bmatrix} \mathcal{L}f \\ \mathcal{B}f \end{bmatrix} \{\alpha\} = \begin{Bmatrix} \varphi \\ \zeta \end{Bmatrix} \tag{4.22}$$

This form is called Kansa's non-symmetric collocation method, and can be shown in matrix notation as:

$$[F]\{\alpha\} = \{S^*\} \tag{4.23}$$

The F matrix will be formed from the BVP formulation, placement of the nodes, and selection of the RBF and the shape parameter. $\{S^*\}$ will be formed from the initial conditions, boundary conditions and the governing equations. Estimation of the unknown values for the problem becomes as simple as determining the unknown $\{\alpha\}$ and applying the collocation method using Equation (4.16).

As stated previously, the time dependency of the model enters through the α coefficients, and may be treated with conventional time integration schemes. Nonlinear terms may be handled easily by performing multilevel Newton iterations and solving the linearized system at each level.

It should be noted that in Kansa's Method is that the system matrix is non-symmetric and invertibility is not guaranteed. It is also possible to form a system matrix that is symmetric for maintaining nonsingularity. The idea behind the symmetric collocation technique is that the field operator is used at the centers corresponding to the

interior points and the boundary operator at the boundary centers in the definition of the interpolant and the system is set up using this modified interpolant as:

$$u = \sum_{j=1}^{N} (\mathcal{L} f_{ij}) \alpha_j + \sum_{j=N+1}^{N+M} (\mathcal{B} f_{ij}) \alpha_j, \; i = 1, ..., N \tag{4.24}$$

which when used in the IVP gives:

$$\begin{aligned} \mathcal{L}u &= \sum_{j=1}^{N} (\mathcal{L}^2 f_{ij}) \alpha_j + \sum_{j=N+1}^{N+M} (\mathcal{L}\mathcal{B} f_{ij}) \alpha_j = \varphi \\ \mathcal{L}u &= \sum_{j=1}^{N} (\mathcal{B}\mathcal{L} f_{ij}) \alpha_j + \sum_{j=N+1}^{N+M} (\mathcal{B}^2 f_{ij}) \alpha_j = \zeta \end{aligned} \tag{4.25}$$

A system is created which can be written in matrix form as:

$$\begin{bmatrix} \mathcal{L}^2 & \mathcal{L}\mathcal{B} \\ \mathcal{B}\mathcal{L} & \mathcal{B}^2 \end{bmatrix} \{\alpha\} = \begin{Bmatrix} \varphi \\ \zeta \end{Bmatrix} \tag{4.26}$$

Equation (4.26) has a symmetrical system matrix. This technique was developed by Fasshauer (1996) based on Hermite interpolation.

More recent studies on improving the condition of the system matrix involve using preconditioning techniques like the Approximate Cardinal Basis Function preconditioning technique (Brown *et al.,* 2005). Also, there's the approach of enriching the RBF interpolant with singularity capturing terms to account for boundary singularities that arise when there is an abrupt change in the boundary conditions, or if there are re-entrant corners. (Bernal and Kindelan, 2009) The usual approach to try to overcome these issues is to use more RBF centers in the vicinity of the singularity. However, these schemes cause a significant increase in computational cost and their efficiency is not always satisfactory. Their method is based in enlarging the functional space spanned by the RBF by including new functions

that capture the discontinuities in boundary conditions, and yields significant improvements in the accuracy of the solution for the problems considered.

It can be seen from the system matrix descriptions that one type of information can be represented at a given location. Also, collocation center may only represent one type of information. This is because the elements in the system matrix are calculated based on the Euclidean internodal distances. If the location of the two RBF centers coincide or are numerically too close to each other, then for a given row, the same values will be computed for two elements. This will result in identical columns in the system matrix, which will cause singularity. The main drawback of this deficiency is that on the boundaries, the governing equation cannot be represented.

Fedoseyev *et al.,* (2002) proposed a procedure called the PDE collocation on the Boundary (PDECB) to overcome this deficiency. It was noted in the collocation method descriptions that the locations of the RBF centers and the data centers need not necessarily be the same. The procedure exploits this feature and enables using more than one type of information at a particular location. By introducing the supplementary information, additional conditions and equations are brought into the model formulation. This produces a system with the number equations more than the number of unknowns. The imbalance is overcome by introducing additional "dummy" nodes to the system. These additional nodes behave as additional RBF centers and may lie in the interior or exterior of the boundary. The additional rows in the system matrix are filled by evaluating RBFs with respect to the newly introduced conditions on the boundary.

With M as the number of nodes inside the boundary, and N as the number of nodes on the boundary; there are $N' = M + N$ nodes in the original problem formation. And supposing N number of extra conditions are introduced to the system by collocating the PDE on the boundary, N number of extra nodes are added outside the domain. Again the solution is sought in the form of Equation (4.16), which forms the system:

$$\begin{aligned} \mathcal{L}u &= (\mathcal{L}f_{ij})\alpha_j = \varphi_i \quad i = 1,...,N' \\ \mathcal{B}u &= (\mathcal{B}f_{ij})\alpha_j = \xi_i \quad i = N+1,...,N+M \end{aligned} \tag{4.27}$$

In this thesis PDECB had been experimented with and used extensively due to the significance of the information at the boundary of the sloshing problem. A great deal of improvement in the results was achieved with usage of this technique.

PDECB procedure is an example application of using data and RBF centers that are not placed in the same location. The locations of the RBF centers and the data centers may be optimized for better accuracy. It can be said that finding the optimum node placement strategies is a field of research with immense potential. An analysis for optimum node locations for the sloshing problem is is provided in the Appendix section of this thesis.

RBFCM emerged in the 90s, at a time when the commercial codes employing conventional methods like FEM and FDM had secured their places in the industry. RBFCM may be considered still under development and is yet to find the popularity it deserves. The method is very promising in the solution of a wide range of problems but it is subject to some limitations.

The limitations include the high computational cost associated with the system matrices that are full and not sparse as in the case of FEM or FDM. The convergence rate criteria are associated with the increased number of data points, but there's the paradox of the system matrix being susceptible to ill conditioning when too much data points are used. Another problem is that determining the shape parameters is problem dependent but generally not in direct correlation to physics of the problem or a parameter that denotes a physical quantity. Research is still ongoing on these issues and this thesis concludes that despite the limitations, the method may be preferable over conventional methods for the sloshing problem.

4.3. Time Marching Scheme

Supposing there is a simple transient problem modeled in the form:

$$\mathcal{L}u = \frac{\partial u}{\partial t} \tag{4.28}$$

where $\mathcal{L}$ is a differential operator and u is to be determined in space and time. One may choose between the different time marching schemes depending on how smooth the results are expected, and what the degree of order in the ODE is.

The numerical methods for IVP's may be classified into two broad categories as single step and multi step methods.

4.3.1. Single Step Methods

Let u_i be the value of u at the present time step and u_{i+1} be the value at next time step. Single step methods permit the calculation of u_{i+1} from the PDE and u_i. They tend to take slope estimation at a given time and extrapolate the variable to the next time step using the old value and the estimated slope. The method for estimating the slope values may vary. Euler's method for example, is the simplest single step method, and only the first derivative is taken at the present time step:

$$u_{i+1} = u_i + \frac{\partial u_i}{\partial t}\Delta t \tag{4.29}$$

In the Heun's method and midpoint techniques, Euler's method is improved by taking additional mid-steps or applying an additional corrector method to the Euler's scheme. In the Runge-Kutta method which is the most popular, better accuracy is achieved with a Taylor series approach and applying increment functions. Some adaptive Runge-

Kutta methods also exist in which the step sizes are modified. All these methods have the ability to self start.

4.3.2. Multi-Step Methods

Multi-step methods are different from the single step methods in the sense that they acknowledge the value of the information from the previous steps, and make use of it. The curvature of the lines connecting the previous points provides information regarding the trajectory of the solution. This is achieved in the non-self-starting Heun method by modifying the Euler's method as predictor and replacing it with taking two times derivative at u_i and adding it to u_{i-1}.

$$u_{i+1} = u_{i-1} + \frac{\partial u_i}{\partial t} 2\Delta t \tag{4.30}$$

There are also more complicated formulas like Newton-Cotes Formulas and Adams formulas. The method used in this thesis was the multi-step time marching scheme with Adams-Bashforth Predictors and Adams-Moulton Correctors.

Both formulas can be derived from the Taylor series expansions, for the predictor, the expansion is performed around t_i and for the corrector at t_{i+1}. Derivations in detail, stability and error analysis on the mentioned methods can be found in Chapra and Canale (1984). The predictor and corrector formulas are given in Table 4.4 and Table 4.5.

Table 4.4. Adams-Bashworth Predictors.

kth order: $y_{n+1} = y_n + \delta t \sum_{j=0}^{k-1} \frac{1}{c_k} \beta_j f_{n-j} + \mathrm{O}(h^{m+1})$

k	c_k	β_0	β_1	β_2	β_3	β_4	β_5	e_t
1	1	1						$\frac{1}{2}(\delta t)^2 f'(\xi)$
2	2	3	-1					$\frac{5}{12}(\delta t)^3 f''(\xi)$
3	12	23	-16	5				$\frac{9}{24}(\delta t)^4 f^{(3)}(\xi)$
4	24	55	-59	37	-9			$\frac{251}{720}(\delta t)^5 f^{(4)}(\xi)$
5	720	1901	-2774	2616	-1274	251		$\frac{475}{1440}(\delta t)^6 f^{(5)}(\xi)$
6	1440	4277	-7923	9982	-7298	2877	-475	$\frac{19078}{60480}(\delta t)^7 f^{(6)}(\xi)$

Table 4.5. Adams-Moulton Correctors.

kth order: $y_{n+1} = y_n + \delta t \sum_{j=0}^{k-1} \frac{1}{c_m} \beta_j f_{n+1-j} + \mathrm{O}(\delta t^{m+1})$

k	c_k	β_0	β_1	β_2	β_3	β_4	β_5	e_t
2	2	1	1					$-\frac{1}{12}(\delta t)^3 f''(\xi)$
3	12	5	8	-1				$-\frac{1}{24}(\delta t)^4 f^{(3)}(\xi)$
4	24	9	19	-5	1			$-\frac{19}{720}(\delta t)^5 f^{(4)}(\xi)$
5	720	251	646	-264	106	-19		$-\frac{27}{1440}(\delta t)^6 f^{(5)}(\xi)$
6	1440	475	1427	-798	482	-173	27	$-\frac{863}{60480}(\delta t)^7 f^{(6)}(\xi)$

Fourth order formulas from Table 4.4. and Table 4.5. were used in the predictor/corrector scheme. An important property the multi-step methods lack is that they are non-self-starting methods, that is using a predictor of order-four requires having the information from the three previous time steps. Therefore, it is required for a self-starting method to initiate and march the simulation until the predictor/corrector schemes can take over.

4.3.3. Time Marching in RBFCM

While RBFCM procedure was being explained in the previous sections, it was stated that for transient PDE's the time dependence would come into the numerical model formation via time dependent α values.

Revisiting Equation (4.16), the solution to the IVP at a particular time step would be in the form:

$$u(x, y, z, t) = f(x, y, z)\alpha(t) \tag{4.31}$$

The unsteady nature of the problem is reflected in the α vector, which has to be evaluated at every time step. When the RHS of Equation (4.31) is substituted to Equation (4.28) and differentiated:

$$\mathcal{L}f\alpha = f\frac{\partial \alpha}{\partial t} \tag{4.32}$$

The time marching technique of preference should be applied to Equation (4.32), to the α coefficient vector for an incremented time step.

In some problems, the internodal distances may be subject to change in time. In these cases, the system matrix f will also be time dependent. The sloshing problem involves a deformable free surface boundary and the internodal distances are modified at

each time step. This fact requires special system matrix updating procedure. In Chapter 5, treatment of the deformable boundary for the sloshing problem is explained in detail.

One important aspect to consider in the time marching scheme is the time step $\triangle t$. In this study, the time steps were calibrated for each model on a trial and error basis. The approach in the process is explained in Chapter 5.

The time marching scheme actually happens to be of vital importance in the development of numerical simulations. It is an important factor in the run times of the models. Also, a poor scheme may cause error accumulations which would be projected to later time steps, and cause instability. So the modeler has to be careful in choosing the optimum time marching scheme.

4.4. Virtual Mass Method

It was decided to enrich the numerical studies by introducing another numerical technique to analyze sloshing. Virtual Mass Method (VMASS) was selected for this purpose. VMASS was developed for means to implement a Fluid Structure Interaction methodology in a structural modeling environment. On 1979, it was included in the FEM solver NASTRAN, which has been used by design engineers in aerospace and automotive industries over the years. The employment VMASS for modeling of tank sloshing is very limited. Especially for the purpose of analyzing the surface waves the documentation in the literature is nearly nonexistent. Therefore this study aims to explore in depth this rather old but underused technique and demonstrate its implementations in the field of tank sloshing.

This section overviews the theoretical reasoning behind the method, and in Section 6.2, the procedures for analyzing 3D tanks are explained.

Nastran has been developed by NASA during the 1960s as a part of the space shuttle research program and released to the public on 1971. The rights to the development of the code have been acquired by several companies over the years. Therefore it has evolved to different versions. MSC Nastran is the version used in this study. Nastran is an implicit

Finite Element Analysis (FEA) software, and it can perform different types of analyses such as linear static, modal, buckling, direct transient response and many more. Each type of analysis is called a solution sequence, and is assigned a referral number. While predominantly utilized in the automotive and aerospace industry, it has also been used in design phases of Civil Engineering applications such as structures found in airports, theme parks, public and commercial buildings, observatories, and parking garages.

Fluid modeling capability of Nastran is achieved by implementing Virtual Mass method, which uses an approach similar to the BEM. In BEM, as the name suggests, only the boundary of the problem has to be discretized instead of the entire domain. The method is formulated from boundary integral equations; therefore the number of dimensions involved in the numerical model is reduced. When this concept is applied to the sloshing problem, only the boundaries of the fluid has to be discretized, which can be denoted by the wetted surface of the tank. Therefore, for a model with fluid-structure coupling, meshing the structure first and then setting the wetted surfaces to be the fluid boundary will be a good starting point.

The structure solver in Nastran uses conventional FEM, and VMASS is used to embed the fluid to the structure. VMASS, under some broad assumptions adds the inertia associated with the fluid into the mass matrix of the wetted elements of the dynamic structural system. This way, the structural system behaves as if fluid is lumped to the wetted elements, and straightforward structural dynamics analyses are performed.

The oscillations of the free surface are obtained using a similar technique. A Phantom Surface of a very small thickness is created that lies wetted on top of the fluid free surface level. The purpose of the phantom surface is to visualize the liquid sloshing behavior. This surface is attached to the fixed nodes on the ground by some elastic springs, and the stiffnesses of the springs are adjusted to simulate the sloshing oscillations. The wetted phantom surface is analyzed with the remaining structural system.

4.4.1. Theoretical Background

Potential flow theory is again the mathematical foundation for the fluid behavior in the Virtual Mass method formation. The fluid is assumed to hold the following fundamental assumptions:

Table 4.6. Fundamental Assumptions in Virtual Mass Method.

Incompressible
Uniform density (i.e., no layers of different fluids)
Irrotational flow
All nonlinear effects neglected
Internal fluids must have a fee surface
No surface waves or other gravitational effects
No steady flow

The incompressible fluid is to construct a mass matrix defined with full coupling with the accelerations and pressures on the flexible structural interfaces. Also, neglecting the surface gravity effects comes with the assumption that important frequency range for the structural modes is well above the gravity sloshing modes. Density within a volume is taken constant and no viscous (rotational flow) or aerodynamic (high velocity) effects are present. A detailed derivation of the Virtual Mass Matrix and its implementations can be found on (McGockel, 1977).

4.4.1.1.Developing Integral Equations. In (McGockel, 1977), the derivations were started by defining a displacement potential function φ as the integral with respect to time of the velocity potential function. It was stated that, this approach would be handier in fluid-structure interaction problems, because the independent variables used in the structure are displacements. Displacements and fluid compressibility are given as:

$$\overline{u} = \nabla \varphi \tag{4.33}$$

$$\nabla \overline{u} = 0 \tag{4.34}$$

When Equation (4.33) and Equation (4.34) are combined, Laplace's equation is obtained for the displacement potential:

$$\nabla^2\varphi = 0 \tag{4.35}$$

which governs the fluid domain. The momentum equation is given by:

$$\rho\ddot{\vec{u}} + \nabla p = 0 \tag{4.36}$$

where ρ is the fluid density. Substituting Equation (4.33) into Equation (4.36) and integrating gives the pressure:

$$p = -\rho\ddot{\varphi} \tag{4.37}$$

The boundary conditions are taken as:

$$\begin{array}{ll} p = 0 & \text{fluid free surface} \\ \left.\begin{array}{l} \overline{n}\cdot\nabla\varphi = \overline{n}\cdot\overline{u}_{structure} \\ f_{structure} = \overline{n}\rho\ddot{\varphi}A \end{array}\right\} & \text{fluid-structure interface} \end{array} \tag{4.38}$$

where $\overline{n}$ is a unit normal vector and A is the area of a particular element.

The method of solution is an approximate integral method which uses the superposition of some fundamental solutions. These fundamental solutions are the surface distributions of point sources. Hence the variables denoted by the strengths of the point sources are the key elements of the method.

The displacement potential, which can show the displacements and the pressures, is written as sums of the strengths of the fundamental solutions. An integral equation can then be solved to give the strengths of the fundamental solutions in terms of the boundary conditions.

The boundary of the whole problem is subdivided into triangular or quadrilateral finite elements in the method of solution. Each area is applied a uniform strength source distribution. The average normal velocity (flow per unit area) and the force (area integral of pressure) are computed for every area due to every source. This way, the integrals are cast in matrix algebra form. Incompressibility also suggests that there are no time lags or gaps between the fluid-structure interface, allowing expression of the result as a Virtual Mass Matrix.

In (McGockel, 1977), the Mass matrix is derived from the integral equations for the point source distributions over the surface in the following procedure:

The displacement potential due to a point source is given by:

$$\varphi(\overline{r}_i) = -\frac{S_j}{|\overline{r}_i - \overline{r}_j|} \tag{4.39}$$

where S_j is the source strength at location r_j and φ is evaluated at r_i. A distributed source with strength per unit area σ produces a potential:

$$\varphi(\overline{r}_i) = \int_{A_j} \frac{\sigma(\overline{r}_j) dA_j}{|\overline{r}_i - \overline{r}_j|} \tag{4.40}$$

And the fluid displacement becomes:

$$\overline{u}(\overline{r}_i) = -\int_{A_j} \frac{\overline{e}_{ij}\sigma(\overline{r}_j) dA_j}{|\overline{r}_i - \overline{r}_j|^2} \tag{4.41}$$

The process may be summarized as using contributions from the area A_j to estimate the value $\overline{u}$ at $\overline{r}_i$ as shown in Figure 4.3.

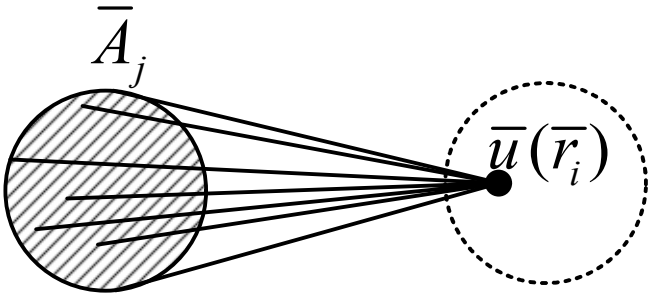

Figure 4.3. Area Contributions.

In Equation (4.41), $\overline{e}_{ij}$ is a unit vector from j to i. The pressure of the fluid is given by

$$p(\overline{r}_i) = -\int_{A_j} \frac{\rho \ddot{\sigma}(\overline{r}_j) dA_j}{|\overline{r}_i - \overline{r}_j|} \tag{4.42}$$

Equation (4.40) and Equation (4.42) relate the displacements and pressures throughout the fluid volume to the surface source distribution. Relating these pressures and displacements of the fluid to those of the structure is achieved by indicating them in matrix form.

4.4.1.2. Developing the Matrix Form. Assuming $\overline{u}(\overline{r}_i)$ for all the interior points are known, the average normal displacement over each element is:

$$u_i = \frac{1}{A_i} \int_{A_j} (\overline{n}_i \cdot \overline{u}(\overline{r}_i)) dA_i \tag{4.43}$$

Each element has a positive normal which must be directed into the fluid. This equation can be written in matrix form as:

$$\{u\} = [\chi]\{\sigma\} \tag{4.44}$$

The explicit form for a term in χ producing a normal velocity in element i due to the source strength of element j is:

$$\chi_{ij} = \frac{1}{A_i} \int_{A_i} \int_{A_j} \frac{\overline{n}_i \cdot \overline{e}_{ij}}{|\overline{r}_i - \overline{r}_j|^2} dA_j dA_i \tag{4.45}$$

The appropriate force quantity to associate with the average normal displacement is the total force on the element in a direction opposite to the direction of the normal. For elements which are wetted on one side, the total force is the integral of the pressure:

$$f_i = \int_{A_i} p(\overline{r}_i) dA_i \tag{4.46}$$

which when expressed in matrix form gives:

$$\{f\} = [\Lambda]\{\ddot{\sigma}\} \tag{4.47}$$

$$\Lambda_{ij} = \rho \int_{A_i} \int_{A_j} \frac{1}{|\overline{r}_i - \overline{r}_j|} dA_j dA_i \tag{4.48}$$

4.4.1.3. Forming the Virtual Mass Matrix. The σ and χ matrices refer to the average displacements and the total normal forces on each element. It is necessary to relate the element displacements and forces to grid point displacements and forces. Letting the vector of grid point displacements in global coordinates be $\{u_g\}$, and the vector of average normal element displacements be $\{u_e\}$; they are related with:

$$\{u_e\} = [G_{eg}]\{u_g\} \tag{4.49}$$

The corresponding relation between grid point forces $\{f_g\}$ and element forces $\{f_e\}$ become:

$$\{f_g\} = -[G_{eg}]^T \{f_e\} \tag{4.50}$$

The negative sign occurs because the positive directions of $\{u_g\}$ and $\{f_e\}$ were chosen to be opposite. The relation between $\{f_g\}$ and $\{u_g\}$ is found to be:

$$\{f_g\} = -[G_{eg}]^T [\Lambda][\chi]^{-1} [G_{eg}] \{\ddot{u}_g\} \tag{4.51}$$

Finally, the Virtual Mass Matrix in global coordinates is obtained as

$$[M_{gg}] = -[G_{eg}]^T [\Lambda][\chi]^{-1} [G_{eg}] \tag{4.52}$$

The Virtual Mass matrix for an incompressible fluid volume is treated in the same way as the mass matrix for Nastran structural element except that it will not be usable in static analysis. Thus, gravity and centrifugal loads will not be computed for fluid masses.

In Chapter 6, the procedures in Nastran for modeling 3D tanks with fluid-structure interaction capability are explained.

Section 6.2 uses the mathematical foundation explained in this section, and gives details about the analysis procedures for the Nastran models created in the studies.

5. 2D SLOSHING MODELS

Mathematicians and engineers have been extensively studying the sloshing problem over the decades. But it is still an extremely hot topic for numerical analysts, due to the challenges involved in modeling the sloshing phenomenon. There are many different sources and types of nonlinear behavior that should individually be investigated. Some of them include high amplitude excitations, run-up along the side walls, viscous sloshing, sloshing in liquids of low – high depths, overturning waves, swirling motion, parametric resonance, or resonance due to the coupling of excitations in multiple directions. In the modeling community, there is simply no consensus on the best modeling practice for handling nonlinear sloshing to its fullest. Also, most commercial computational fluid dynamics software are not benchmarked or verified for the sloshing problems involving large nonlinearities.

The ultimate goal of the studies for this thesis is to demonstrate that RBFCM can be a strong competitor to other methods used to model sloshing. It is aimed to solve the benchmark test cases in an accurate and effective manner. The methodology in the model developments was to first of all create the simplest working model, and then step by step improve the models to solve increasingly complicated test cases.

This chapter explains the path from simple to complex. A fully linear model with no boundary deformations is developed in Section 5.1, and in Section 5.2, certain features of this model are modified to form the fully nonlinear model with deformable free surface boundaries. The 2D test cases documented in Chapter 8 are run using the fully nonlinear model developed in this chapter.

5.1. Linear Model With Stationary Free Surface Boundary

5.1.1. Mathematical Model

In Chapter 3, it was given that the complexity of the sloshing problem came from two sources: nonlinear surface boundary conditions, and the deformable surface boundary. The boundary value problem derived from potential flow theory was simplified under some assumptions to yield a linearized sloshing formulation.

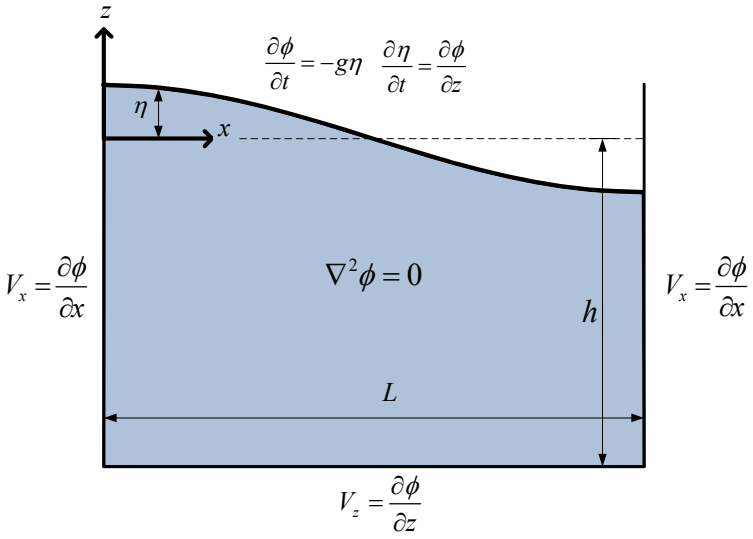

Figure 5.1. Linear Sloshing Problem.

In Figure 5.1, the linearized sloshing problem is shown by revisiting Equation 3.13. The nonlinear terms are dropped, and the free surface boundary conditions are evaluated at the free surface level $z = 0$.

The domain and the boundaries may be denoted as:

$$\begin{aligned} &\Omega : 0 < x < L,\ \eta < z < -h \\ &\partial\Omega_L : \eta < z < -h,\ 0 \le x \le L \\ &\partial\Omega_B : 0 < x < L,\ z = -h \\ &\partial\Omega_S : 0 < x < L,\ z = 0 \end{aligned} \tag{5.1}$$

where Ω is the problem domain, $\partial\Omega_L$ is the lateral boundary, $\partial\Omega_B$ is the bottom boundary, and $\partial\Omega_S$ is the surface boundary.

5.1.2. Numerical Model

5.1.2.1.RBFCM System. In Section 4.1, the procedure for implementing RBFCM for the solution to BVP's was explained. The Equations in Figure 5.1 are transformed to RBFCM notation accordingly in Table 5.1.

Table 5.1. The fully linear sloshing problem formulated in RBFCM.

Analytic Form	RBFCM Form	Location
$\nabla^2\phi = 0$	$\left(f_{ij}^{xx} + f_{ij}^{yy}\right)\alpha_j = 0$	Ω
$\frac{\partial\phi}{\partial x} = V_x$	$\left(f_{ij}^{x}\right)\alpha_j = V_x^{(t)}$	$\partial\Omega_L$
$\frac{\partial\phi}{\partial z} = V_z$	$\left(f_{ij}^{z}\right)\alpha_j = V_z^{(t)}$	$\partial\Omega_B$
$\phi = \phi^{(t)}$	$\left(f_{ij}\right)\alpha_j = \phi^{(t)}$	$\partial\Omega_S$

In Table 5.1, the superscripts denote the partial derivatives, and (t) denotes the current time step. The radial basis function f_{ij} was taken to be the MQ RBF from Table 4.1, with the parameter $\beta = 1$. The shape parameter c was optimized separately for each test case by trying a range of different values. The derivatives of the MQ RBF were taken as in Table 4.3. When the equations are combined in matrix form, the numerical formulation at time t becomes:

$$\begin{bmatrix} f_{11}^{xx}+f_{11}^{zz} & \cdots & \cdots & \cdots & f_{l1}^{xx}+f_{l1}^{zz} \\ \vdots & . & . & . & \vdots \\ \vdots & . & . & . & \vdots \\ f_{1n}^{xx}+f_{1n}^{zz} & \cdots & \cdots & \cdots & f_{ln}^{xx}+f_{ln}^{zz} \\ f_{1(n+1)}^{x} & \cdots & \cdots & \cdots & f_{l(n+1)}^{x} \\ \vdots & . & . & . & \vdots \\ \vdots & . & . & . & \vdots \\ f_{1m}^{x} & \cdots & \cdots & \cdots & f_{lm}^{x} \\ f_{1(m+1)}^{z} & \cdots & \cdots & \cdots & f_{l(m+1)}^{z} \\ \vdots & . & . & . & \vdots \\ \vdots & . & . & . & \vdots \\ f_{1k}^{z} & \cdots & \cdots & \cdots & f_{lk}^{z} \\ f_{1(k+1)} & \cdots & \cdots & \cdots & f_{l(k+1)} \\ \vdots & . & . & . & \vdots \\ \vdots & . & . & . & \vdots \\ f_{1l} & \cdots & \cdots & \cdots & f_{ll} \end{bmatrix} \begin{Bmatrix} \alpha_1^{(t)} \\ \vdots \\ \vdots \\ \alpha_n^{(t)} \\ \alpha_{n+1}^{(t)} \\ \vdots \\ \vdots \\ \alpha_m^{(t)} \\ \alpha_{m+1}^{(t)} \\ \vdots \\ \vdots \\ \alpha_k^{(t)} \\ \alpha_{k+1}^{(t)} \\ \vdots \\ \vdots \\ \alpha_l^{(t)} \end{Bmatrix} = \begin{Bmatrix} 0 \\ \vdots \\ \vdots \\ 0 \\ V_x^{(t)} \\ \vdots \\ \vdots \\ V_x^{(t)} \\ V_z^{(t)} \\ \vdots \\ \vdots \\ V_z^{(t)} \\ \phi^{(t)} \\ \vdots \\ \vdots \\ \phi^{(t)} \end{Bmatrix} \begin{matrix} \text{on } \Omega \\ " \\ " \\ " \\ \text{on } \partial\Omega_L \\ " \\ " \\ " \\ \text{on } \partial\Omega_B \\ " \\ " \\ " \\ \text{on } \partial\Omega_S \\ " \\ " \\ " \end{matrix} \tag{5.2}$$

Recalling from Section 4.1, Equation (5.2) can be written as Equation 4.23:

$$[F]\{\alpha\} = \{S^*\} \tag{5.3}$$

This represents the system at a specified time level t, and a system is to be formed and solved at each time step.

$\{\alpha\}$ vector is the unknown to be determined. In Section 4.2, the time dependence was explained to enter the RBFCM formation via the $\{\alpha\}$ vector, which will be calculated from:

$$\{\alpha\} = [F]^{-1}\{S^*\} \tag{5.4}$$

In Equation (5.4), $\{S^*\}$, $[F]$ and $[F]^{-1}$ should be updated at every time step to find the time dependent $\{\alpha\}$. After this is achieved, any derivative of the ϕ can be estimated with the procedures explained in Section 4.1.

$[F]$ is constructed from the mathematical formulation, numerical formulation and from the layout of the nodes in the problem geometry. In the fully linear formulation, boundary deformations are neglected, geometry is constant throughout the time, and the nodal layout does not change. Therefore, $[F]$can be taken as a constant matrix. It is enough to construct $[F]$ and to compute $[F]^{-1}$ once in the beginning, and use the same matrices in the next time steps.

$\{S^*\}$ is where the RHS of the GE and the BC's are specified. As seen on Table 5.1, for the GE, the RHS is always zero. For the lateral and bottom BC'S, the RHS specify the instantaneous lateral and vertical velocity of the rigid container. They have to be updated at each time increment, and they are found from the external excitations. For the surface boundary, RHS specifies the instantaneous ϕ values, which are determined from the KFSBC and DFSBC and by employing a time marching scheme. The procedure for updating ϕ is explained in the coming paragraphs.

5.1.2.2.Time Marching Scheme. The time dependence of the mathematical model is specified in the surface boundary conditions. However, in the Equation (5.2), the free surface is treated as a Dirichlet BC. So after the system has been solved for a particular time t, the KFSBC and the DFSBC have to be taken into account to determine ϕ values on the free surface at time $t+\triangle t$.

The time marching scheme used in the model was the 4th order Adams-Bashforth predictor and Adams-Moulton corrector, as discussed in Section 4.2. The predictor-corrector method works in two steps. First, data from the past 4 steps is used to predict the value at the next time step. And then, the predicted solution and the data from the past 3

steps are used to correct the predicted solution. This is a non-self-starting method, therefore the model is initiated with a different mechanism. At the first time step, the Euler Scheme was used. 2nd and 3rd order Adams-Bashforth were used in the second and third time steps, and afterwards the 4th order scheme took over. Recalling the linearized DFSBC and KFSBC:

$$\begin{aligned} \frac{\partial \phi}{\partial t} &= -g\eta \\ \frac{\partial \eta}{\partial t} &= \frac{\partial \phi}{\partial z} \end{aligned} \tag{5.5}$$

it can be seen that ϕ and η are dependent on each other, and they have to be simultaneously marched in time. The algorithm developed and used for this purpose is given in Table 5.2:

Table 5.2. Time Marching Algorithm for Linear Sloshing Models.

Action		Updated Variable	Used Variables
#	Description		
1	Predict $\phi^{(t^*)}$	$\phi^{(t^*)}$	$\eta^{(t-4)}, \eta^{(t-3)}, \eta^{(t-2)}, \eta^{(t-1)}, \phi^{(t-1)}$
2	Predict $\eta^{(t^*)}$	$\eta^{(t^*)}$	$\phi^{z^{(t-4)}}, \phi^{z^{(t-3)}}, \phi^{z^{(t-2)}}, \phi^{z^{(t-1)}}, \eta^{(t-1)}$
3	Correct $\phi^{(t)}$	$\phi^{(t)}$	$\eta^{(t-3)}, \eta^{(t-2)}, \eta^{(t-1)}, \eta^{(t^*)}, \phi^{(t^*)}$
4	Determine	$\phi^{z^{(t)}}$	$\phi^{(t)}$
5	Correct $\eta^{(t)}$	$\eta^{(t)}$	$\phi^{z^{(t-3)}}, \phi^{z^{(t-2)}}, \phi^{z^{(t-1)}}, \phi^{z^{(t)}}, \eta^{(t^*)}$
6	Increment time	t	
7	Go to 1		

In the algorithm, ϕ is corrected from predicted ϕ and predicted η; and η is corrected from predicted η and corrected ϕ.

The model might be thought to be composed of two separate systems: the RBFCM system and the TMS system. The two systems are coupled, and feed each other. RBFCM system feeds the TMS system by estimating the ϕ^z values on the free surface, and the TMS

system uses this and the past data to feed the RBFCM system by estimating ϕ values for the next time step.

5.1.2.3.Nodal Layout. The formulation in Equation (5.2) suggests that there are n number of nodes for collocating the governing equation, $m-n$ number of nodes for lateral boundary conditions, $k-m$ nodes for bottom boundary conditions, and $l-k$ number of nodes for surface boundary conditions. The nodes were decided to be uniformly distributed, maintaining a constant minimum internodal distance. A sample nodal layout is shown in Figure 5.2 with property of the nodes being color coded. In this model the RBF centers and the collocation centers are placed in the same location.

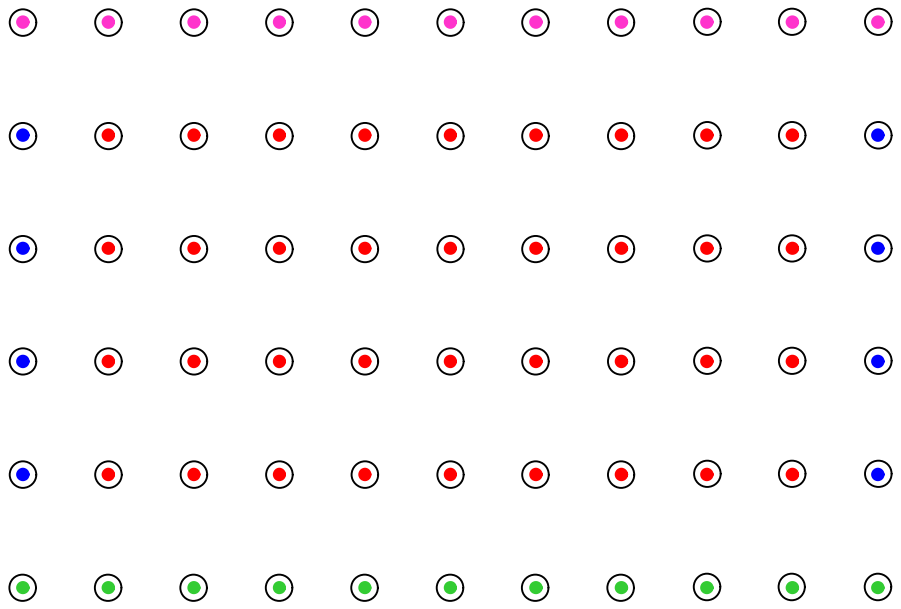

Figure 5.2. Sample Node Placement; ●:GE, ●: Lateral BC, ●: Bottom BC, ●: FSBC, ○:RBF center.

It should be remembered from Section 4.1 that in this formulation a certain data center can only represent one kind of information. It can either be a bottom node, lateral node, a surface node, or a node inside the domain.

PDE collocation on the boundary (PDECB) procedure, which was explained in Section 4.1 is also utilized for the purpose of collocating the Laplace equation on the boundary nodes. For each additional condition on the boundary, an extra RBF center is added outside the domain. The system matrix is formed using the PDECB procedure, and the number of unknowns and the number of equations are equal.

Figure 5.3 shows the additional data centers that are placed outside the domain having a distance of $r_{\min}$ to the corresponding boundary node.

For the corner nodes, it can be seen that two extra RBF centers are placed. This was because other than an extra GE, an extra lateral boundary condition is also applied on the corner ndoes. These additional lateral conditions were added for research purposes and were observed to increase the accuracy in the corners. Therefore they were left in the model formation.

So assuming there are m nodes in the vertical direction and n nodes in the horizontal direction, there would be $m \times n$ nodes inside the domain and on the boundary, $2(m+n)$ nodes placed one unit away from the boundaries to form the PDECB nodes. And 4 corner nodes to collocate additional wall boundary conditions on the corners.

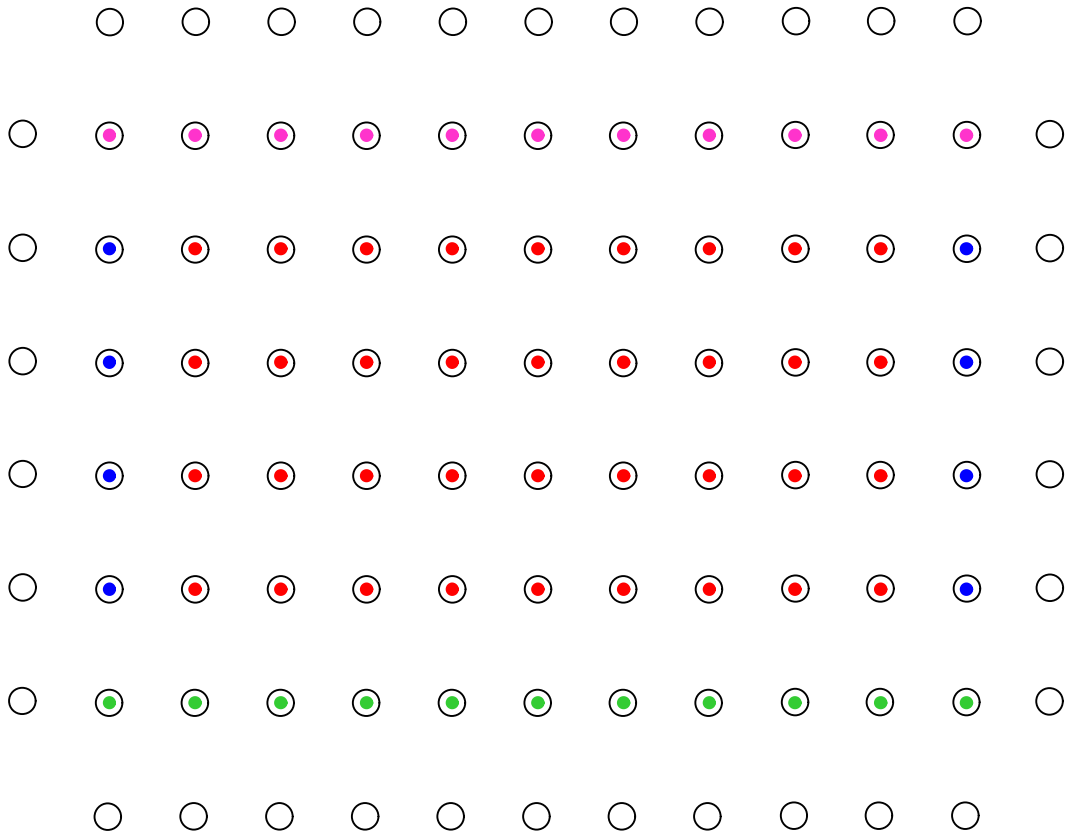

Figure 5.3. Nodal layout showing imposed additional conditions ●:GE, ●: Lateral BC, ●: Bottom BC, ●: FSBC.

5.2. Model with Deformable Free Surface Boundary and Nonlinear Free Surface Boundary Conditions

The models used for the numerical tests were developed by using fully nonlinear boundary conditions, and by updating the free surface boundary at every time step.

The principle difference of the latter model from the linear model is the geometry updating scheme, and theg time integration scheme. Updating the geometry each time step is achieved by locating the surface nodes. Because the problem was formulated in the semi-Lagrangian reference frame, the surface nodes are only allowed to move in the vertical direction. After the surface nodes are placed, then the interior nodes are evenly

distributed between the free surface and the bottom boundary. Alternative procedures were also examined during the studies and are documented in the Appendix section.

The time marching algorithm utilized in this model is shown in Table 5.3. It can be seen that first of all, ϕ and η values are predicted from previous data. Then, ϕ is corrected from the predicted, η and then the geometry is updated. The system for the velocity potential (system 1), and the system for the surface amplitudes (system 2) are solved to estimate the derivatives on the free surface. Finally, predicted ϕ is corrected from all the utilized data.

An important note is that the Laplace equation is not solved again. Because the time step is taken so small that estimating the velocity potential derivatives after step 1 or after step 7 make negligible difference.

When model runs were being performed, experiments on the accuracies associated with using different time steps were analyzed. It was decided to take a rule of thumb type of time step and apply the same approach on all of the models. Three constraints were considered in selecting the time step. The first constraint was about the computation time. In most of the analyses, the model was run for at least 20 periods of harmonic excitation. And because of the number of test cases, it was decided to set the time step so that a period of computation would not exceed 15 minutes of computation time in an Intel Core 2 Duo 2.13 GHz machine. The second constraint was the Courant–Friedrichs–Lewy condition, which states that the computational speed of the wave should not be greater than the physical speed of the wave. Time step for the computational wave should be less than the time for the wave to travel to the next time step. A third constraint was based on the numerical experiments. It was observed that in order to achieve an acceptable accuracy for simple models, marching one sloshing period with 20000 to 25000 time steps was adequate. Therefore the CFL condition was modified to satisfy:

$$\Delta t \frac{\omega_0}{2\pi} \leq 4 \cdot 10^{-4}$$

For all of the models, the time increments were in the order of 10^{-4} seconds.

The nonlinear model developed here is capable of handling low to medium sloshing amplitudes that are $<10\%$ of the mean surface level. For higher amplitude sloshing, different measures were have to be taken. Example of such measures are; separating RBF centers from collocation centers, using different numbers of RBF and collocation centers, mass conservation techniques, and shape parameter optimization. An analysis on the effects of these measures on the high amplitude modeling can be found in the Appendix.

Table 5.3. Time Marching Algorithm for the Nonlinear Sloshing Models.

Action		Updated Variable	Used Variables
#	Description		
1	Predict η^{t*}	η^{t*}	η^{t-1} $\Phi_z^{t-4},\Phi_z^{t-3},\Phi_z^{t-2},\Phi_z^{t-1}$ $\Phi_x^{t-4},\Phi_x^{t-3},\Phi_x^{t-2},\Phi_x^{t-1}$ $\eta_x^{t-4},\eta_x^{t-3},\eta_x^{t-2},\eta_x^{t-1}$
2	Predict Φ^{t*}	Φ^{t*}	Φ^{t-1} $\eta^{t-4},\eta^{t-3},\eta^{t-2},\eta^{t-1}$ $\Phi_x^{t-4},\Phi_x^{t-3},\Phi_x^{t-2},\Phi_x^{t-1}$ $\Phi_z^{t-4},\Phi_z^{t-3},\Phi_z^{t-2},\Phi_z^{t-1}$
3	Correct Φ^t	Φ^t	Φ^{t*} $\eta^{t-3},\eta^{t-2},\eta^{t-1},\eta^{t*}$ $\Phi_x^{t-3},\Phi_x^{t-2},\Phi_x^{t-1},\Phi_x^t$ $\Phi_z^{t-3},\Phi_z^{t-2},\Phi_z^{t-1},\Phi_z^t$
4	Update Geometry	$[F]$	$\eta^{t*}, [F]$
5	Solve System 1	Φ_z^t, Φ_x^t	$\Phi^t, [F]$
6	Solve System 2	η_x^{t*}	η^{t*}
7	Correct η^t	η^t	η^{t*} $\Phi_z^{t-3},\Phi_z^{t-2},\Phi_z^{t-1},\Phi_z^t$ $\Phi_x^{t-3},\Phi_x^{t-2},\Phi_x^{t-1},\Phi_x^t$ $\eta_x^{t-3},\eta_x^{t-2},\eta_x^{t-1},\eta_x^{t*}$
8	Solve System 2	η_x^t	η^t
9	Increment t	t	
10	Goto 1		

6. 3D SLOSHING MODELS

6.1. Models With RBFCM

The aim of the 3D models was to demonstrate the efficiency of the RBFCM in analyzing actual sloshing tank cases. The linear mathematical formulation was used, and rectangular prismatic and cylindrical sloshing tank models were developed in the studies.

3D models were created by modifying the fully linear 2D model. One of the most favorable feature of RBFCM is that implementing the method in higher dimensions is nearly as simple as implementing the method in one dimension. The simplicity of the modeling effort is demonstrated in this section.

6.1.1. 3D Rectangular Prismatic Model

6.1.1.1.Mathematical Model. In the 2D models, the container was free to move in the lateral and vertical directions x and z. For the 3D rectangular prismatic models, the third dimension y, introduced an extra degree of freedom to the system. Movement of the rigid tank was defined by:

$$\vec{V}(t) = V_x\vec{i} + V_y\vec{j} + V_z\vec{k} \tag{6.1}$$

A new lateral BC was added for the third direction and the GE was modified accordingly in the IVP:

$$\text{G.E}\begin{cases}\dfrac{\partial^2\phi}{\partial x^2}+\dfrac{\partial^2\phi}{\partial y^2}+\dfrac{\partial^2\phi}{\partial z^2}=\nabla^2\phi=0\end{cases}$$

$$\text{B.C's}\begin{cases}V_x=-\dfrac{\partial\phi}{\partial x},\text{on } x=0 \text{ and } x=W\\ V_y=-\dfrac{\partial\phi}{\partial y},\text{on } y=0 \text{ and } y=L\\ V_z=-\dfrac{\partial\phi}{\partial z},\text{on } z=-H\\ \dfrac{\partial\eta}{\partial t}=\dfrac{\partial\phi}{\partial z},\text{on } z=0\\ \dfrac{\partial\phi}{\partial t}=-g\eta,\ \text{on } z=0\end{cases} \tag{6.2}$$

The tank geometry and the coordinate system can be seen in Figure 6.1.

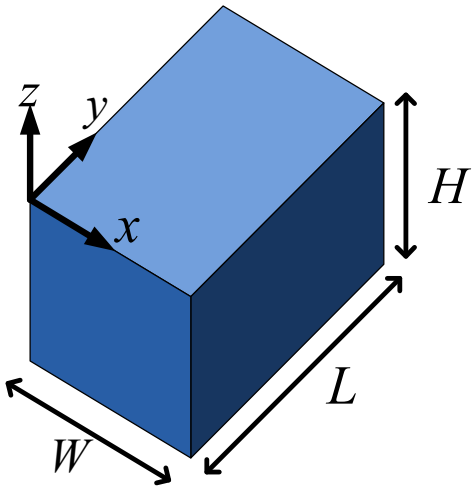

Figure 6.1. Sample 3D Rectangular Prismatic Tank Geometry and Coordinate System.

6.1.1.2.Numerical Model. Similar to the linear 2D numerical model, the RBF for this model was chosen to be MQ RBF. With the increased number of dimensions, the internodal radial distances would be calculated from:

$$r=\sqrt{(x-x_i)^2+(y-y_i)^2+(z-z_i)^2} \tag{6.3}$$

With 3D, the derivative of the RBF with respect to the third dimension should be added to the numerical model formation:

$$\frac{\partial f}{\partial y} = \frac{y - y_i}{f} \tag{6.4}$$

$$\frac{\partial^2 f}{\partial y^2} = \frac{1}{f} - \frac{(y - y_i)^2}{f^3} \tag{6.5}$$

Also, the third dimension has to be considered for calculating the Laplacian:

$$\nabla^2 f = \frac{\partial^2 f}{\partial x^2} + \frac{\partial^2 f}{\partial y^2} + \frac{\partial^2 f}{\partial z^2} = \frac{3}{f} - \frac{r^2}{f^3} \tag{6.6}$$

It can be seen that the amount of work required for increasing the dimensions in the numerical formation is minimal. And the same procedures can be applied to solve problems with even more number of dimensions

6.1.1.3.Nodal Layout. The node placement was set up by thinking of the 3D-Tank as being composed of slices of 2D tanks. The 2D-tank geometries at hand were layered side by side to form the third dimension. Figure 6.2a shows a sample 2D nodal layout similar to that of the linear 2D tank on Chapter 5. Figure 6.2b demonstrates the layer copying phase. As for the lateral boundaries for the third direction, a layer of boundary nodes are placed at both end sides of the point cloud. This is demonstrated in Figure 6.2c with the new lateral boundary nodes shown in black.

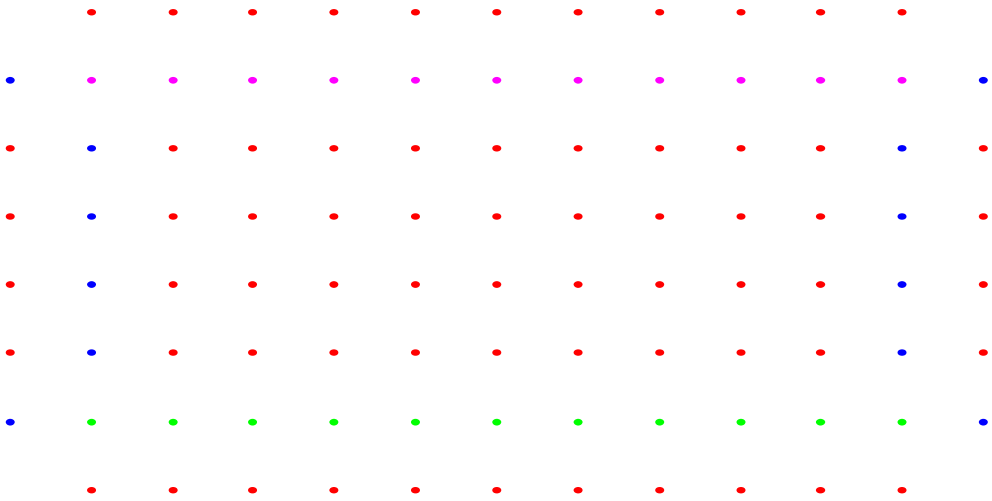

(a)

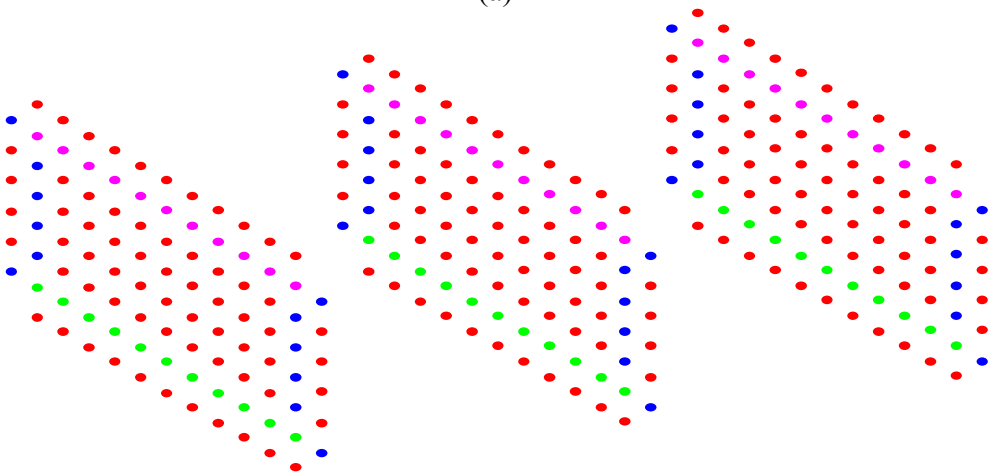

(b)

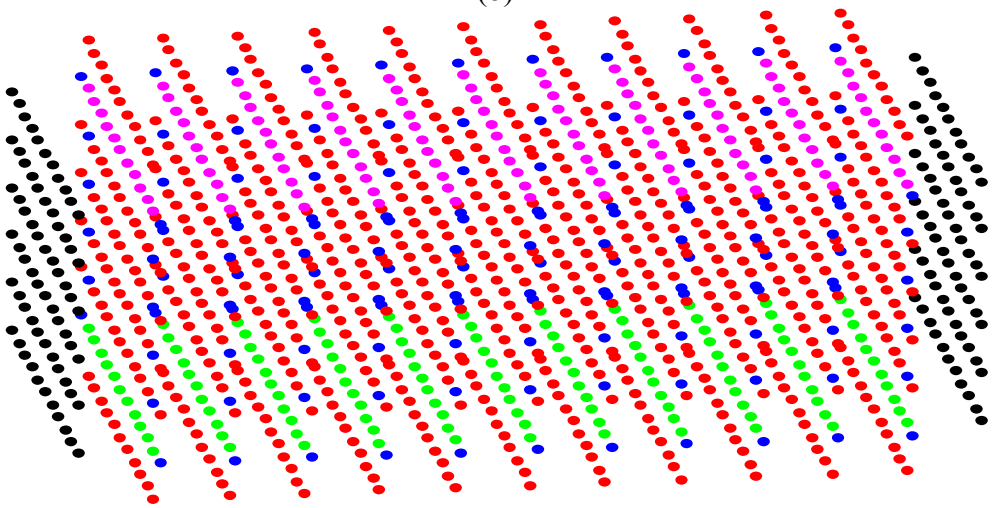

(c)

Figure 6.2. Nodal Layout Formation for a 3D Rectangular Prismatic Tank.

6.1.2. Cylindrical Tank

6.1.2.1.Mathematical Model. Mathematical and numerical formulations for the cylindrical coordinate system were available in the literature. However, it was decided to stick to the rectangular coordinate system to develop the cylindrical model. This way, the code written for the previous tanks were directly used. The movement of the rigid tank was again defined by Equation (6.1).

A cylindrical coordinate system was also defined to easily keep track of the lateral boundary nodes, and to determine the normal direction to the boundary nodes. Figure 6.3 shows the xyz coordinate system and rθz coordinate systems. Correspondence between the two systems can be maintained through:

$$(x,y,z)=(r\cos\theta,r\sin\theta,z) \tag{6.7}$$

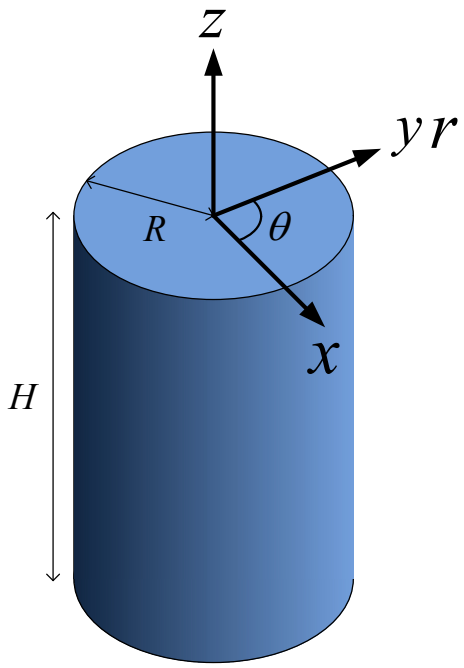

Figure 6.3. Geometry and the Coordinate Systems for the Cylindrical Tank.

In the numerical formulation; the lateral boundary conditions were modified accordingly:

$$\text{G.E}\begin{cases}\dfrac{\partial^2\phi}{\partial x^2}+\dfrac{\partial^2\phi}{\partial y^2}+\dfrac{\partial^2\phi}{\partial z^2}=\nabla^2\phi=0\end{cases}$$

$$\text{B.C's}\begin{cases}V_x\cos\theta+V_y\sin\theta=\dfrac{\partial\phi}{\partial x}\cos\theta+\dfrac{\partial\phi}{\partial y}\sin\theta,\text{on r}=R\\ V_Z=-\dfrac{\partial\phi}{\partial z},\text{on } z=-H\\ \dfrac{\partial\eta}{\partial t}=\dfrac{\partial\phi}{\partial z},\text{on } z=0\\ \dfrac{\partial\phi}{\partial t}=-g\eta,\ \text{on } z=0\end{cases} \tag{6.8}$$

6.1.2.2.Numerical Model. Comparing to the rectangular prismatic model, there are no differences in the calculation phase of the RBFs. For the nodes on the lateral boundaries, the elements in the system matrix were modified to fit Equation (6.8):

$$f_{ij}^{\ x}\cos\theta+f_{ij}^{\ y}\sin\theta \tag{6.9}$$

6.1.2.3.Nodal Layout. To create the nodal layout for the cylindrical tanks, first of all the 2D nodal layout was taken and the coordinate system was fixed at the midpoint of the stationary free surface. Next, the 2D tank was rotated on its z axis, and it was copied to form the principle slices of the cylinder. Figure 6.4a shows the sample 2D nodal layout and Figure 6.4b shows 3 slices of the 2D layout that form the cylinder. The space in between the slices was filled by copying the vertical segments from the 2D layout in between. Figure 6.4c shows the top view of the cylinder after this procedure was performed, and Figure 6.4d shows a sample final nodal layout for a cylinder. The number of rings, slices and vertical nodes were adjusted to maintain a uniform minimum internodal distance throughout the nodal layout.

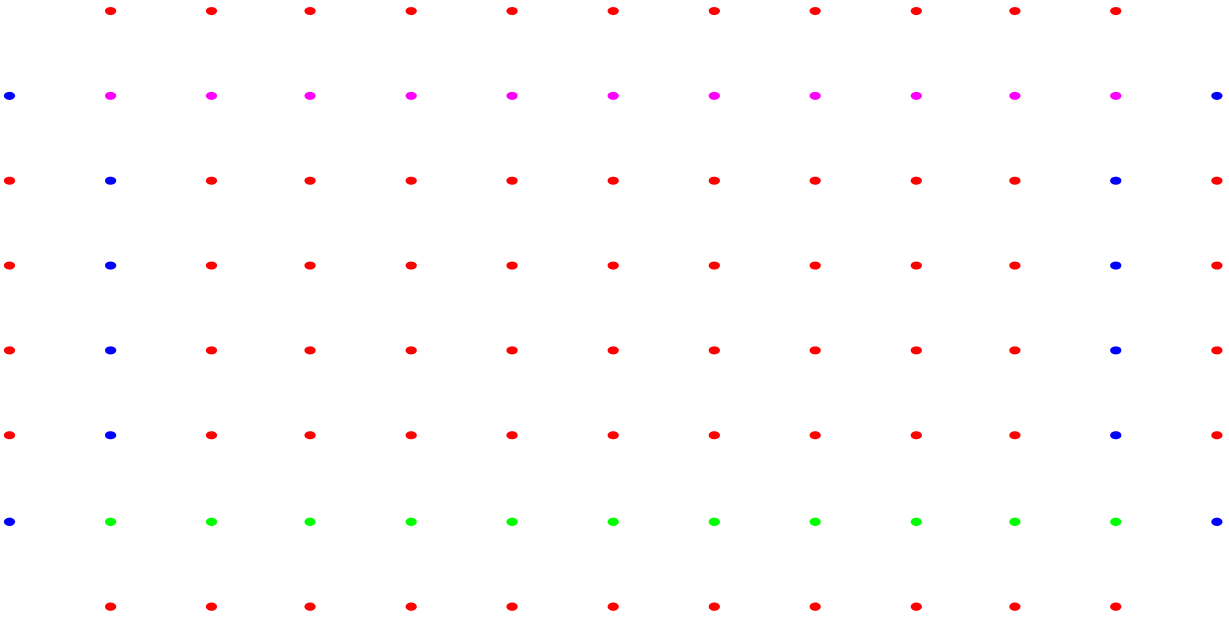

(a)

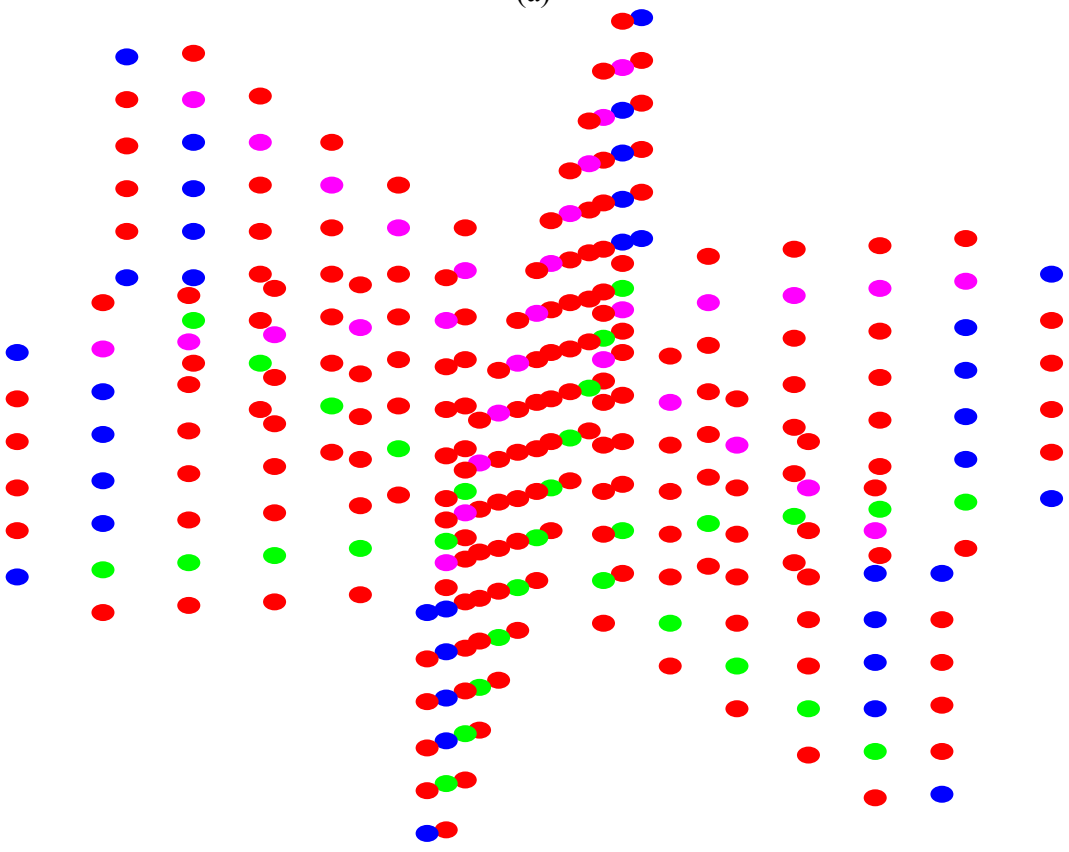

(b)

Figure 6.4. 3D Cylindrical Nodal Layout Formation Example.

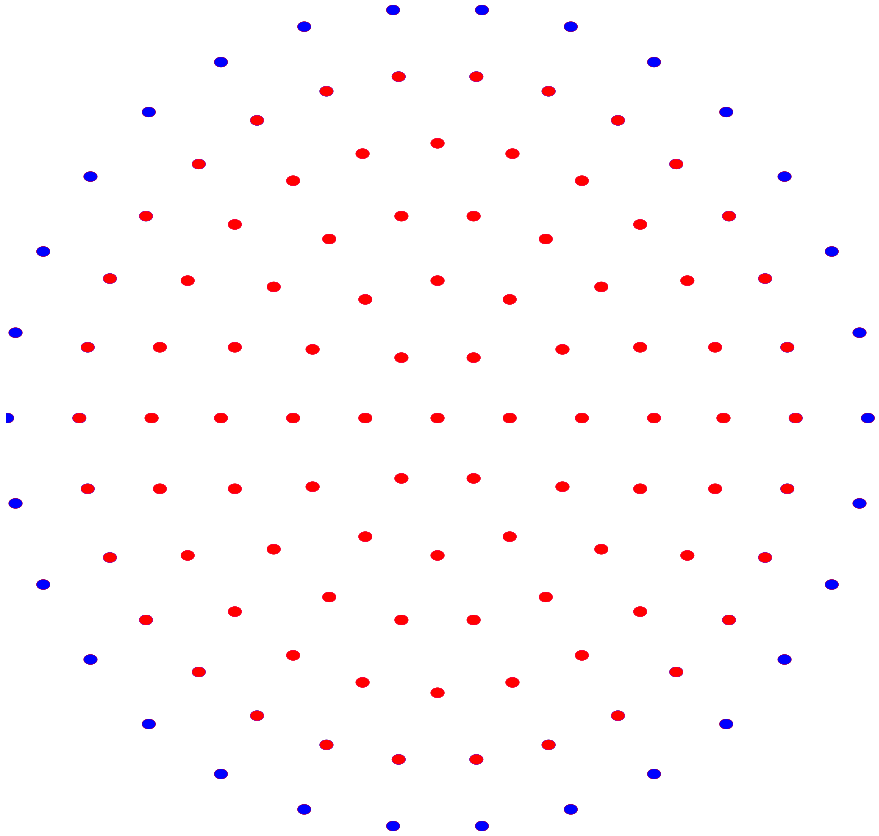

(c)

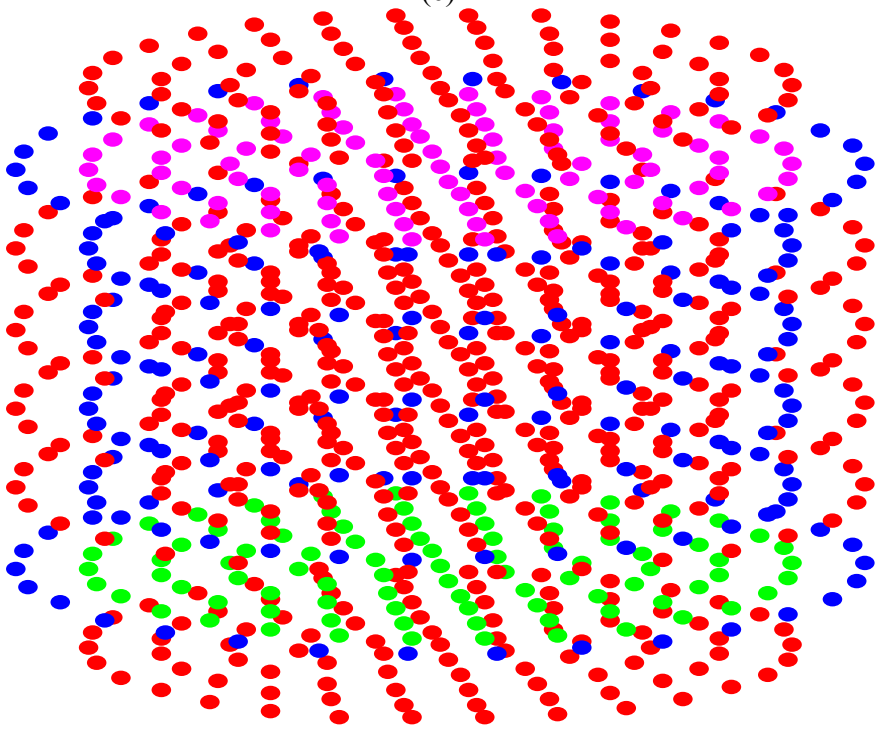

(d)

Figure 6.4. 3D Cylindrical Nodal Layout Formation Example (Cont.).

6.2. 3D Sloshing With Virtual Mass Method

Nastran can perform over 20 different types of analyses. In this thesis, the Virtual Mass models were first analyzed with respect to their performances in finding the natural sloshing frequencies. Modal analysis was performed for this purpose, which has the solution sequence code "SOL 103" in Nastran notation. After benchmarking, lateral earthquake motions were applied to the system. The analysis type for this purpose is Direct Transient Analysis, and the solution sequence code for this analysis is "SOL 109". The benchmarking modal analyzes were compared to the linear analytical solutions, laboratory experiment results, and RBFCM model results. The transient analyzes were only compared with RBFCM results.

The following sections explain the performed procedures for Nastran Virtual Mass modeling of 3D sloshing tanks.

6.2.1. Pre Processing

Nastran is a FEA solver, and it does not have a GUI for model building or meshing. The inputs and outputs are usually in the form of text files. There are also pre and post-processors from third party software companies or MSC Software itself. But no pre processor has the functionality to fully implement Virtual Mass Method, and extensive manual work is required. Therefore, during the studies, a special pre processor was coded for the purpose of performing Virtual Mass analyses on 3D sloshing tanks. As inputs, geometric and material properties of a sloshing tank are given to the pre processor, and Nastran input files are outputted.

The input file format for Nastran usually has the file extension BDF standing for "bulk data file". A BDF file is arranged in five sections as shown in Table 6.1:

Table 6.1. The Organization of a Nastran Input File: Sections are Specified in Bold, and Delimiters are Specified in Italic.

Nastran Statement
File Management Section
Executive Control Section
CEND
Case Control Section
BEGIN BULK
Bulk Data Section
ENDDATA

The first two sections in Table 6.1 are optional and were not modified in this study. Nastran Statement is used to modify system defaults and File Management Section is used to allocate files and to perform database operations. In the Executive Control Section, type of analysis to be performed is specified. CEND delimiter starts the Case Control Section, in which titles and load cases are defined. It requests output and selects bulk data items such as loadings and constraints to be used. And in the Bulk Data Section started by the "BEGIN BULK" delimiter, finite element data, nodes, elements, material and element properties, and boundary conditions are specified. The last line of the BDF file is denoted by the "ENDDATA" delimiter.

The bulk data entry format is simple, but some strict rules have to be followed, which are detailed in the Quick Reference Guide (QRG) of Nastran. For example, character limits per line and per data field, usage of the decimal points, format for continued data entries that do not fit to one line, precision, the default data entries and many more details should be carefully studied from the QRG. The types of entries in the bulk data are denoted as "Cards".

6.2.2. Creating the Surface Mesh

The foremost task performed by the pre processor was to form the surface of the fluid. Tanks with circular or rectangular basins were created during the studies. The shapes of the elements in the meshes were chosen to be quadrilateral. Meshing a rectangular surface from quad elements was straightforward, but for the circular surfaces, this was not an easy task.

In the numerical modeler's point of view, a good mesh should minimize the possibility of ill conditioning in the system matrices and fully and accurately represent the problem domain. Overlapping elements should be avoided. There has to be uniform distribution of the masses. A corner should not be shared by a high number of elements. Elements should be of high quality, being approximately equilateral polygons. And elements should have similar and low aspect ratios.

A random mesh for the circular surface was not thought to be good enough because multiple trials are required to form a "good" mesh. Some different approaches for circular meshes are shown in Figure 6.5. A four-corner approach for a circular mesh will cause singularity due to distorted elements at the edges. And a mesh with its center resembling pizza slices causes singularity on the midpoint due to one corner shared by too many elements and extreme difference in aspect ratio.

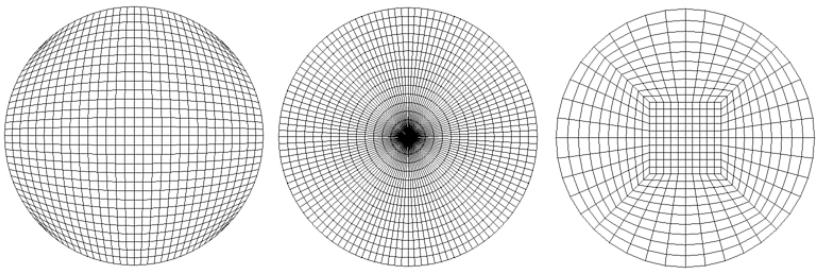

Figure 6.5. Samples for meshing a circle: four corner approach, pizza slice approach, butterfly mesh.

The method utilized in this study was to form a “butterfly mesh”. For this purpose the mesh generation software package “Truegrid” by XYZ Scientific Applications Inc was used. Truegrid worked with a scripting language, and parametric meshes could be maintained easily. The mesh projection method of Truegrid makes creating complicated meshes easy. Mesh transitions can be maintained in a very fast manner.

The procedure for forming the butterfly mesh was initiated by creating all four corner nodes in the center. It was set to have a uniform mesh within the four corner nodes. Next, another group of four corner nodes were duplicated on top and linked to the first four corner nodes. Than a cylinder was formed at the exterior, and the copied nodes were projected to that cylinder. After some calibrations, the butterfly mesh was formed. The size of the kernel, the size of the exterior cylinder and the mesh densities could all be calibrated easily with some commands of the scripting language of Truegrid.

The tank meshes were also created with the Truegrid. In the pre processor, routines were written that would generate Truegrid input files upon inputted geometry and mesh density information. When run, it generated the Truegrid input files, than run Truegrid software to process these input files. The pre processor then analyzed the meshes, and performed the tasks that would turn these meshes to a Virtual Mass model. The next section explains how the surface mesh is treated to form the phantom surface.

6.2.3. Creating the Phantom Surface

In the created BDF for the surface, the locations of the surface nodes are specified in GRID cards, and the meshes are created with quadrilateral elements denoted in QUAD4 cards. These elements are linked to PSHELL and MAT1 cards in the bulk data, which are created to specify very small thickness and stiffness values. It was explained in Chapter 4 that the purpose for the surface mesh was only to visualize sloshing; hence the name “phantom surface” was used. Therefore the surface does not have to attain any considerable physical properties. The motion of the phantom surface is maintained through constraining all in-plane motions and rotations to zero and attaching vertical scalar springs

to the nodes with the CELAS2 card. The stiffness values for the elastic springs are to be calculated from:

$$K_i = A_i \rho g \tag{6.10}$$

where i is the index number, A_i is the tributary area under the individual grid point, ρ is the fluid density and g is the gravitational constant. The calculation of the tributary areas might be trivial for a uniform rectangular mesh. But it was decided to develop a generic algorithm that will work on any given surface mesh created with quadrilateral elements.

In the routine for calculating the spring constants, the BDF file including the surface mesh information is analyzed. Letting N be the number of quad elements and M be the number of surface nodes, the steps of the routine may be shown as:

(i) Store GRID ID numbers of the corners of QUAD4 elements in a $4 \times N$ array "quads".

(ii) Store the coordinates of all GRID elements on the surface in a $2 \times M$ array.

(iii) Create a $4 \times M$ array to store the QUAD4 ID numbers of all adjacent quad elements attached to the surface grid elements.

(iv) Calculate areas of the quad elements.

(v) Calculate centroids of all the quad elements and store in a 2xN array.

(vi) Take the $4 \times N$ "quads" array calculate and store the tributary areas corresponding to each corner.

(vii) For all individual surface nodes, sum the tributary area contributions from the adjacent quad elements and store, and acquire the A_i values in Equation (6.10).

(viii) Calculate the K_i values from Equation (6.10).

The method for calculating the tributary areas in Step 6 is to first identify the mid points of the sides, and then to divide the quad elements to four. So each smaller element

had one common corner as the centroid of the bigger quad. Figure 6.6 shows how an arbitrary quad element may be divided to calculate the tributary areas. And Figure 6.7 summarizes the procedure in Step 7.

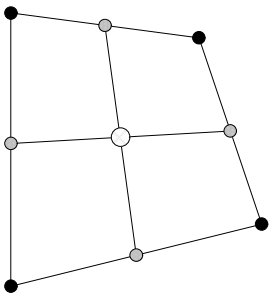

Figure 6.6. Image Showing How a Sample Quad Element Will be Divided, ●: Corners, ○: the Centroid, ○: Mid points of the Sides.

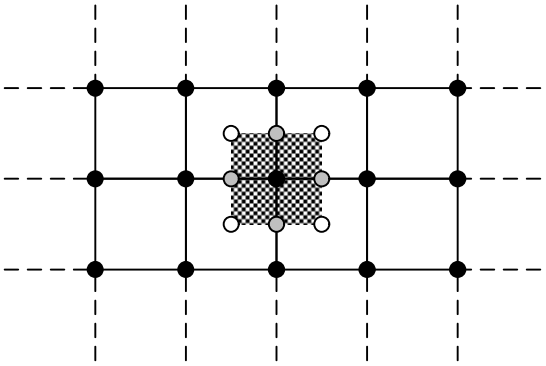

Figure 6.7. Image Showing Tributary Area Contributions to a Surface Node From Adjacent Quad Elements, ●: Corners, ○: the Centroid, ○: the Mid points of the Sides, ▩: Tributary Area Contributions.

As for constraining the in plane motions and rotations of the surface, SPC card was pointed to the single point constraint bulk data SPC1. In the Phantom Surface, all the nodes were constrained in all the directions except for the vertical direction.

6.2.4. Creating the Tank Mesh

The meshing of the tank is performed by first forming the tank bottom. The procedure is the same as for the fluid surface. The walls of the tanks were formed by taking

the exterior outer-most nodes of the bottom mesh and copying and offsetting them in the vertical direction with constant intervals.

To achieve the simulation of a rigid tank, the default material property values were taken to have large thickness and stiffnesses. However, caution is required to avoid singularity in the system matrices upon taking too large or too small material properties. An analysis on the effect of modifying the material properties on the results is provided in Section 8.2. Also for the rigid tank, the bottom node lying on the center was set to be fixed with the SPC1 card. The rest of the tank bottom was linked and grouped to this fixed node by the RBE2 card, which defines rigid body elements. This way, any movement on the reference node would be reflected in all of the tank bottom nodes.

6.2.5. Considerations for Virtual Mass

Two important cards required for the Virtual Mass analysis are the ELIST and the MFLUID cards. Virtual Mass matrix is formed for the elements that are wetted. And for an element to be wetted, it has to attain two conditions. First, it has to be listed in the ELIST card denoting wettable sides of the quad elements; and second, it has to lie beneath the zero free surface level (ZFS). Therefore for the Phantom Surface to work, it is important for the ZFS to be set above the location of the surface mesh. This ZFS information and physical properties of the fluid are specified in the MFLUID card.

Setting up a phantom surface beneath the ZFS and totally enclosing the boundary results in a model such as in Figure 6.8:

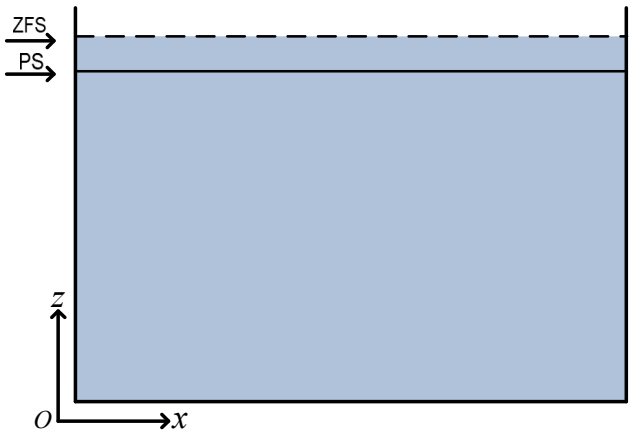

Figure 6.8. Sample 3D tank cross section showing the zero free surface level (ZFS) over the Phantom Surface (PS), which results in a totally enclosed fluid volume.

which results in a totally enclosed fluid volume. Nastran Advanced Dynamics Manual (ADVDYN) states that a totally enclosed fluid volume results in the singularity of the χ matrix in Equation 4.19 due to a set of nonzero sources producing zero velocities on the structural surfaces. This results in occurrences of large pressures due to infinitesimal volume changes on the incompressible fluid. There are some methods to overcome this singularity, like constraining the structure to eliminate any net change to the enclosed volume, or by putting one or more small holes in the boundary. The method used in this study was to set the phantom surface dimensions smaller than the structure surface. This way the fluid would leak to the free surface and the singularity would be avoided. The best method to overcome this issue is not well defined in the literature, and some more research is required.

6.2.6. Comments on the Virtual Mass Model for Sloshing Analysis

It is noteworthy to mention that Nastran is originally a structures solver and the fluid compatibility is derived by modifying the structural solver. Even though the fluid was tried to be isolated in this study by means of strengthening the tank physical properties, it is evident that some amount of fluid – structure interaction is present in the results. A

sensitivity analysis on changing various properties of the tank and their reflections on the results are tabulated in Section 8.2.

The pre processor developed in this study automatically performs all the tasks for analyzing a 3D sloshing tank, like forming the meshes, attaching the CELAS springs, making the tank rigid, and listing the wettable elements. Therefore parametric studies on tanks of variable sizes may easily be carried out.

In this thesis, sizes of the analyzed tanks for the benchmarking studies were taken similar to the tanks used in the laboratory experiments. For the analysis of the earthquake induced free surface motions, a more realistic tank design is taken. The details on that tank may be found at the end of Chapter 8.

7. LABORATORY EXPERIMENTATION

A series of shaking table experiments were conducted by applying sinusoidal excitations to partially-filled containers by Kilic and Erginbas (2009). The raw data from these experiments were analyzed in this thesis and used for additional information to benchmark the numerical models. In this chapter, the procedure of the experiments and the method for analysis of the data is explained.

Cylindrical and rectangular prismatic containers were tested in the experiments, and their dimensions are tabulated in Table 7.1. The containers were manufactured from 3 mm thick Plexiglas material, with an elasticity modulus of $E = 3.1\text{GPa}$. These material properties may practically hold the rigid tank assumption for the tanks of given sizes.

Table 7.1. Dimensions of the Containers.

Code	Basin	Dimensions
C10	Circular	d=10, h=50
C15	Circular	d=15, h=50
C20	Circular	d=20, h=50
R1510	Rectangular	L=15 W=10, h=50
R1515	Square	L=10, W=10, h=50

The contained liquid was water, which may be considered to hold inviscid and incompressible fluid assumptions. The heights of all of the containers were 50cm and were filled to approximately two thirds of their depths.

The oscillations were initiated from a frequency of 2 Hz and with a maximum acceleration of 0.1g. The starting frequency was a limitation from the instrument, but the sizes of the containers were selected such that the lowest mode frequencies for all of the tanks were above 2 Hz. So a decent initiation frequency was maintained. The instrument could change the frequencies with a minimum of 0.01 Hz per increment.

The experiments were started by taking a partially filled container and choosing an axis for excitation. For similar excitation frequencies, different mode shapes could be triggered depending on the excitation axis. For the container with rectangular basin, two experiments were conducted, by taking the axis of excitation parallel to width and parallel to the length of the tank. For the square tank R1010, the axis of excitation was taken first parallel to one side, and then as the diagonal axis. The cylindrical containers are symmetrical in all directions so one shaking experiment was conducted per tank. In Figure 7.1, sketches of the tanks and their axes of excitations can be seen.

After the set up, the experiments were conducted by continuously shaking and filming the response. It was attempted to capture the sloshing modes by scanning the frequency interval between 2 to 6 Hz. The frequency incrementation procedure was performed in an observant basis. The frequencies to focus on were not pre determined. When the observer suspected of witnessing a possible sloshing mode, the attempt was to fine tune the excitation frequency in order to produce the clearest visuals.

The filming equipment has recorded the experiment with 25 frames per second, but film could be analyzed on the computer software with 14 frames per second. The highest excitation frequency in all the cases was about 6 Hz, and 14 FPS was enough to cover the most of the observable mode shapes.

The video was shot with approximately a front – top view. This resulted on a clear visual representation of the mode shapes that were along the axis of excitation. Detecting the mode shapes due to the opposite axis was a challenging task.

The literature was searched to find the analytical mode shape functions, and formulae for the corresponding mode frequencies. They can be found in Chapter 8. To have an understanding of the mode shapes, they were plotted in Matlab. The videos were analyzed frame by frame to identify the mode shapes. Any resemblance of the surface profile was noted by taking series of screenshots to demonstrate one period of the mode shape. The corresponding excitation frequencies were also noted.

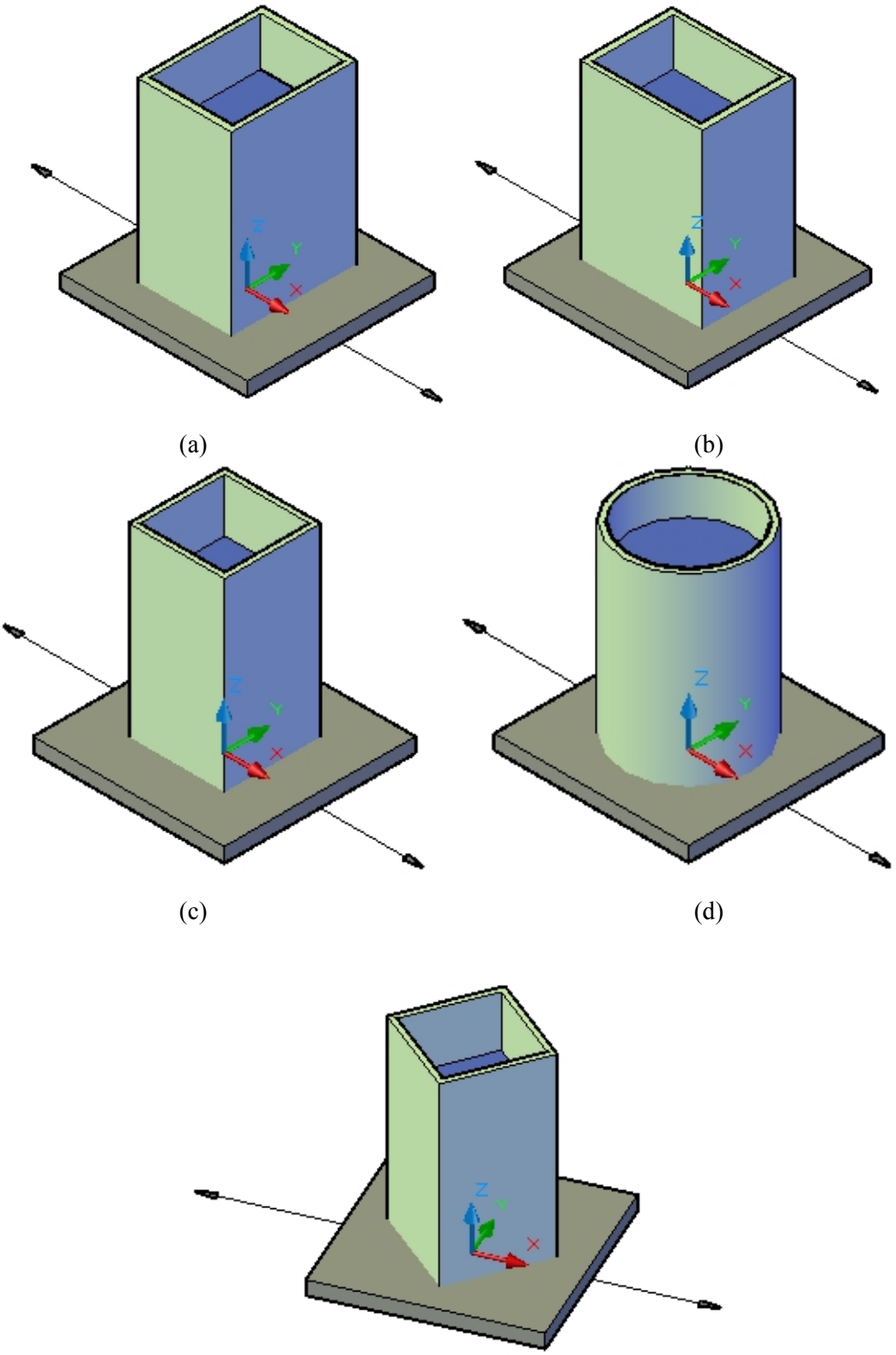

(a) (b)

(c) (d)

(e)

Figure 7.1. Image showing tank axes and the excitation axes in black.

The results were compared to the analytical frequencies from the literature, and the deviations from the linear theory were analyzed. Analytical mode shapes and their frequencies also formed the basis for the validation the 3D RBFCM and VMASS models.

The results, analysis of the data and the criticism on the experimental procedure can be found on Chapter 8.

7.1. Criticism and Suggestions on the Experimental Procedures

Free surfaces were not measured in any way. Wave gauges might have been used, or the containers might have been scaled before filming. This way the surface amplitude versus time graphs or the maximum amplitudes might be compared.

The excitation frequencies were not determined before conducting the experiments. The system might have been allowed to go to rest before trying an excitation frequency. This way, an accurate initial condition would have been supplied to the numerical models.

The contained liquid was not dyed, and the surface was filmed at a fixed angle. The tanks may have been filmed with other angles or with an isometric angle so that surface behavior would more clearly be observed.

8. NUMERICAL TESTS AND RESULTS ON 2D SLOSHING

In this section, the tests performed on the 2D RBFCM models are presented. The test cases are selected from the benchmark problems popularly used for model validations in the literature. Four different types of test cases were analyzed in the studies: lateral excitation cases, vertical excitation cases, combined lateral and vertical excitation cases, and standing wave cases. In the first part of this section, the boundary conditions for each case, and the methodology of analyzing the outputs is discussed. Then, the graphs comparing the present results to the solutions from the literature are presented. The results on high amplitude sloshing may be found in the section of lateral sloshing.

All the models except the high amplitude models were created with the procedures explained in Chapter 5. The nodal layout procedure, boundary deformation procedure, and the time marching scheme were as presented in Chapter 5. For the high amplitude problems, certain modifications to this procedure were applied. The Appendix section of this thesis documents these modifications.

8.1. Methodology For the Analyzes

When the literature on sloshing is analyzed, it can be seen that the common method for outputting the results is to plot the amplitude versus time graphs. A particle on the free surface is kept track of, and the surface amplitude at that location is recorded. The particle is often chosen to be a point very close to the tank wall, or a point in the middle of the surface. In this study, all the cases were analyzed at the point on the surface touching the left wall of the tank. This point will correspond to the coordinate $x = 0$ on the coordinate system moving with the tank as shown in Figure 8.1.

In Frandsen and Borthwick (2003), the parameters in the amplitude vs. time graphs were non-dimensionalized by:

$$t^* = \omega_c t$$
$$\eta^* = \frac{\eta}{a_c} \tag{8.1}$$

where the time histories t and the wave heights η are normalized with the characteristic sloshing frequency ω_c and the characteristic wave amplitude a_c. This simple notion is found very useful for comparing results from different test cases. Therefore, all the plots in this study are non dimensionalized. The results from the test cases are compared to the amplitude vs. time graphs from the analytical, numerical or experimental solutions from the literature.

The published analytical solutions are in the form of asymptotic formulas derived from solving the nonlinear PDE's with standard perturbation theory. A recent study is in Wu (2007), where the first and the second order potential are derived. First and second order resonance is analyzed in this paper for varying excitation frequencies. A very popular second order asymptotic solution for lateral sloshing is also provided in Faltinsen (1978). This solution has been commonly used in model verifications. In Frandsen and Borthwick (2003), a third order asymptotic solution for standing wave and vertical sloshing is derived, and in Frandsen (2004), third order solution for lateral and combined lateral and vertical sloshing can be found.

As for the numerical benchmark studies, popular models are from Liu and Lin (2008), where FDM is used to solve RANS; and Frandsen(2004), where FDM with sigma-transformation is used with potential flow theory.

Analytical and numerical results are often verified with experimental studies. Results are available in studies of Liu and Lin (2008) and Faltinsen *et al.* (2000). In these studies, shaking table experiments were performed to analyze lateral sloshing and wave probes were used to record the free surface elevation with respect to time.

A combination of these published data is used to benchmark the studies in this thesis. The wide range of test cases show that the RBFCM models can be considered a strong competitor to the recent numerical tank designs widely accepted and referenced in the literature.

In the studies, the coding environment was chosen to be Matlab. All the models were coded, run and the results were post processed in the Matlab platform.

8.2. The Boundary Conditions

There are three types of BC's in the model formation: free surface BC, lateral wall BCs and bottom BC. It was stated in the coupled system discussion at Section 4.2 that, time marching scheme (TMS) feeds the RBFCM formulation with the BC for ϕ's on the free surface, and RBFCM formulation feeds the TMS with the derivatives on the free surface. For the lateral and bottom boundaries, the BC's for each time step are supplied from the external excitations.

To initiate the models, the only remaining information to be supplied to the system is the information about the free surface. The IC's and BC's for the test cases are tabulated in Table **8**.**1**.

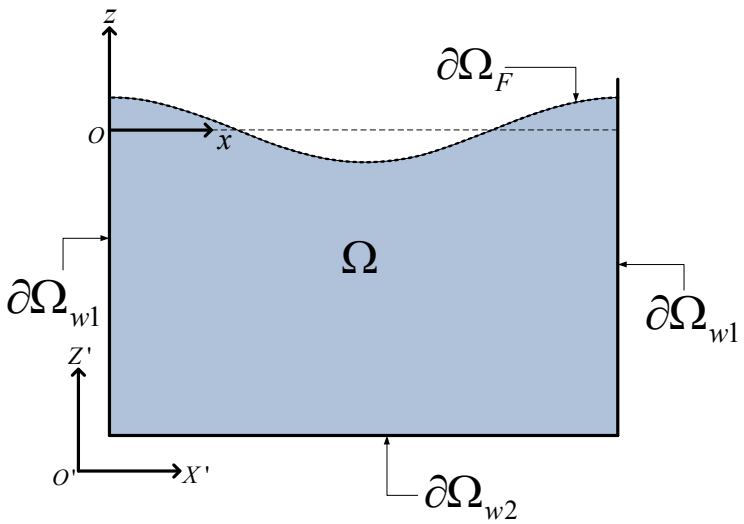

Figure 8.1. Representation of the boundaries in the 2D sloshing problem.

Table 8.1. IC and BC for Test Cases

Test Case	I.C	B.C's
Free Sloshing	$\eta^0 = a\cos(k_n x),\ \text{on}\ \partial\Omega_F$ $\phi^0 = 0,\ \text{on}\ \partial\Omega_F$	$\phi_x^t = 0,\ \text{on}\ \partial\Omega_{w1}$ $\phi_z^t = 0,\ \text{on}\ \partial\Omega_{w2}$
Lateral Excitation	$\eta^0 = 0,\ \text{on}\ \partial\Omega_F$ $\phi^0 = 0,\ \text{on}\ \partial\Omega_F$	$\phi_x^t = a_h \sin(\omega_h t),\ \text{on}\ \partial\Omega_{w1}$ $\phi_z^t = 0,\ \text{on}\ \partial\Omega_{w2}$
Vertical Excitation	$\eta^0 = a\cos(k_n x),\ \text{on}\ \partial\Omega_F$ $\phi^0 = 0,\ \text{on}\ \partial\Omega_F$	$\phi_x^t = 0,\ \text{on}\ \partial\Omega_{w1}$ $\phi_z^t = a_v \sin(\omega_v t),\ \text{on}\ \partial\Omega_{w2}$
Combined Excitations	$\eta^0 = 0,\ \text{on}\ \partial\Omega_F$ $\phi^0 = 0,\ \text{on}\ \partial\Omega_F$	$\phi_x^t = a_h \sin(\omega_h t),\ \text{on}\ \partial\Omega_{w1}$ $\phi_z^t = a_v \sin(\omega_v t),\ \text{on}\ \partial\Omega_{w2}$

The IC's may be supplied in the form of ϕ and η values, which when both equal to zero denote a fully stationary tank at rest. The stationary IC is adequate for the test cases with lateral excitations and combined excitations. For the vertical excitation and free sloshing cases, an initial surface perturbation is required. In these cases, it was decided to only supply the system with the position of the free surface η as the IC, which represents a standing wave at rest. The k_n values of the standing wave descriptions in Table **8**.**1**. are calculated from:

$$k_n = \frac{n\pi}{l} \tag{8.2}$$

where n is the wave number, and l is the tank length. Figure 8.2 demonstrates first three modes in 2D rectangular tanks.

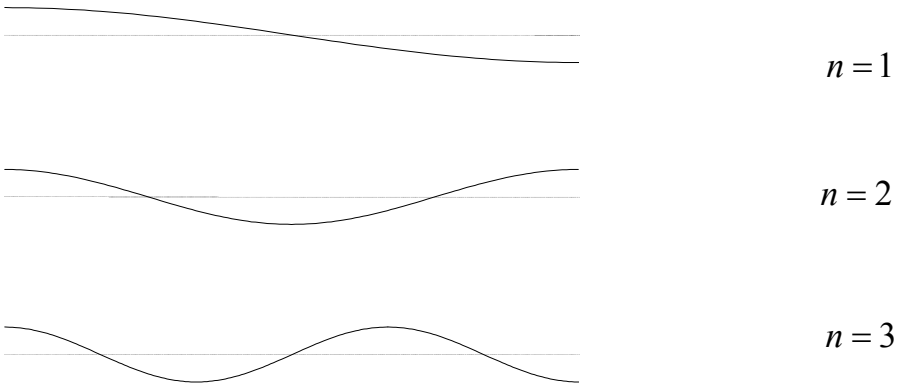

Figure 8.2. Representation of standing wave with wave number $n=1$, $n=2$, and $n=3$.

It can be observed that for each n, the mean free surface level is the stationary free surface level.

Physically, it is not possible to form a case simultaneously having non-zero η and zero ϕ on the surface. In some studies the test for fixed tanks are performed by first exciting the tank laterally for a given amount of time, and then stopping the tank and observing free sloshing. The current approach however, helps understanding the time evolution of a single given mode which is also the approach of our benchmarks.

As for the boundary conditions, being in line with the mathematical formulation in Figure 3.2, the time dependent velocity components are input to the model. The velocities are taken to be harmonic. Alternative mathematical formulations which allow acceleration inputs are also available.

For any practical applications of the model, such as inputs of earthquake motions, the velocity or the acceleration data with respect to time should be taken. The only requirement for analysis is to supply the model with these time varying bottom and wall boundary conditions.

It should be noted that in some studies, the harmonic excitations were provided to the system in form of cosine waves. Exciting the system with a cosine wave means initiation of the system with a non-zero velocity, which affects model behavior. Faltinsen *et al.* (2000) describes the types of inputs as impulse or zero initial conditions. A sensitivity study in their studies suggests that impulse conditions represent the lab conditions better in cases with shallow water depths. Varying excitation frequencies are also influential factors. A more in depth discussion can be found in the study mentioned.

8.3. Standing Wave Case

This is the simplest of the test cases in the sense that no time dependent boundary conditions are required. A standing wave is inputted to the system as the initial condition, and free sloshing is observed. It is also the easiest test case to verify. No dampers or viscous effects were specified in the mathematical formulation. The expectation from the model is to observe free sloshing oscillations at the corresponding sloshing mode frequency. For low-amplitude initial conditions, the expectation is also to maintain the initial maximum wave amplitude.

In Abramson (1966), the natural mode frequency is derived from the linear theory as:

$$\omega_n = \sqrt{g k_n \tanh(k_n h_s)} \tag{8.3}$$

where, k_n is defined in Equation (8.2), and h_s is the height of the stationary surface.

A second-order explicit derivation of the solution to the free sloshing problem from potential theory is provided in Frandsen(2004) as:

$$\eta(x,t) = a\left(c\cos(\omega_n t)\cos(k_n x) + \frac{a\omega_n^2}{g}\left(\frac{1}{8}\frac{\omega_n^4 + g^2k_n^2}{\omega_n^4} + \left(\frac{1}{8}\frac{3\omega_n^4 - g^2k_n^2}{\omega_n^4} - \frac{3}{2}\frac{\omega_n^4 - g^2k_n^2}{\omega_n^2\left(4\omega_n^2 - \omega_{2n}^2\right)} \right)\cos(2\omega_n t) \right.\right. \\ \left.\left. + \frac{1}{2}\frac{\omega_n^2\omega_{2n}^2 - \omega_n^4 - 3g^2k_n^2}{\omega_n^2\left(4\omega_n^2 - \omega_{2n}^2\right)}\cos(\omega_{2n} t) \right)\cos(2k_n x) \right) \tag{8.4}$$

where $\omega_{2n} = \sqrt{g2k_n \tanh(2k_n h_s)}$.

In the test cases, a tank with height $h = 5\text{m}$ and length $l = 10\text{m}$ was modeled. First and third mode standing waves were tested for free sloshing. The amplitudes of the standing waves were taken in the linear range.

In the present runs, the nodal layouts were taken as 11x6 for the first case and 25x13 for the second case. Increasing the number of nodes in the horizontal direction was necessary to catch the details of the standing wave with $n = 3$. Shape parameters were chosen as $6\, d_{\min}$ and $5\, d_{\min}$ respectively. Both values were adjusted by trial and error. Timestep was chosen to be 0.0002s for this tank.

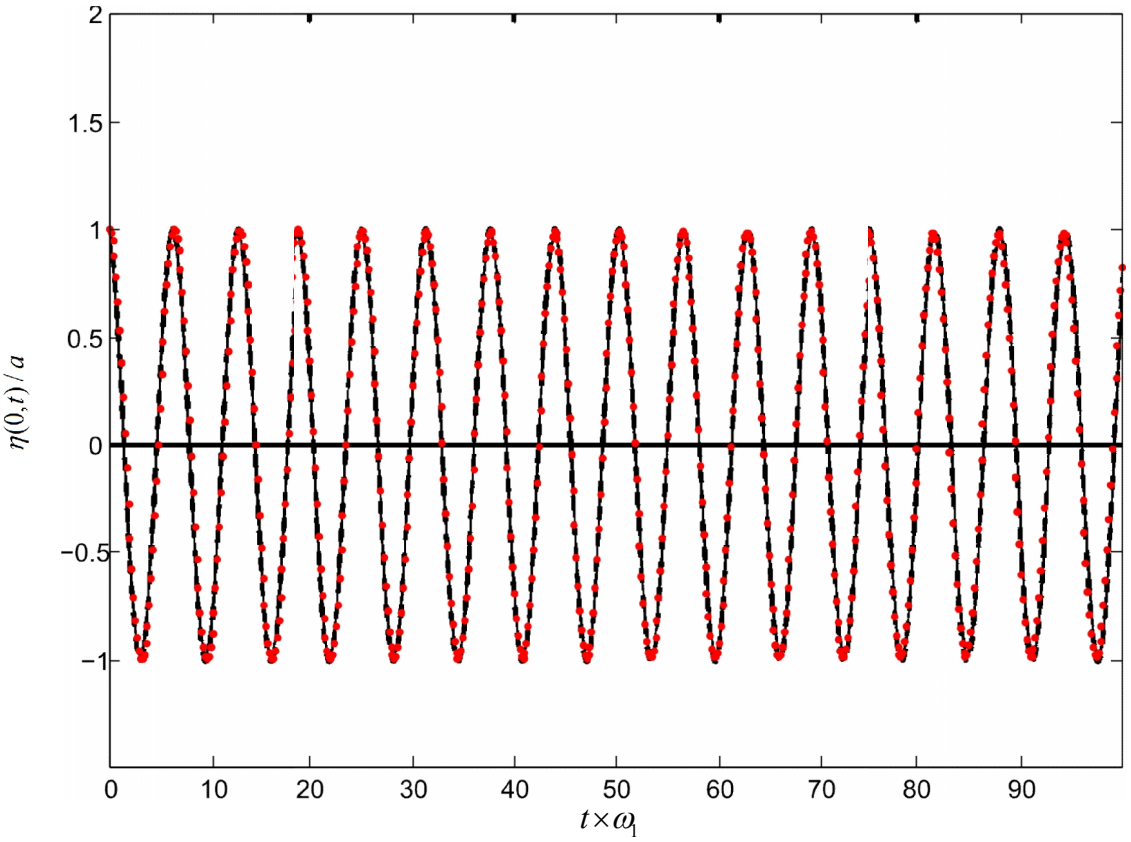

Figure 8.3. Free surface elevation for free sloshing at the left wall in fixed tank $n=1, h=5\text{m}, l=10\text{m}, a=0.005m$ •Present Numerical Solution −·− Analytical Solution (Frandsen, 2004), — Numerical Solution(Frandsen, 2004).

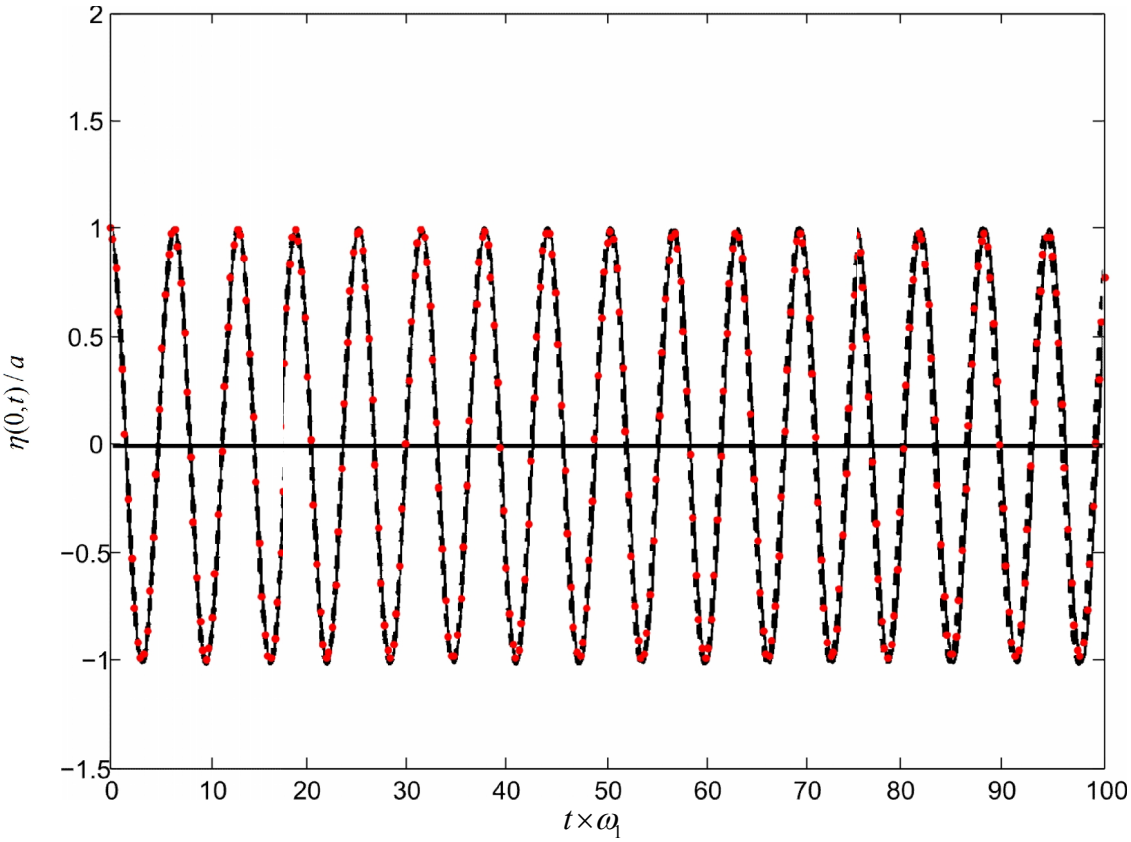

Figure 8.4. Free surface elevation for free sloshing at the left wall in fixed tank, $n=3, h=5\text{m}, l=10\text{m}, a=0.0015m$ •Present Numerical Solution −·− Analytical Solution (Frandsen, 2004), — Numerical Solution (Frandsen, 2004).

Both standing wave cases were run for 20 periods. Figure 8.3 and Figure 8.4 compare present numerical solution to the analytical solution from Frandsen (2004). It can be seen that the present results are in excellent agreement with the analytical theory in both of the cases. Because the test cases are low amplitude, the nonlinear terms in the free surface boundary conditions have negligible effects on the free surface amplitudes. Therefore the solution keeps the maximum wave amplitude constant throughout the case.

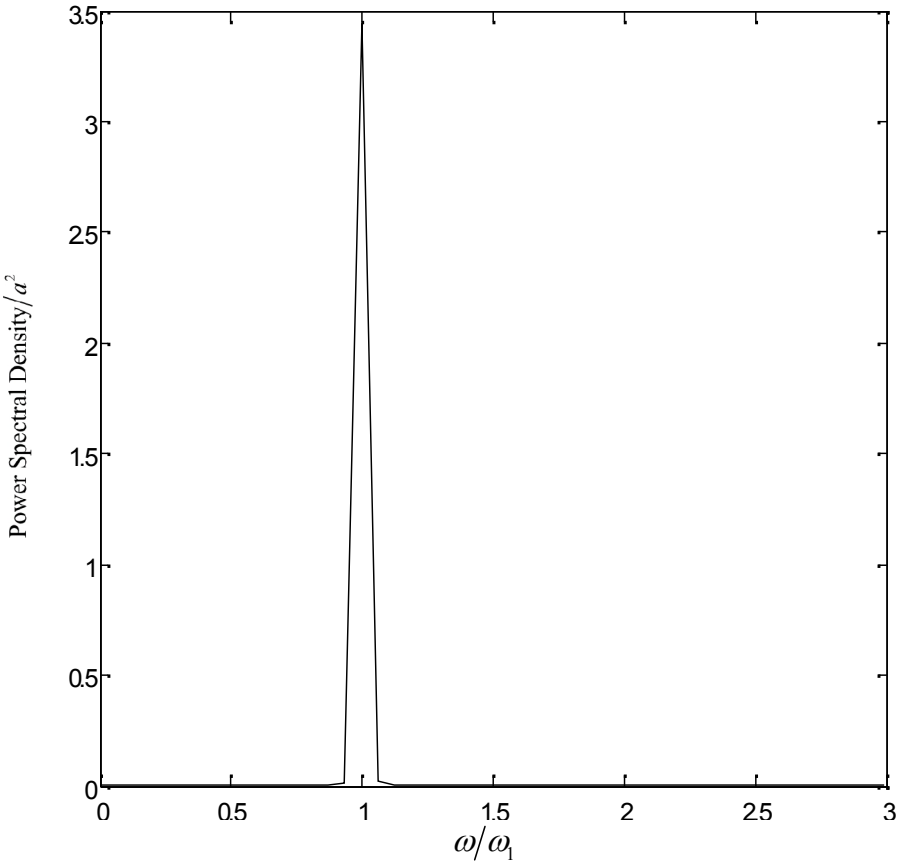

Figure 8.5. Spectra of the Free sloshing model with $n=1$.

The analysis of the output waves in the frequency domain are presented in Figures 8.5 and 8.6. The x axis shows the frequencies normalized with the corresponding resonant frequencies. The y axis shows the power spectral density output, which has the dimensions power per hertz and is a measure of the energy at various frequencies. It is computed using Matlab's discrete transformation algorithm fast-Fourier transform (FFT), and the complex conjugate. This value is also normalized with the input wave amplitude. It can be seen that the spectra display the fundamental sloshing frequencies. The output wave records show that only a single harmonic is present with frequency $\omega=\omega_1$ for the first case and $\omega=\omega_1$ for the second case.

Figures 8.7 and 8.8 show the comparisons of the surface profiles at different instants throughout the runs. It can be seen that the maximum amplitude conservation is achieved throughout the runs, with no minor waves or distortions in the surface profiles.

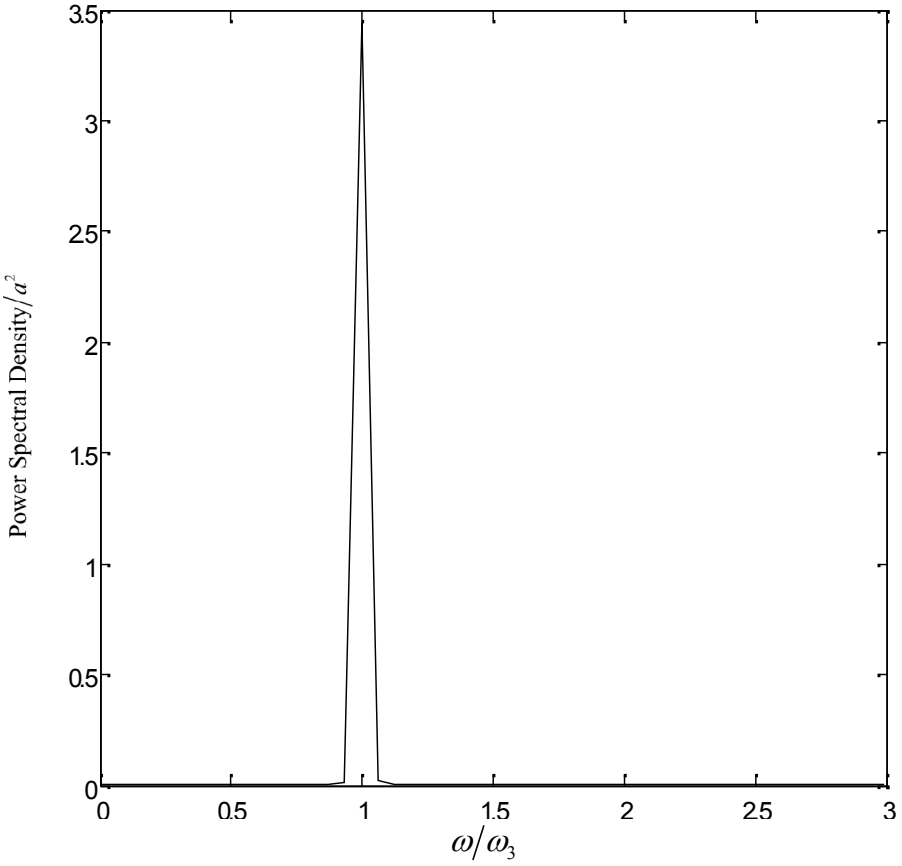

Figure 8.6. Spectra of the Free sloshing model with $n = 3$.

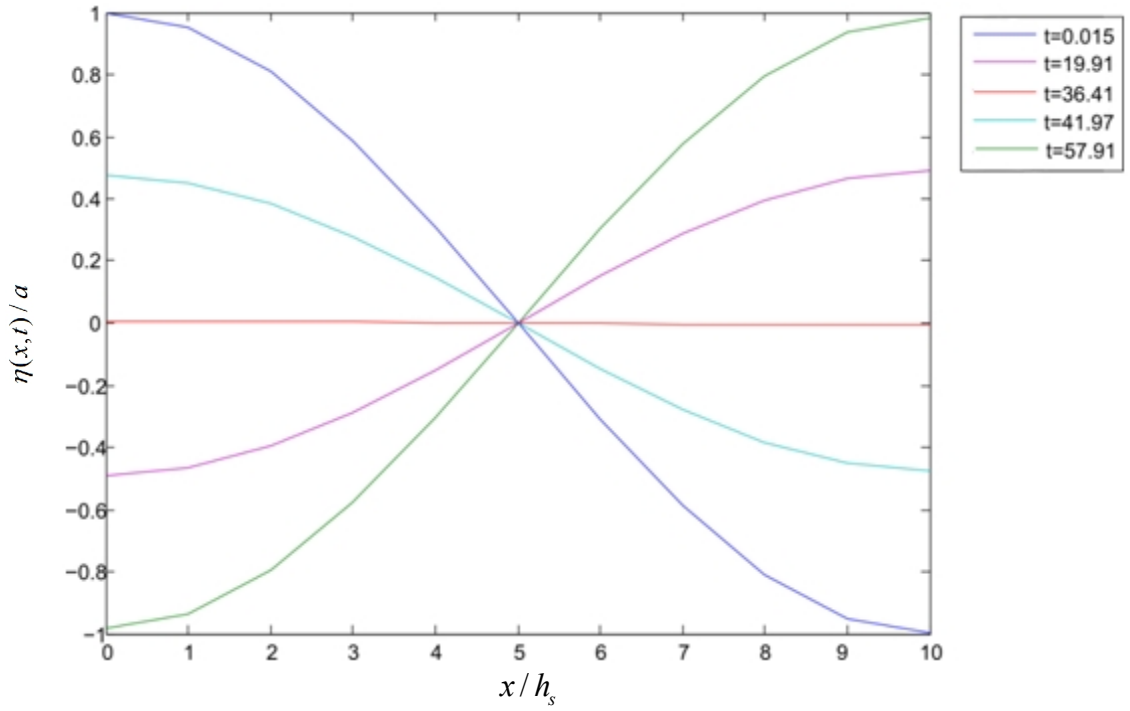

Figure 8.7. Surface Profiles at time t in Seconds, for Standing Wave Input with $n=1$.

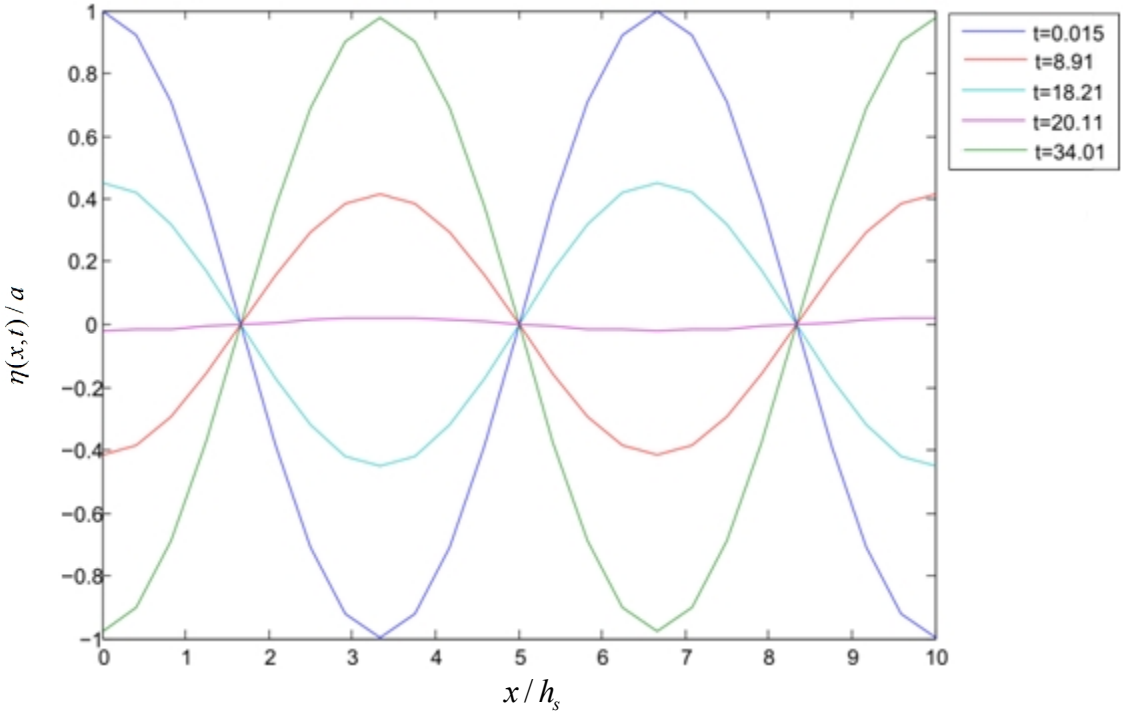

Figure 8.8. Surface Profiles at time t in Seconds, for Standing Wave Input with $n=3$.

8.4. Vertical Excitation Case

Vertical excitation case is a rather complex but important case. In earthquake induced ground motions, vertical components may exist; and a sloshing model for tanks should be able to handle such excitations. Even though pure vertical sloshing is not likely to occur in real sloshing problems, and it is very difficult to test in laboratory conditions; it is a case that should be tested and verified for the sake of completeness.

A preliminary analysis shows that pure vertical sloshing is very similar to the free sloshing case. Its behavior can be perceived as free sloshing occurring in an environment with a time dependent gravitational acceleration. Therefore, in order for the vertical excitation to induce any motion on the fluid, there has to be an initial surface disturbance. For this purpose, a standing wave with wave number $n=1$ was provided to the system as the initial condition.

The literature for this case is limited compared to lateral sloshing. One of the most important studies on the subject was performed by Benjamin and Ursell (1954). In this study, the stability of the vertical sloshing motion was examined, and an analytical solution was derived. The problem is formulated with Eulerian equations of motion, and the solutions are provided in form of Mathieu's functions. The solutions to the Mathieu's functions may be unstable depending on certain parameters. The envelope for the stability of the solution was developed based on the excitation amplitude and frequency.

A more recent study on the subject was performed by Frandsen and Borthwick (2003), in which an asymptotic third order solution was derived, a numerical model was coded and extensive discussion on the motion was carried out. The behavior of the fluid under excitations in the unstable region was characterized as Parametric Resonance. One may refer to Frandsen and Borthwick (2003) for detailed explanation on the subject.

Within the context of this study, stable motions were examined, and high amplitude motions were avoided. Figure 8.9 shows the stability region defined in Frandsen and

Borthwick (2003) and the blue circle denotes the selected input for the pure vertical and combined lateral and vertical sloshing cases in this study.

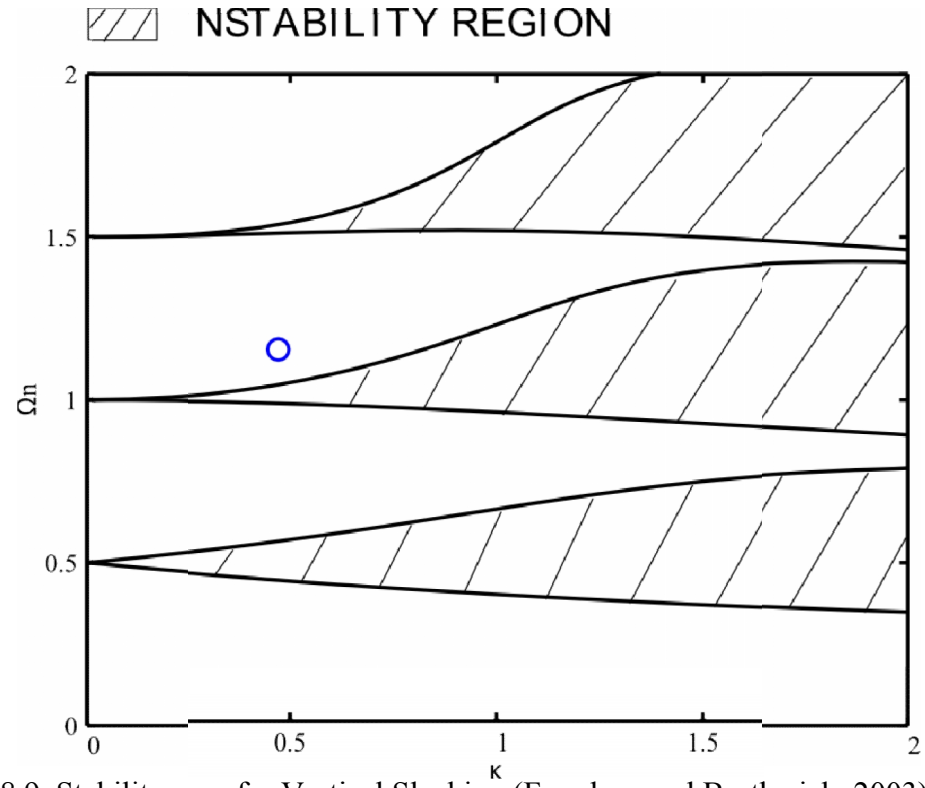

Figure 8.9. Stability map for Vertical Sloshing (Frandsen and Borthwick, 2003), where $\Omega = \omega_1/\omega_v, \kappa = a_v\omega_v^2/g$.

Vertical sloshing was tested for the same tank for free sloshing cases, with height $h = 5\text{m}$ and length $l = 10\text{m}$. Nodal layout of 21x11 nodes through the domain was taken for this model.

Figure 1.10 shows the comparison of the present model with the analytical and numerical result from Frandsen and Borthwick (2003). The system was vertically excited with $V_z = a_v \sin(\omega_v t)$ and with $a_v = 2.72\text{m}$ and $\omega_v = 0.8 \cdot \omega_1$. It can be seen that the phase and amplitude of the analysis compare well for this input.

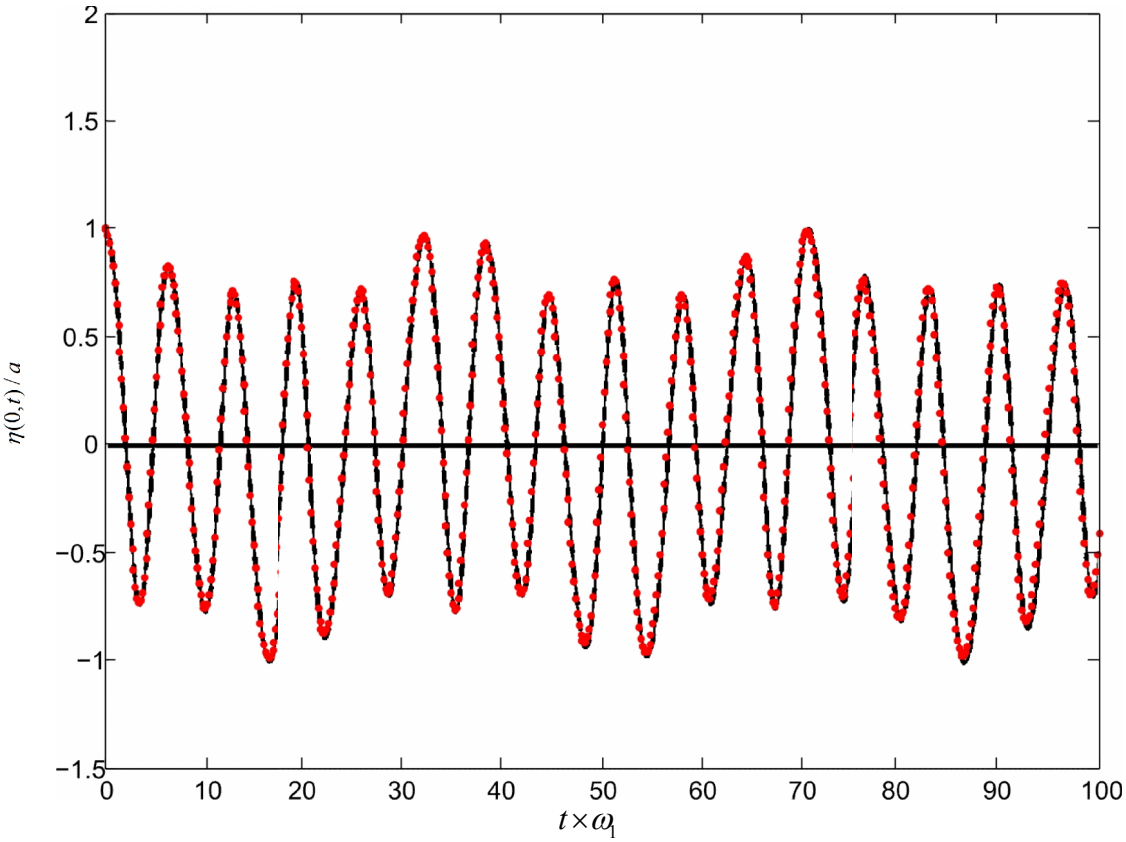

Figure 8.10. Free surface elevation for vertical sloshing at the left wall •Present Numerical Solution −·− Analytical Solution (Frandsen, 2004), — Numerical Solution(Frandsen, 2004) $h=5\text{m}, l=10\text{m}, a=0.005\text{m}, a_v=2.72\text{m}, \omega_v=0.8\cdot\omega_1$.

8.5. Lateral Excitation Case

In this section, investigations of horizontally excited 2D numerical tanks are undertaken. Lateral excitation case is the most extensively studied 2D case in this thesis. This is because of the abundance of the resources on this type of sloshing. The numerical predictions of the free surface motions are compared to both the analytical, numerical, and experimental studies from the literature.

The excitation frequencies of the test cases are selected relative to the first resonant frequency. Low amplitude excitations were applied at off resonance and at resonance frequencies in the initial studies. Next, the excitation amplitudes were increased to examine

the nonlinearity handling capabilities of the RBFCM models. Comparisons with the experimental test cases are also included in this section.

For the lateral excitation cases, the system starts from stationary "at rest" condition. So both ϕ and η are equal to zero at time $t = 0$. Harmonic excitations in the form $a_h \sin(\omega_h t)$ are applied to the lateral boundaries, with the maximum excitation amplitude a_h and the excitation frequency ω_h remaining constant throughout the runs.

The first two cases are from Frandsen (2004), where a modified-sigma transform FDM model was constructed and a third order asymptotic solution to the velocity potential was developed.

Off resonant frequencies at $0.7 \cdot \omega_1$ and $1.3 \cdot \omega_1$ are used for horizontal excitations. The modeled tanks have height $h = 5\text{m}$ and length $l = 10\text{m}$ as in the previous cases, and the excitation amplitudes were selected in the linear region. The nodal layout was kept at 21x11 nodes.

The two cases in Figures 8.12 and 8.13 show perfect fits to the third order solution and the numerical solution from Frandsen (2004). When both graphs are analyzed, it can be seen that maximum sloshing wave amplitude is about 2.5 times the excitation amplitude for the sub harmonic case and it is about 5 times the excitation amplitude for the super-harmonic case.

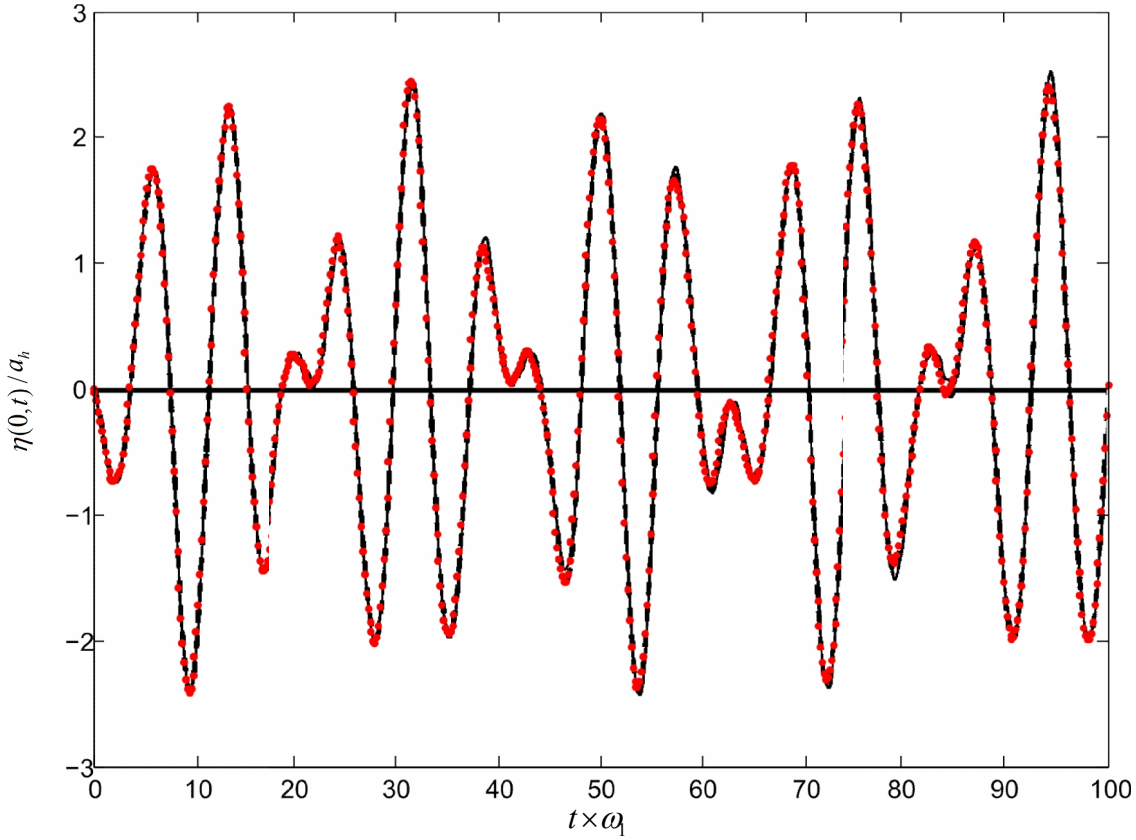

Figure 8.11. Free surface elevation for lateral sloshing at the left wall • Present Numerical Solution −·− Analytical Solution (Frandsen, 2004), — Numerical Solution(Frandsen, 2004) $h=5\text{m}, l=10\text{m}, a_h=0.01m, \omega=0.7\cdot\omega_1$.

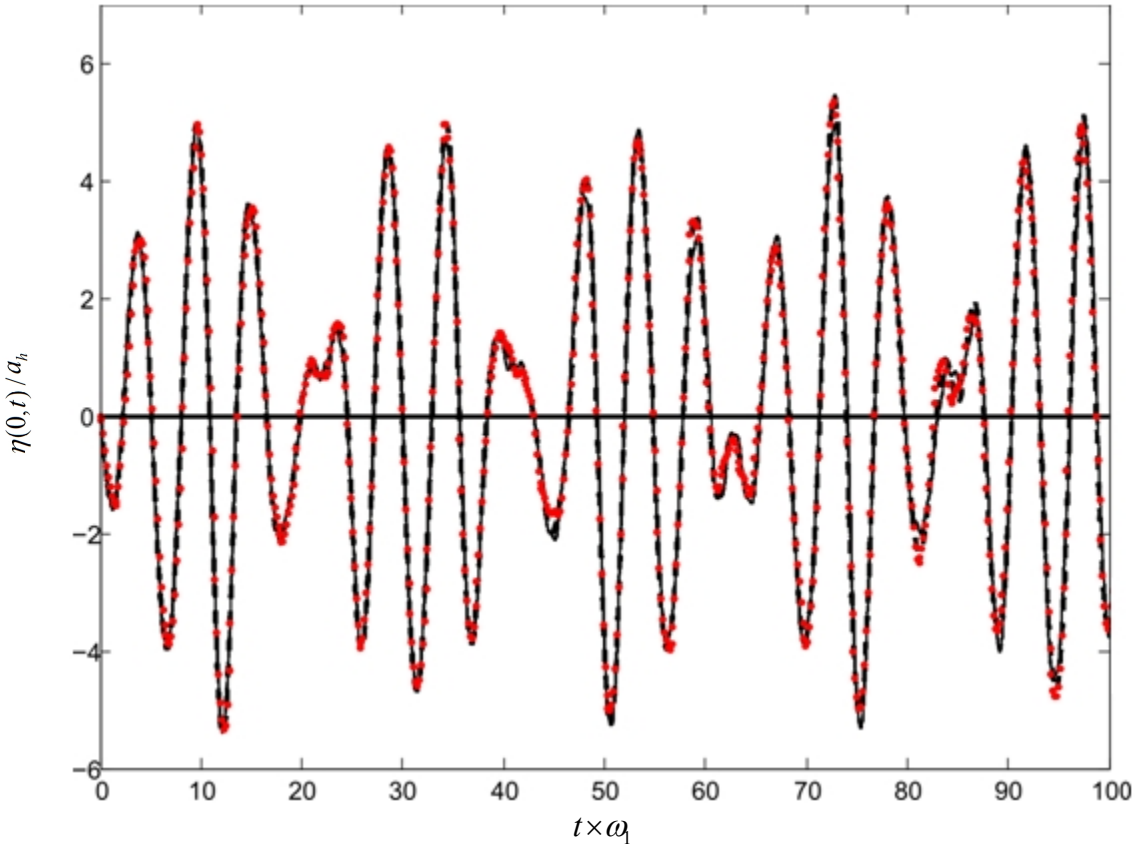

Figure 8.12. Free surface elevation for lateral sloshing at the left wall • Present Numerical Solution −·− Analytical Solution (Frandsen, 2004), — Numerical Solution(Frandsen, 2004) $h = 5\text{m}, l = 10\text{m}, a_h = 0.01m, \omega = 1.3\cdot\omega_1$.

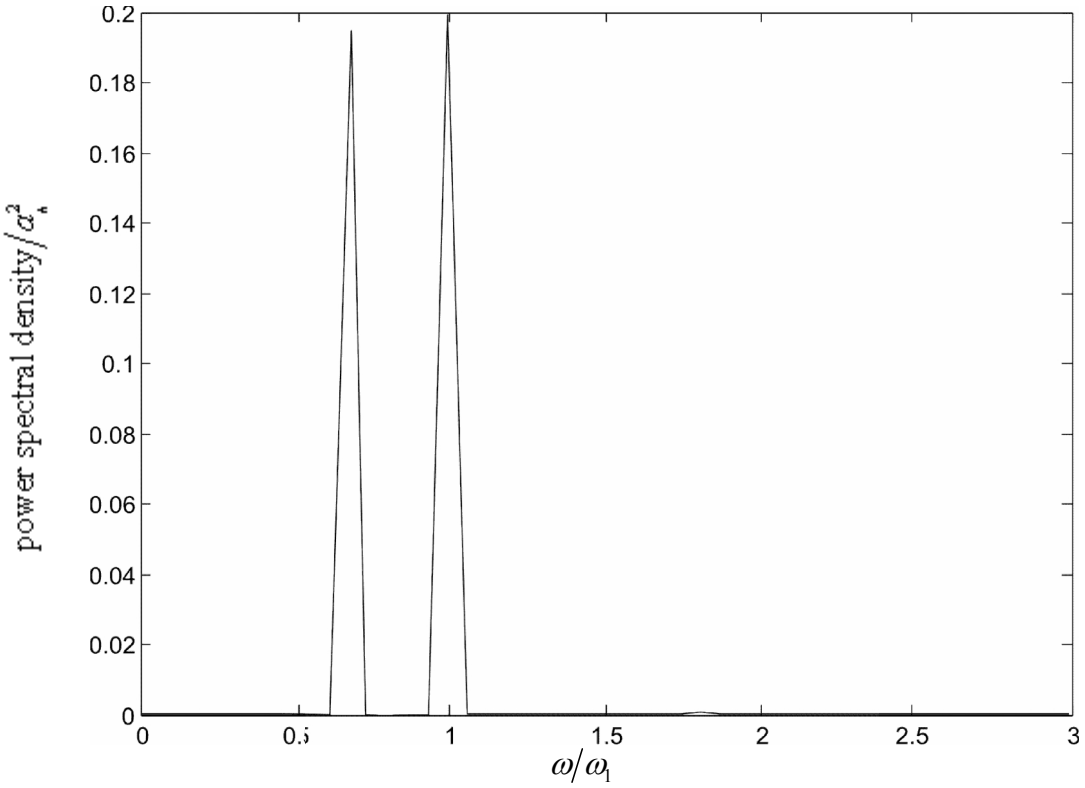

Figure 8.13. Energy Spectrum for Low Amplitude Lateral Sloshing Case with $\omega = 0.7 \cdot \omega_1$.

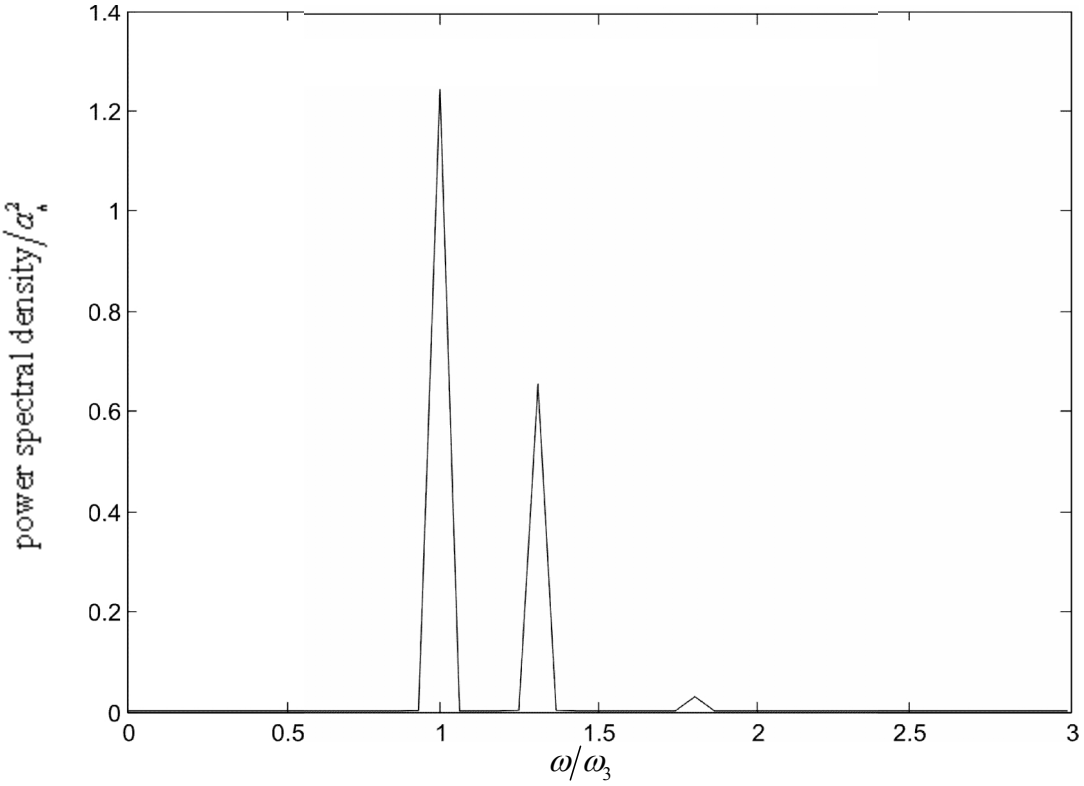

Figure 8.14. Energy Spectrum for Low Amplitude Lateral Sloshing Case with $\omega = 1.3 \cdot \omega_1$.

Figures 8.13 and 8.14 show the power spectrums for the both cases. Energy contents at the first natural frequency and at the excitation frequency are present. An additional low energy content spike is present for the super harmonic case, which is at the third natural frequency. The deviations from the analytical solution are thought to originate from this spike.

The next test case was taken from Liu and Lin (2008). A tank with dimensions $h = a = 0.5\text{m}$ to $l = 2a = 1\text{m}$ was excited at the near resonant frequency $0.95 \cdot \omega_1$. Comparing to the previous cases, the tank dimensions were lowered, and the first natural mode frequency of the system was nearly doubled. Therefore the time step was adjusted to be 0.0001 for this case. In this case, the excitations were applied in the form $a_h \cos(\omega_h t)$, where $a_h = b\omega_h$, b being the displacement amplitude. This is the impulse initial condition explained in Section 8.2. The results in this study were compared to the second order solution from Faltinsen (1978).

The 2nd order analytic implicit solution from Faltinsen (1978), which was used to verify their numerical model and experimentation was given as:

$$\zeta(x,t) = \frac{1}{g}\sum_{n=0}^{\infty} \sin\left(\frac{(2n+1)\pi}{2a}x\right)\cosh\left(\frac{(2n+1)\pi}{2a}h\right)\left[-A_n\omega_n \sin\omega_n t - C_n\omega \sin\omega t\right] - \frac{1}{g}a_h\omega x \sin a$$

$$\omega_n^2 = g\frac{(2n+1)\pi}{2a}\tanh\left(\frac{(2n+1)\pi}{2a}h\right), C_n = \frac{\omega K_n}{\omega_n^2 - \omega^2}, A_n = -C_n - \frac{K_n}{\omega}, \tag{8.5}$$

$$K_n = \frac{\omega a_h}{\cosh\left(\frac{(2n+1)\pi}{2a}h\right)}\frac{2}{a}\left(\frac{2a}{(2n+1)\pi}\right)^2 (-1)^n$$

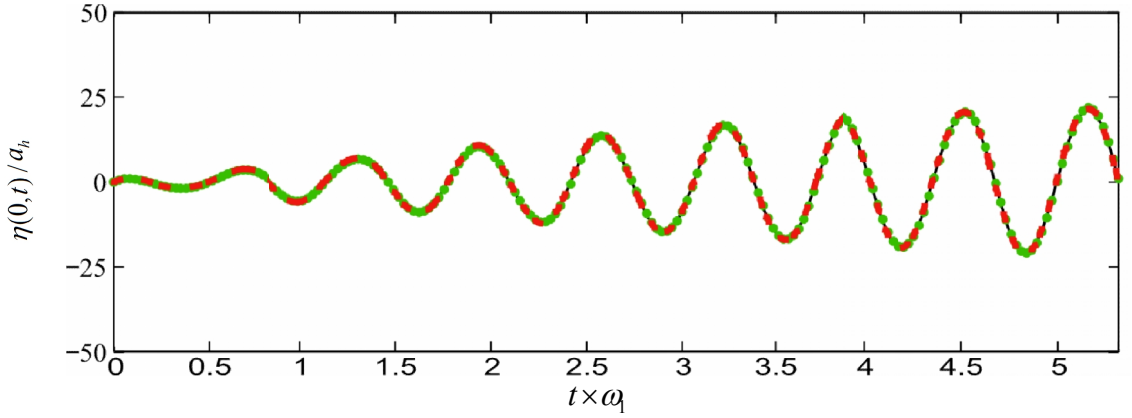

Figure 8.15. Free Surface Elevation for Lateral Sloshing at the Left Wall wall • Present Numerical Solution, –Analytical Solution (Faltinsen, 1978), • Numerical Solution(Liu and Lin,2008) $h=0.5\text{m}, l=1\text{m}, a_h=0.0004\text{m}, \omega=0.95\cdot\omega_1$.

Figure 8.15 demonstrates an excellent fit to the low amplitude, resonant excitation case.

For the next series of test cases, the amplitudes were drastically increased to enforce surface motions that are not possible catch by linear theory. When the forcing amplitudes increase, the nonlinear terms in the free surface boundary conditions grow large enough to have significance on the results. When the standard procedures in Chapter 5 are used for these cases, the accuracy and stability of the models are not as good as other cases. Handling the problems associated with high free surface boundary deformations is a topic subject to intense contemporary research. For example, in Frandsen (2004), the domain was discretized with sigma transformation, and in Liu and Lin (2008) the second order volume of fluid method was used to track the free surface. In this study, the models were modified by means of changing the locations and numbers of RBF and collocation centers, and applying certain filtration and correction techniques to the results. These techniques are reviewed in the Appendix section of this thesis.

The first case analyzed in this manner was an off-resonant case with forcing frequency of $\omega=0.5\omega_1$ and with a forcing amplitude of $a_h=0.1\text{m}$ on a 0.5m by 1m tank. In this model, the stability was maintained by using 295 collocation centers, and reducing

the number of RBF centers to 257. RBF centers were placed in between the collocation nodes, and 3 additional rows of RBF centers were placed close to the surface, as shown in Figure 8.16.

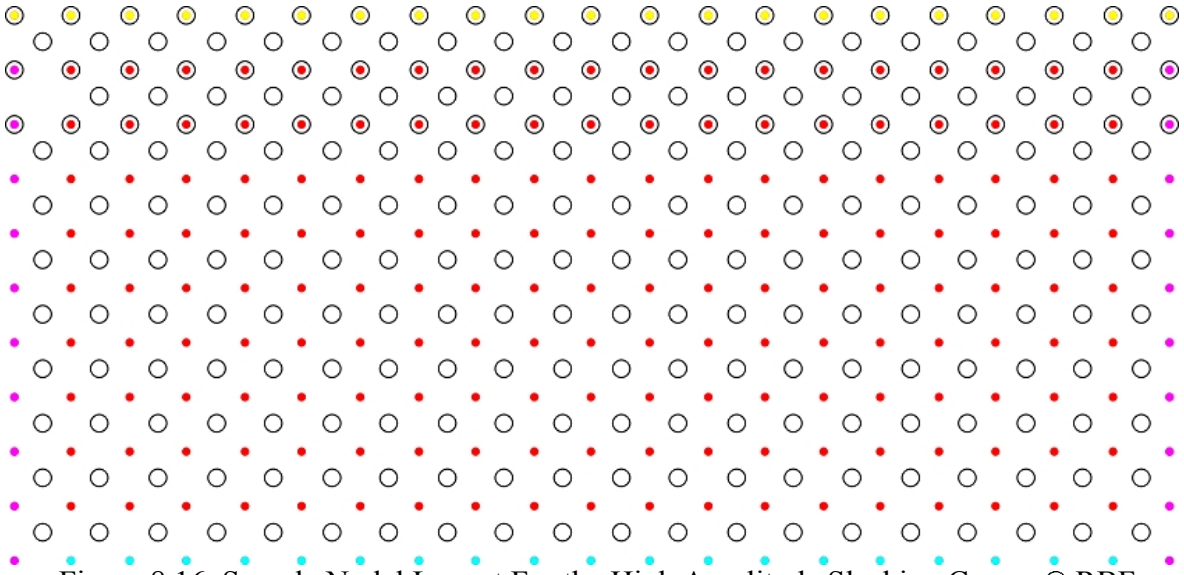

Figure 8.16. Sample Nodal Layout For the High Amplitude Sloshing Cases; ○ RBF Centers, • Collocation Centers.

The resultant over-determined system produced a non-square system matrix. Solution to this system was achieved by using the nonlinear least squares approach. This approach yielded more stable and smoother results. Also, the shape parameter was optimized every 1000^{th} time step by trying 20 different shape parameters to estimate the Laplacian throughout the domain, and selecting the one that yielded the least RMS error. The shape parameters that were tested were set to be in the region ±20% of the previous shape parameter. A more detailed explanation is provided in the appendix. The result was compared to the second order solution from Faltinsen (1978).

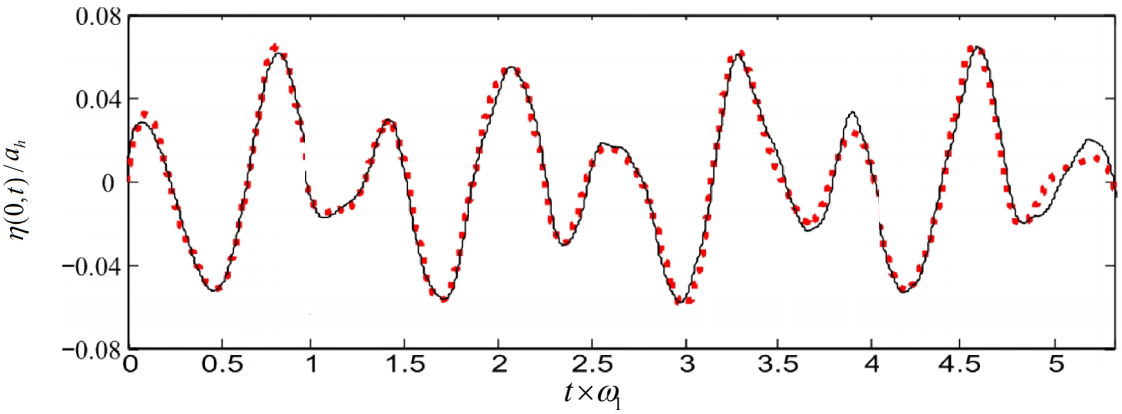

Figure 8.17. Free surface elevation for horizontal sloshing at the left wall

•Present Numerical Solution, —Analytical Solution (Faltinsen, 1978),

$h = 0.5\text{m}, l = 1\text{m}, a_h = 0.05\text{m}, \omega = 0.5 \cdot \omega_1$.

This motion was in the impulse form $a_h \cos(\omega_h t)$, and it initiated with a non-zero velocity. The discrepancies due to the impact effect are evident in the results. However, the graph shows minimal deviation of the peak surface amplitudes. The maximum difference in from the analytical solution normalized with the excitation amplitude is 20%, and the mean difference is 6%.The phase of the wave is also in harmony with the analytical result.

The next test case was taken from Frandsen (2004). Tank with dimensions 5m by 10m was excited at frequency $\omega = 0.7\omega_0$. The results were compared to the analytical results and the numerical results from Frandsen (2004). For this model, 21x11 nodal layout was chosen with 295 collocation nodes. 255 RBF nodes were taken, and RBF centers were concentrated near the surface boundary. The shape parameter was optimized every 1000^{th} time step. When calculating the derivatives for η, the approach of using less number of RBF centers was used by collocating the free surface using 16 RBF centers every 2000^{th} time step.

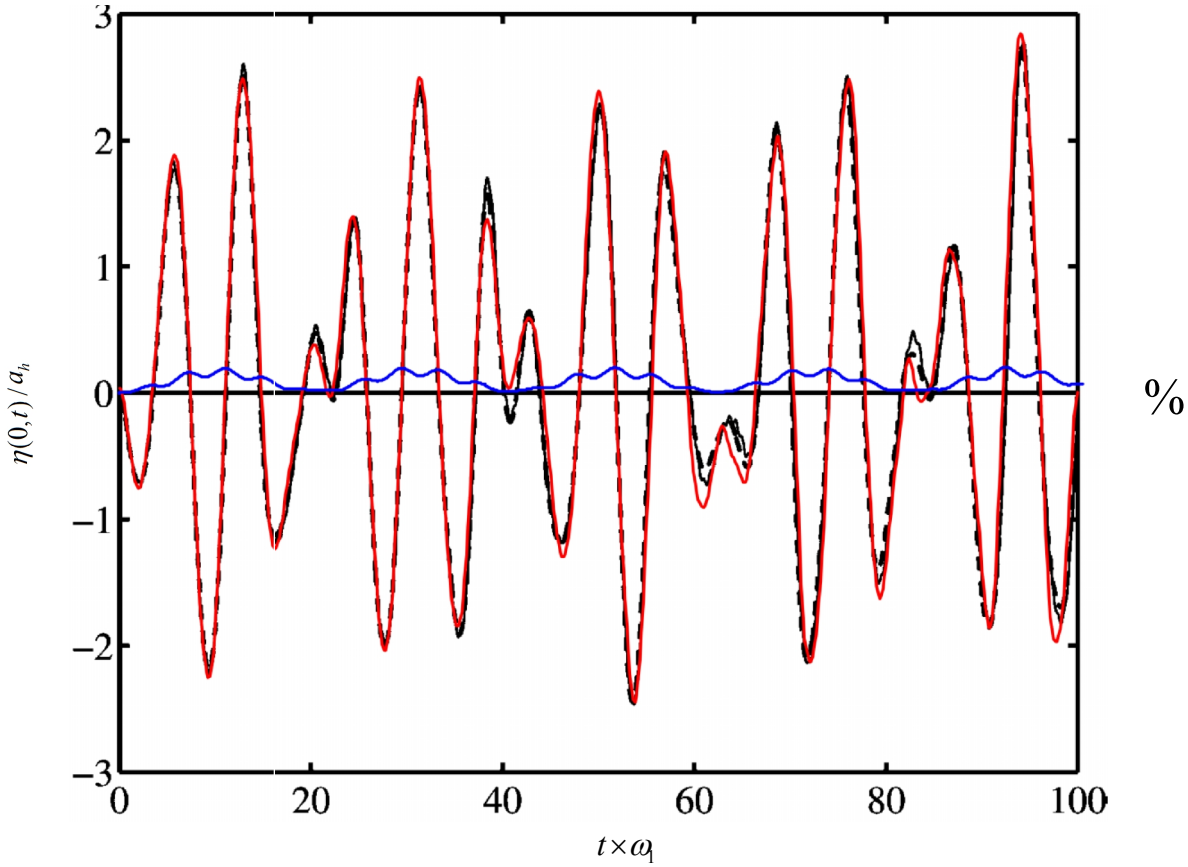

Figure 8.18. Results for Lateral Sloshing ——Present Numerical Solution –·– Analytical Solution (Frandsen, 2004), — Numerical Solution(Frandsen, 2004), —— Percent Mass Difference $h=5\text{m}, l=10\text{m}, a_h=0.255\text{m}, \omega=0.7\cdot\omega_1$.

When the graph is analyzed, it can be seen that the peak surface amplitudes rise as high as to three folds the excitation amplitude; which means peaks of about 15% and troughs of about 10% of the initial fluid depth. This causes dramatic distortions on the computational domain, and causes the difference from the results from Frandsen (2004).

There is a drop in the accuracy of the derivatives evaluated at the free surface boundary because of the distortion on the computational domain. This results in some error accumulation and a change in the fluid mass, which manifests itself as a deviation in the mean water level of the tank. The blue line in the graph shows the change of fluid mass throughout the run and shows that it is maintained to stay within 0.1%.

The next test case in the nonlinear range is taken from the laboratory experimental studies of Liu and Lin (2008). In the experiment, a 0.30m by 0.57m tank was constructed and filled to 0.15m in liquid depth. The tank was equipped with three wave probes at each side and in the middle of the tank as shown in Figure 8.19.

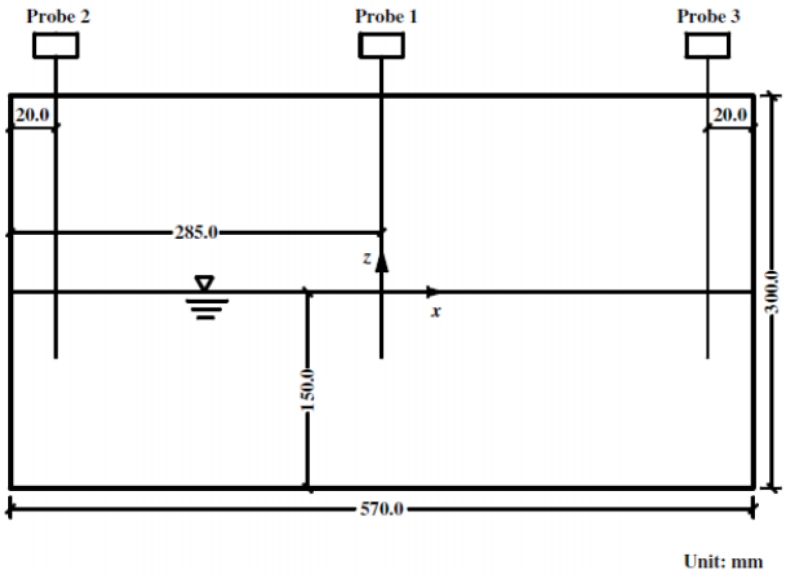

Figure 8.19. Experimental setup from Liu and Lin (2008).

The rectangular prismatic tank had a width of 0.31 m to simulate 2D sloshing. The tank was placed on the shaking table and an excitation frequency of $0.578 \cdot \omega_1$ was used in the first test. The movement of the shaker followed a harmonic excitation as $x(t) = -a\sin(\omega t)$ and the excitation amplitude was at $a = 0.005m$. The sinusoidal displacement input, when differentiated with respect to time, gave the velocity input necessary to be supplied to the model as the wall BC.

In the present model, this tank was modeled with a 20x6 nodal layout, with 172 collocation centers and 149 RBF centers. 12 RBF nodes were used the collocate the surface every 1000^{th} time step and the shape parameter was optimized every 1000^{th} time step.

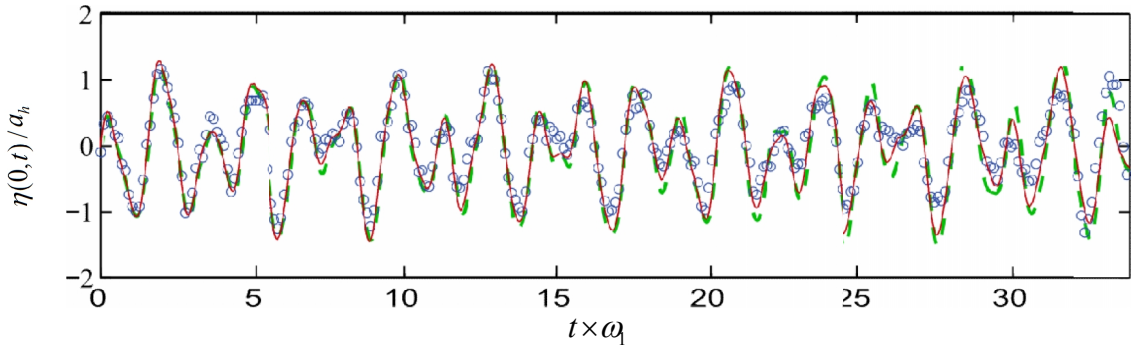

Figure 8.20. Free surface elevation for horizontal sloshing at the left wall —— Present Numerical Solution ○Experimental Results (Liu and Lin, 2008), - - - Numerical Solution (Liu and Lin, 2008) $h=0.15\text{m}, l=0.57\text{m}, a_h=0.005\text{m}, \omega=0.578\cdot\omega_1$.

In Figure 1.20, the comparison of present model with the numerical and experimental results from Liu and Lin (2008) can be seen. It should be noted that i the reference model, RANS was solved and turbulence was also included. It can be observed that the present model captures free surface motions of the experimental tank good enough to catch the phase, and the peak amplitudes with acceptable accuracy. Some peaks are over or under-represented, and for some peaks, the present model performs more accurate estimations than the reference model. Although there is room for improvement, the present model can be thought as a competitor to the popular numerical tanks in the literature.

The final horizontal excitation case applies high amplitude excitation to the experimental tank at the resonant frequency $\omega=\omega_1$. The aim is to see how the model performs under extreme conditions. The results are compared to the experimental and numerical results of Liu and Lin (2008).

For this model, 172 Collocation centers and 149 RBF centers were used, shape parameters were optimized at each time 1000$^{\text{th}}$ time step and then magnified by 10% to get optimum performance. 10 RBF nodes were used the collocate the surface every 1000$^{\text{th}}$. For this particular model, a mass conservation scheme was also applied every 1000$^{\text{th}}$ time step and details on that may be found in the Appendix section.

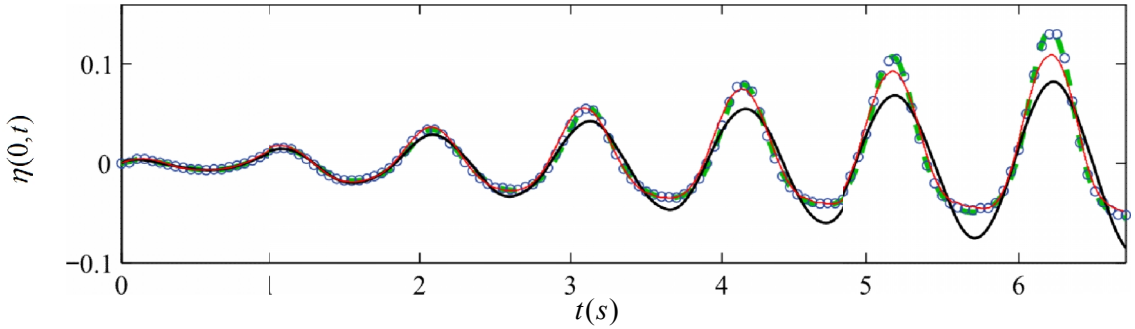

Figure 8.21. Free surface elevation for horizontal sloshing at the left wall —— Present Numerical Solution ○Experimental Results (Liu and Lin, 2008), - - - Numerical Solution (Liu and Lin, 2008), —Linear Solution,
$h = 0.15\text{m}, l = 0.57\text{m}, a_h = 0.005\text{m}, \omega = 1 \cdot \omega_1$.

Figure 1.21 compares results from the present model to the experimental and numerical results from Liu and Lin (2008). There is also a fourth wave, which shows the result from the linear theory. In the present results, the nonlinear phenomenon is evident with the higher peaks and shallower troughs in the surface elevation. However, it can be observed that during the end of the analysis, there exists a 10% difference between the present model and the experimental study.

It should be noted that the peak amplitudes reach to 0.12m in this case, which is about 80% of the mean free surface level. This is an unrealistic case for a real earth quake scenario. The system is excited at the resonant frequency for more than 6 periods at high amplitudes, which eventually causes the fluid to behave as a whole mass slamming each wall and reaching extreme amplitudes.

The deviations from the reference numerical model leave room for improvement on the behavior of the RBFCM at very high amplitude free surface deformations.

8.6. Combined Lateral and Vertical Excitation Case

This section examines situations when lateral and vertical excitation components are both present. All the boundary conditions are fully utilized for this type of cases.

With combined lateral and vertical excitation, the instability and/or resonance occurrence becomes more probable. For example, when the sum or difference of the lateral and vertical excitation frequencies coincides to a natural mode frequency, resonant motions can be observed. Therefore test cases should be carefully selected to ensure that the free surface amplitudes lie within the model limitations. Within the context of this study, the lateral and vertical excitation frequency and amplitude combinations are selected to avoid the instability region and mode interactions.

In these cases, the initial surface disturbance for the vertical excitations to take effect are supplied by the lateral excitations, therefore an initial condition with standing waves is not present. The system is initiated with a stationary free surface.

In Frandsen (2004) an extensive study is carried out on the combined excitation cases. The test cases for this study are selected from Frandsen (2004). The analyzed tank has height $h = 5\text{m}$ and length $l = 10\text{m}$ and a nodal layout of 21x11 nodes was taken. Both the cases were off-resonant cases.

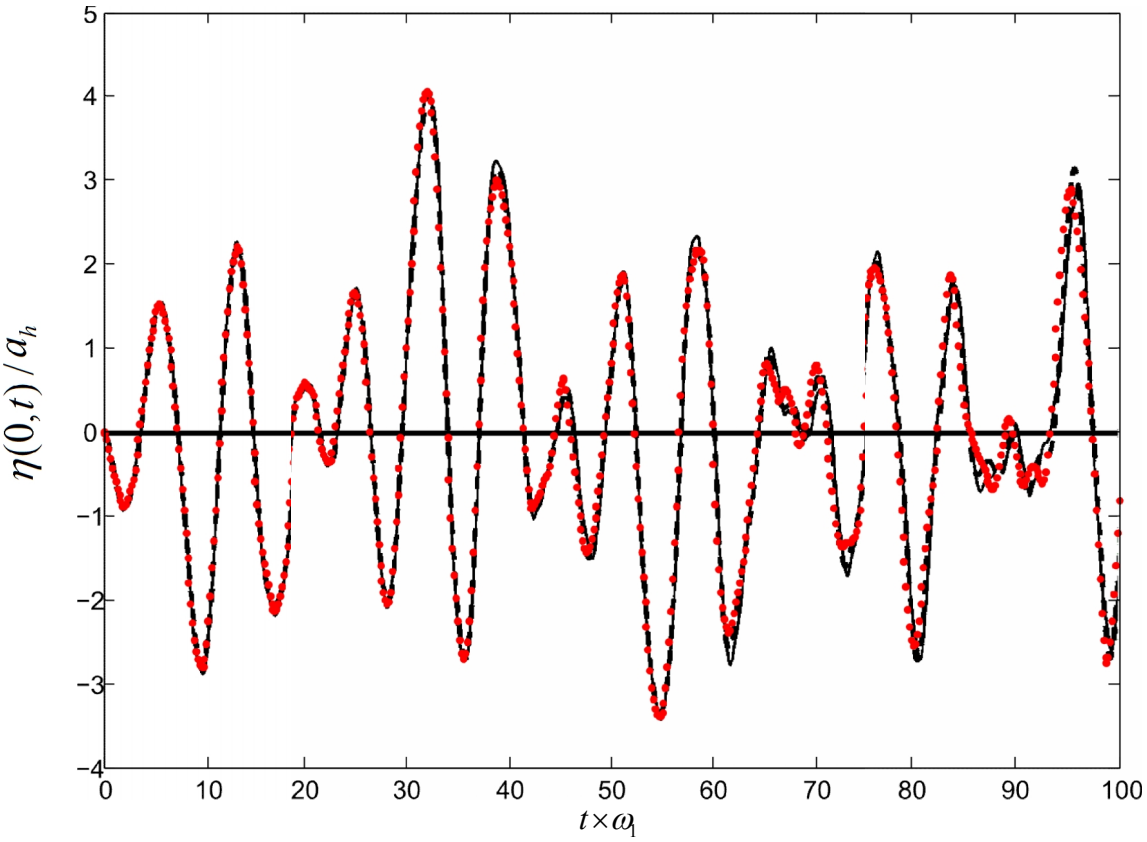

Figure 8.22. Free Surface Elevation for Combined sloshing at the Left Wall

•Present Numerical Solution −·− Analytical (Frandsen, 2004), — Numerical (Frandsen, 2004) $h=5\text{m}, l=10\text{m}, a_h=0.025\text{m}, a_v=2.72m, \omega_h=0.7\cdot\omega_1, \omega_v=0.8\cdot\omega_1$.

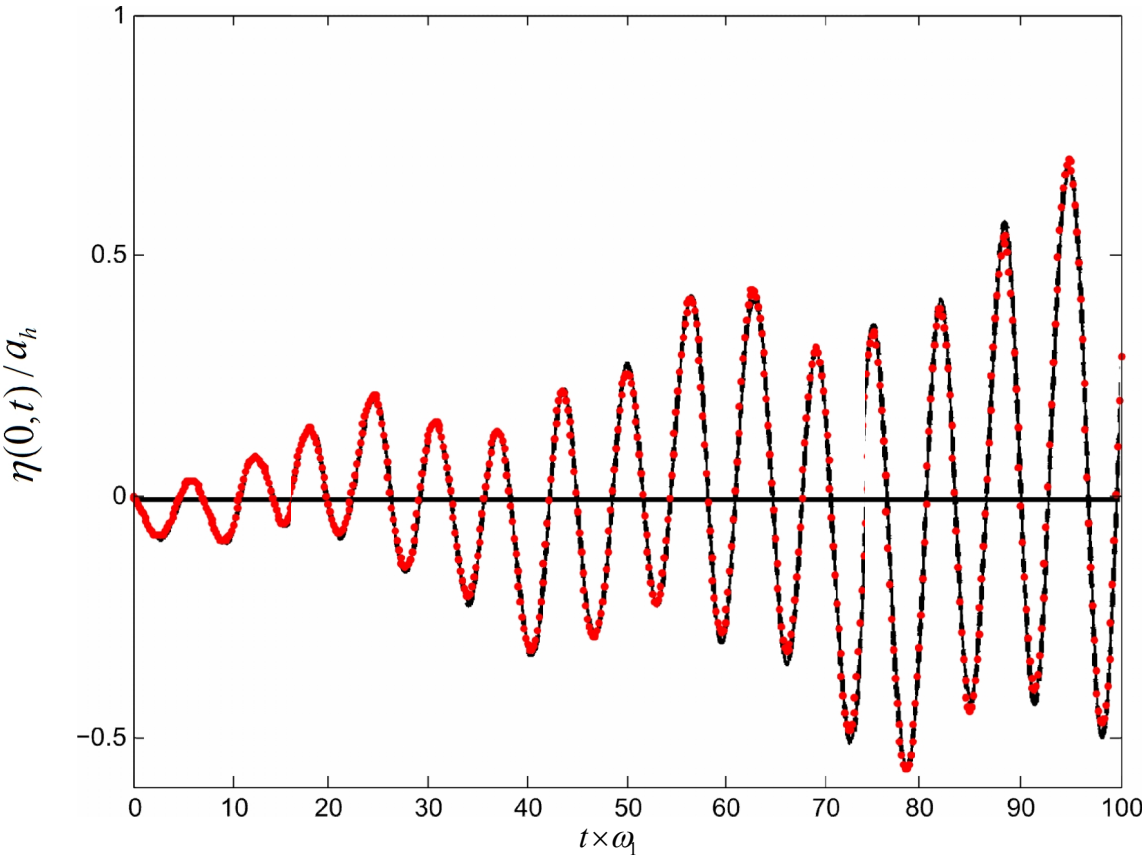

Figure 8.23. Free Surface Elevation for Combined sloshing at the Left Wall

●Present Numerical Solution −·− Analytical (Frandsen, 2004), — Numerical (Frandsen, 2004) $h=5\text{m}, l=10\text{m}, a_h=0.005\text{m}, a_v=2.72m, \omega_h=0.18\cdot\omega_1, \omega_v=0.8\cdot\omega_1$.

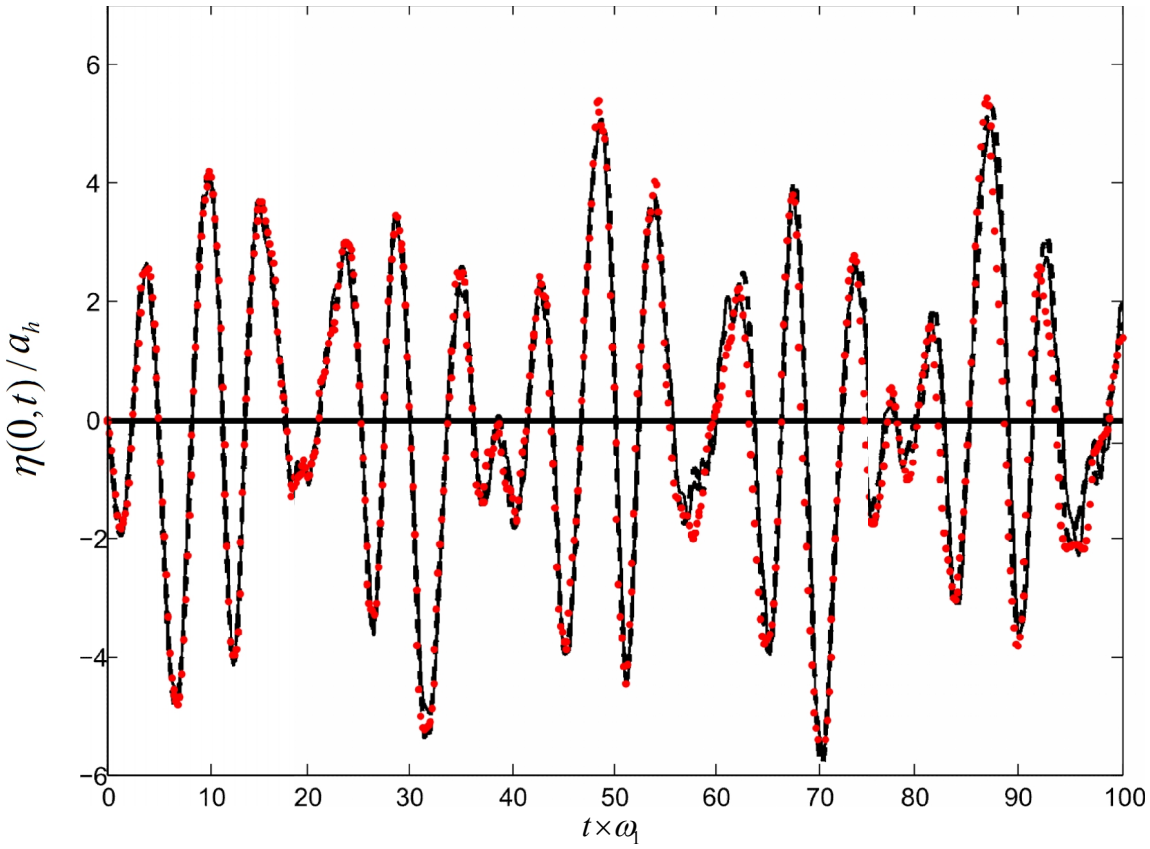

Figure 8.24. Free Surface Elevation for Combined sloshing at the Left Wall

Present Numerical Solution −·− Analytical (Frandsen, 2004), — Numerical (Frandsen, 2004) $h=5\text{m}, l=10\text{m}, a_h=0.0074\text{m}, a_v=2.72m, \omega_h=1.3\cdot\omega_1, \omega_v=0.8\cdot\omega_1$.

The test cases show excellent fits to the analytical and numerical results from Frandsen (2004), combined sloshing is demonstrated.

8.7. Comments on the Modeling Effort

The principle aim of this study was to create stable running models that could solve the sloshing problem. In a number of locations in this thesis, it was stated that RBFCM allows flexibilities in model development. Some of these flexibilities include the choice of nodal layout, choice of RBF, shape parameter, matrix symmetry, PDECB technique and many others.

In Chapter 5, a generic modeling approach was presented, and this approach can handle most low amplitude sloshing problems. However, in order to create the optimum solution, or any solution at all for some cases, each and every model has to be tailor made.

RBFCM is not like the conventional numerical techniques. Straightforward approach of applying techniques like mesh refinement or time step adjustment for increasing the accuracy may not applicable in RBFCM. Mesh refinement may even cause instabilities and increased errors. Behavior of the selected RBF is a key factor. For example, MQ is known to behave well in sparse, random node placement, and TPS is known to behave well in orderly and dense nodal alignment. Therefore it is important to choose a strategy for optimizing the models based on the behavior of the selected RBFs. Appendix provides an analysis on the subject.

The biggest challenges were faced especially in high amplitude sloshing cases where the precision of the results was highly dependent on accurate evaluation of the second order derivatives on the boundary. In these cases with extreme boundary deformities, classical RBFCM modeling technique was not sufficient. A more detailed explanation on the experimented numerical tricks are documented in the Appendix section. However, it should be noted that the accurate evaluation of the derivatives on the boundaries is also a problem in other numerical methods like FDM and FEM, and often these derivatives are treated specially in other models as well.

9. NUMERICAL TESTS AND RESULTS ON 3D SLOSHING

There were three different types of models to test in the 3D sloshing studies: RBFCM models, VMASS models and the laboratory experimentation models. Majority of this section compares the three types of models in their performances in estimating the sloshing mode frequencies. Methodology for testing the models; and an analysis on the design code is provided in the beginning. Then, comparative analysis of the models is provided for rectangular prismatic and cylindrical tanks. In the last section, simulation of a realistic cylindrical tank under earthquake motion is analyzed using the RBFCM and VMASS models.

9.1. Selecting the Variable to Test, and Criticism on the Experiments

The numerical models were based on the laboratory experimental models.

The data at hand from the laboratory models were the excitation frequency, excitation amplitude, and tank geometries as the input and images of the surface as the output. It was decided to estimate the natural sloshing frequencies from the data, and to compare them with the linear analytical sloshing frequencies.

In the numerical models, the geometries of the tanks from the laboratory experiments were replicated. Three cylindrical tanks, and two rectangular prismatic tanks were modeled. The natural sloshing mode frequencies were calculated in these models, and the model performances were quantified based on their percentage deviations from the analytic frequencies.

Analytical formulae for the free sloshing frequencies and mode shapes for cylindrical and rectangular tanks may be found in Equation (8.2) and Equation (9.10).

The following section provides a preliminary analysis on the design code, and it can be seen that a similar modal analysis approach is used to incorporate sloshing into design.

9.2. Analysis on the Design Code

In the industry, most welded Oil Storage tanks are designed due to the code "API 650 Welded Steel Tanks for Oil Storage". The appendix section associated with the seismic design was analyzed to see how sloshing has been incorporated into the design.

It was seen that the fluid is perceived as a mass that is divided to an impulsive and a convective portion. The impulsive mass tends to be stationary where the convective mass is considered free to move and slosh. The ratio is determined from the tank diameter per tank height ratio $\frac{D}{H}$. For broad tanks, more liquid is convective than impulsive, and for slender tanks, more liquid is impulsive than convective. A representative image can be found in Figure 8.1.. Intuitively this approach is sensible, as for slender tanks; more liquid may be constrained to move with the tank walls. The formulae for the weight ratios are:

$$\frac{W_i}{W_p} = \frac{\tanh(0.866\frac{D}{H})}{0.866\frac{D}{H}}, \text{ for } \frac{D}{H} \geq 1.333 \tag{9.1}$$

$$\frac{W_i}{W_p} = \left[1.0 - 0.218\frac{D}{H}\right], \text{ for } \frac{D}{H} < 1.333 \tag{9.2}$$

where, W_i is the impulsive weight and W_p is the total weight.

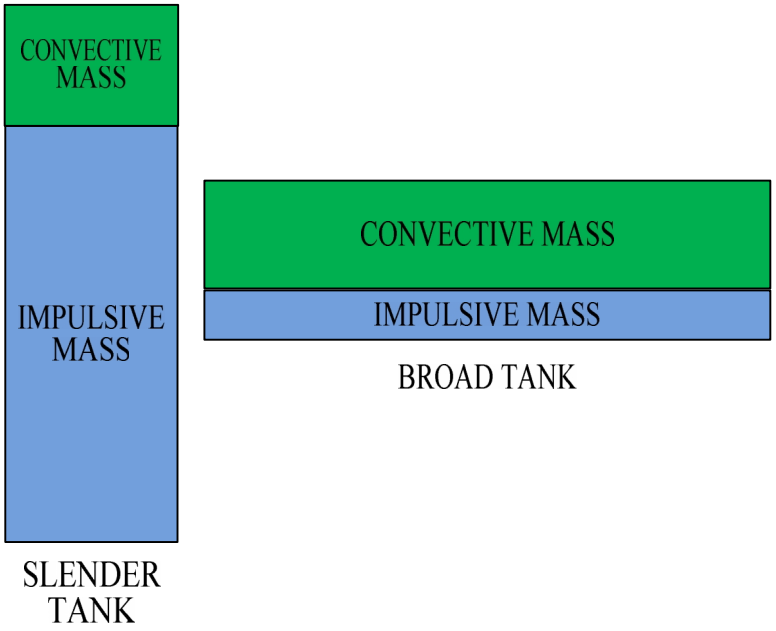

Figure 9.1 Graphical Representation of impulsive versus convective masses.

The natural period for impulsive portion and the natural period for the first sloshing mode for the convective period are calculated in the design code from closed form formulae:

$$T_i = \left(\frac{1}{\sqrt{2000}}\right)\left(\frac{C_i H}{\sqrt{\frac{t_u}{D}}}\right)\left(\frac{\sqrt{\rho}}{\sqrt{E}}\right) \tag{9.3}$$

$$T_c = 1.8 K_s \sqrt{D} \tag{9.4}$$

$$K_s = \frac{0.578}{\sqrt{\tanh\left(\frac{3.68H}{D}\right)}} \tag{9.5}$$

where T_i is the natural period of vibration for impulsive mass, T_c is the natural period of convective (sloshing) mass, H is the maximum design product level, D is the

nominal tank diameter, E is the elastic modulus of tank material, and C_i is a coefficient depending on H/D and is used for determining the impulsive period. The curve to determine C_i is provided in the design code.

In API 650 the next steps in seismic design are to calculate the spectral accelerations based on these periods, and then to combine the spectral accelerations with the effective weights to amplify the design load and overturning moments.

A closed form formula is provided for the design sloshing wave height as:

$$\begin{aligned} \delta_s &= 0.5DA_f \\ A_f &= f(T_C, S_0, geom) \end{aligned} \tag{9.6}$$

where the coefficient A_f is a function of the natural period of vibration for convective mass T_c, peak ground acceleration for maximum considered earthquake S_0, and tank geometry. The estimated sloshing wave height is used to determine the freeboard height for the tank.

It is interesting to see that in the design manual, a dynamic analysis is not required. The only design parameter based on seismically induced sloshing is the natural period of the first mode, and that is calculated from a closed form approximation formula. The effect of the higher modes is not taken into consideration. The sloshing wave height is also a vast approximation, and is a function of T_c.

The approach in API 650 suggests that, analysis of the fluid behavior at higher sloshing modes will be of practical importance. Tanks under seismic excitations may involve complicated coupled high mode resonant sloshing behavior, which may result in the occurrence of wave heights and pressures that are underrepresented in the design. And if the criticality of the higher modes is observed, more sophisticated measures may be taken to incorporate sloshing into the design code.

The following sections show that the models created in this thesis are capable of analyzing higher mode sloshing phenomenon, and these models may be utilized for investigations that may eventually lead to improvements on the design code.

9.3. Methodology for the Tests

9.3.1. Virtual Mass Models

In the Virtual Mass models, eigenvalue analyses are performed to find the fluid structure interaction modes. Corresponding natural mode frequencies are extracted as a result of this analysis. Details of the model can be found on Chapter 6.

Nastran solution sequence 103 was used to perform the eigenvalue analyses. To isolate the fluid from the coupled fluid-structure system, the physical properties of the tank were adjusted to make it rigid. First 30 modes were outputted in the increasing order of their frequencies. Each of these mode shapes were visually analyzed to determine which analytical modes were being represented.

In Chapter 6, it was noted that Nastran was a structures solver and isolating the fluid involved vast approximations. It was seen that most of the parameters in the model formation had an effect on the results. A sensitivity analysis was performed on these effects, which can be found in Table 9.1.

Table 9.1. Sensitivity analysis on Virtual Mass model parameters.

Action	Effect on Frequencies
Finer Surface Mesh	Increase
Finer Bottom Mesh	Increase
Finer Tank Mesh	Negligible Increase
Fluid R approach Tank R	Decrease
Increase Height of the Tank	Negligible Increase
Increase ZFS	Increase
Increase Fluid Density	Decrease (very sensitive)
Increase Tank E	No Effect

Numerical modeling parameters such as fineness of the mesh have interesting effects on the results. But the runs were taken after determining the convergence for these parameters. Figure 9.2. and Figure 9.3. show the effects of changing VMASS special parameters like the phantom surface radius and ZFS level discussed in Chapter 6.

The mesh fineness was selected to make the computation last for a reasonable decent computation time. The other virtual mass parameters were selected to avoid singularities.

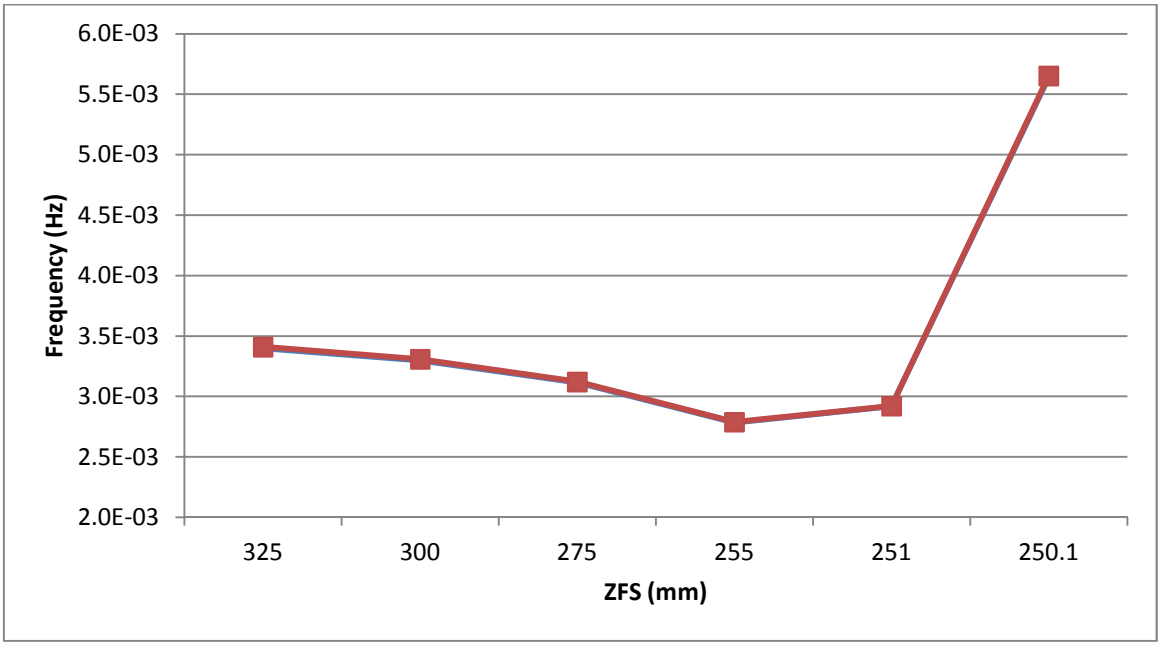

Figure 9.2. Effect of changing ZFS on a sample cylindrical tank of phantom surface level at 250 mm.

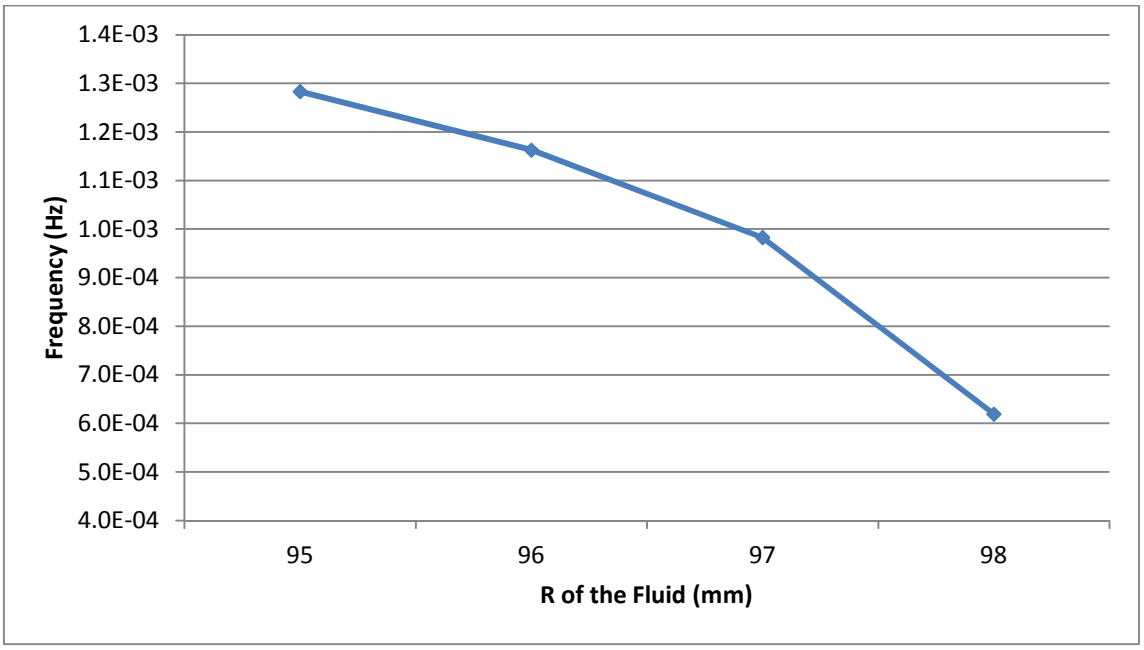

Figure 9.3. Effect of changing ZFS on a sample cylindrical tank of phantom surface level at 250 mm.

9.3.2. RBFCM Models

In the 3D RBFCM models, free sloshing analyses were performed. A mode shape was given as initial surface position to the model, and no other external effects were provided. The data that was recorded were the surface positions vs. time. The natural mode frequencies were obtained by analyzing this data. By running the analysis over long periods of time, the stability of the models were also observed.

The mode shape functions that were used to form the initial conditions are provided in Equation (9.8) for cylindrical basin and Equation (9.12) for rectangular basin. To eliminate the nonlinear effects, peak amplitudes of $\eta = 0.001h$ were chosen for the initial standing waves.

9.3.3. Lab Models

The experimental set up and the procedures for data analysis were as explained in Chapter 7. On important thing to take into consideration was that a particular mode shape could be observed in an interval of frequencies and not in a single excitation frequency. And in the higher modes, these intervals got narrower and overlapped. While processing the data, the interval was recorded, and the frequencies that were closer to the analytical solutions were used in the analyses.

9.4. Cylindrical tanks

Expressions for the sloshing mode shapes and the frequencies are derived by using the potential flow formulation with linearized free surface boundary conditions. An overview is presented in Chapter 2. In Ibrahim (2005) the mode shape and the mode frequency for the cylindrical container is derived using cylindrical coordinates for the boundary conditions and the governing equation, and using the separation of variables technique. Mode shape is given as:

$$\Psi_{n,m}(r,\theta,z) = J_m(\alpha_n^{(m)} r / a)\{A_m \cos(m\theta) + B_m \sin(m\theta)\}\cosh(\alpha_n^{(m)} z / a) \qquad (9.7)$$

where J denotes the Bessel function, and $\alpha_n^{(m)}$ is the n 'th positive root of $J_m' = 0$.

Equation (9.7) is the solution for the surface profile. If $z = 0$ and sinusoidal terms are combined, the resultant equation is:

$$S_{n,m}(r,\theta) = J_m(\alpha_n^{(m)} r / a)\{C_m \cos(m\theta)\} \qquad (9.8)$$

where m and n correspond to the number of nodal diameters and the nodal circles for a given sloshing mode. Equation (9.8) outputs the amplitude S of the surface for given radial coordinates. In the results, the mode shapes are described in the format (m,n).

In any phenomena that involves circular cross sections, the nodal diameters and circles can be used to designate the mode shapes. For example, Waller (1937) analyzed normal vibrating modes of free circular plates, by exciting the metallic circular plates with solid carbon dioxide, and visualizing the nodal circles by sprinkling sand on the surfaces. The corresponding modes are photographed:

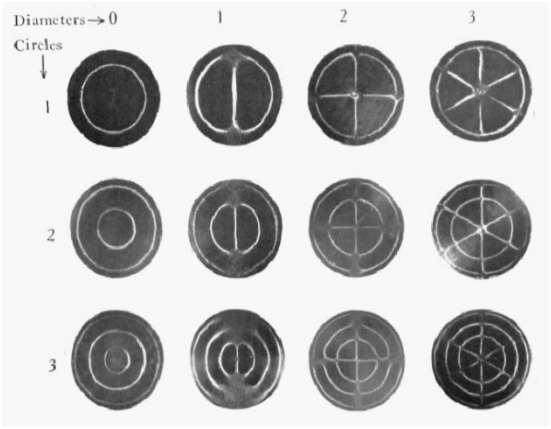

Figure 9.4 Circular Mode Shapes, from (Waller, 1938).

For ease of visualization, the mode shapes are plotted in Matlab:

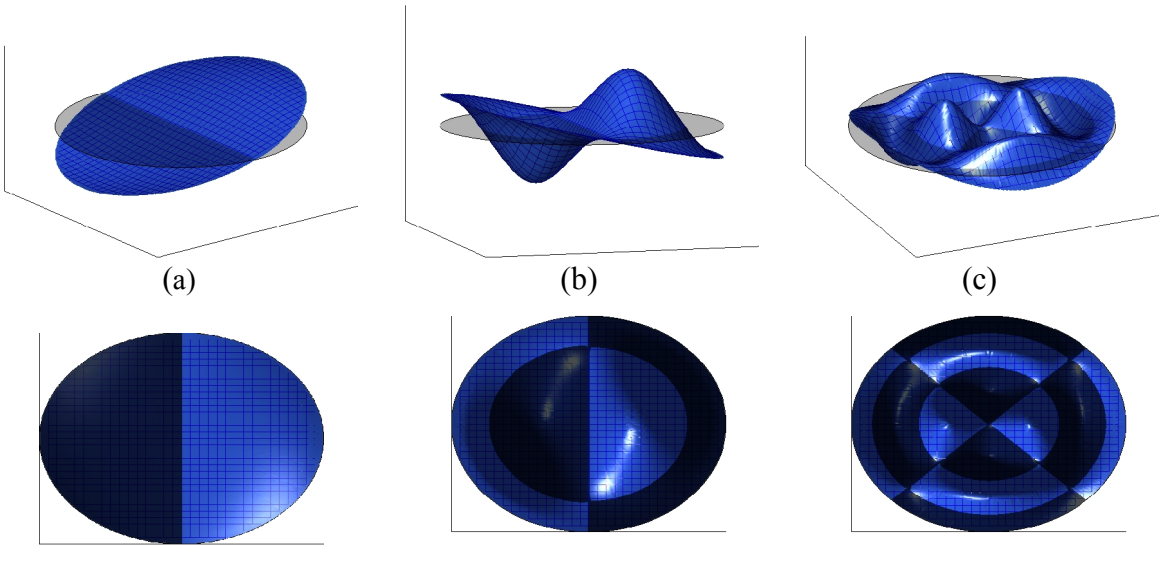

Figure 9.5. Sample mode shapes plotted in Matlab with perspective and top views: (a) and (d): mode (1,1), (b) and (e): mode (1,2), (c) and (f): mode (2,3).

In Ibrahim (2005), the natural mode frequency for a cylindrical tank is given as;

$$\omega_{n,m}{}^2 = \frac{g\alpha_n^{(m)}}{a}\tanh(\alpha_n^{(m)}h/a) \tag{9.9}$$

It should be noted that for $n=1$ and $m=0$, $\alpha_n^{(m)}=0$, and hence, $\omega_{n,m}=0$. Therefore this mode is not computed in the models.

9.4.1. Numerical Model Calibrations

9.4.1.1.Virtual Mass. The tanks analyzed in Nastran had $E=207000\ \mathrm{MPa}$, density of $d=0.00783\ \mathrm{kg/cm^3}$, and fluid density of $\rho=0.001\ \mathrm{kg/cm^3}$. All the CELAS spring constants were thus calculated. The consistent units in Nastran were specified in the program manuals.

Surface mesh was taken with 30×30 elements according to the butterfly mesh method. The surface the diameter was taken as 90% of the tank diameter. This way, the gap required for numerical stability discussed at Chapter 6 could be maintained. Tank height of $h=30$ cm was taken, tank walls were meshed with element sizes equal to the outer most surface mesh elements, and tank bottom was meshed with 30×30 elements.

9.4.1.2.RBFCM. The methodology for creating the nodal layout was explained in Chapter 6. The number of rings and number of elements in each ring could be set in the nodal layout of the RBFCM models. The nodal layout constituting 6 rings was enough to catch the modal behaviors in most of the cases. For the exceptional case of mode (1,4), one extra ring was added for stability and accuracy.

It can be said that for mode shapes of high nodal diameter values, RBFCM nodal layout of higher number of nodes per ring performed better. And for modes of higher modal circles, RBFCM nodal layout of higher number ring performed better. One

technique to reduce the number of nodes might be to first determine the probable peak and zero locations of the free surface; and then placing nodes at those critical points.

The shape parameters used in the three tanks were optimized by hand. Some sample runs with different shape parameters were performed, and the c value that gave the least errors for energy preservation was selected. It can be said that for these particular test cases, the optimum shape parameter c could be found in a range between $0.5d_{\min}$ to $1.5d_{\min}$.

9.4.2. Results

Table 9.2, Table 9.3, and Table 9.4 show the calculated analytical mode frequencies for the three cylindrical tanks. The mode shapes observed on the laboratory experiments are shaded. Figures Figure 8.9a through Figure 8.9f show some clearly seen mode shapes, the initial conditions for the RBFCM models, and the outputs from the VMASS models.

Table 9.2. Analytical mode frequencies for cylindrical tank with radius of 5 cm.

m	n = 1	n = 2	n = 3	n = 4	n = 5	n=6	n=7
0	0	4.36381	5.90475	7.11057	8.13733	9.04742	9.87355
1	3.02495	5.14745	6.51336	7.62736	8.59471	9.46222	10.2559
2	3.89602	5.77306	7.03891	8.09037	9.01354	9.84761	10.6148
3	4.56936	6.31143	7.50913	8.51404	9.40248	10.2093	10.9542
4	5.14074	6.79203	7.93893	8.90722	9.76732	10.5512	11.2772
5	5.64662	7.2306	8.33748	9.27585	10.1122	10.8765	11.586
6	6.10572	7.63677	8.71091	9.62416	10.4401	11.1875	11.8824

Table 9.3. Analytical mode frequencies for cylindrical tank with radius of 7.5 cm.

m	n = 1	n = 2	n = 3	n = 4	n = 5	n=6	n=7
0	0	3.56304	4.82121	5.80575	6.6441	7.38719	8.06172
1	2.46985	4.20287	5.31813	6.22771	7.01756	7.72587	8.37388
2	3.18109	4.71368	5.74725	6.60576	7.35953	8.04054	8.66692
3	3.73087	5.15326	6.13118	6.95168	7.67709	8.33583	8.9441
4	4.1974	5.54567	6.48211	7.27271	7.97498	8.61505	9.20783
5	4.61045	5.90376	6.80752	7.5737	8.25656	8.88066	9.45995
6	4.9853	6.2354	7.11242	7.85809	8.52433	9.13452	9.70192

Table 9.4. Analytical mode frequencies for cylindrical tank with radius of 10 cm.

m	n = 1	n = 2	n = 3	n = 4	n = 5	n=6	n=7
0	0	3.08568	4.17529	5.02793	5.75396	6.39749	6.98165
1	2.13875	3.6398	4.60564	5.39335	6.07738	6.6908	7.25199
2	2.7549	4.08217	4.97726	5.72076	6.37354	6.96331	7.50578
3	3.23103	4.46286	5.30976	6.02033	6.64856	7.21904	7.74582
4	3.63505	4.80269	5.61367	6.29835	6.90654	7.46086	7.97421
5	3.99277	5.11281	5.89549	6.55902	7.15039	7.69088	8.19256
6	4.3174	5.40002	6.15954	6.80531	7.38229	7.91073	8.40211

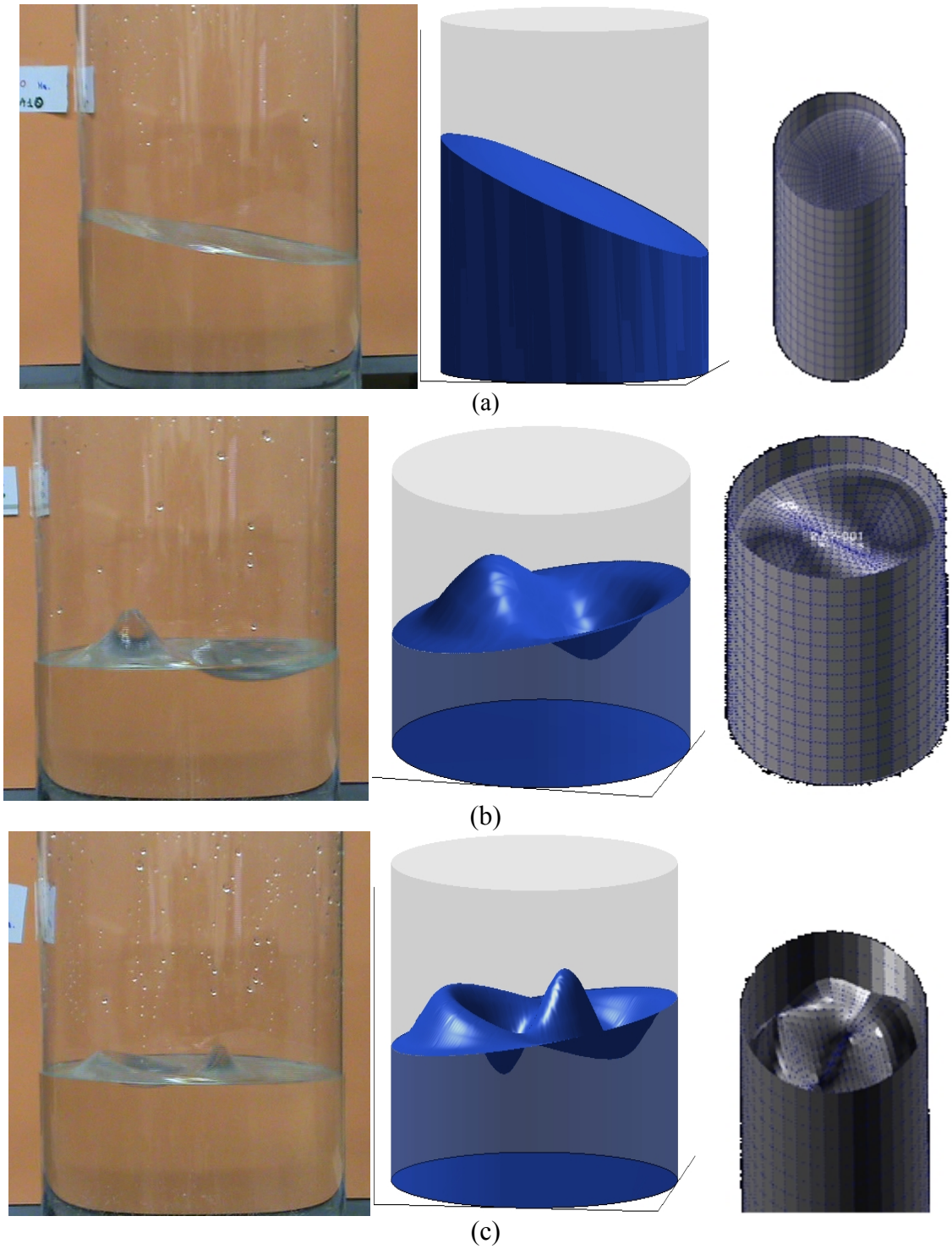

Figure 9.6 Comparisons of mode shapes from Laboratory experiments(left), RBFCM models(middle) and Virtual Mass Models(right). (a): (1,1), (b): (1,2), (c): (1,3).

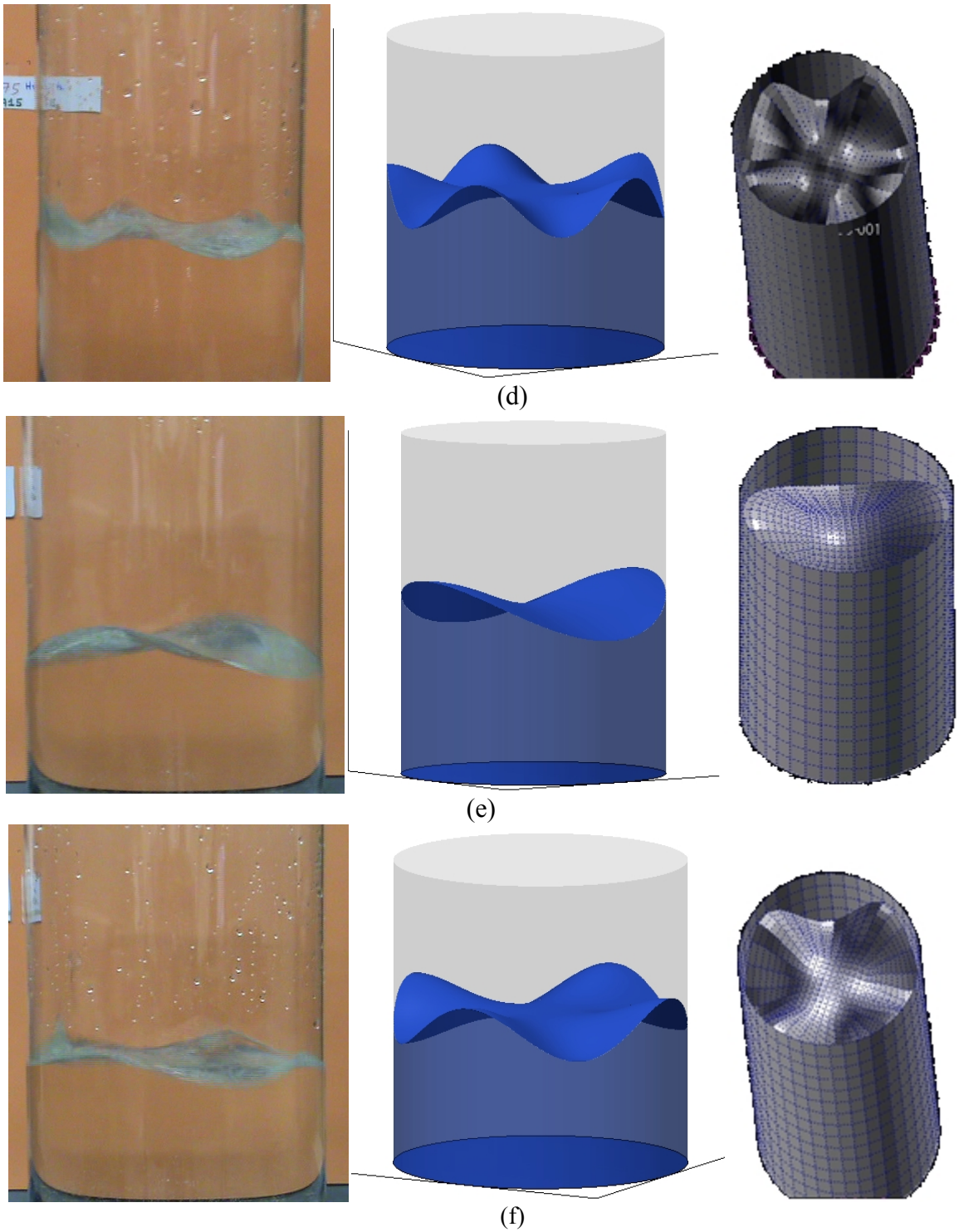

(d)

(e)

(f)

Figure 9.6. Comparisons of mode shapes from Laboratory experiments(left), RBFCM models(middle) and Virtual Mass Models(right). (a): (1,1), (b): (1,2), (c): (1,3), (d): (5,1), (e): (2,1), (f): (4,1) (cont.).

Table 9.5. Model comparisons with percentage absolute relative error of the residuals with respect to the linear analytical theory (a) $r = 0.05\text{m}$ m (b) $r = 0.075\text{m}$ (c). $r = 0.10\text{m}$.

MODE		%RELATIVE ERROR			MODE		%RELATIVE ERROR			MODE		%RELATIVE ERROR		
m	n	VMASS	RBF	EXP	m	n	VMASS	RBF	EXP	m	n	VMASS	RBF	EXP
1	1	3.0	0.2	24.0	1	1	9.7	0.3	15.8	1	1	20.1	1.1	6.5
2	1	2.7	0.4		2	1	7.9	0.7		2	1	16.5	0.8	0.2
0	2	1.8	0.6		0	2	3.9	0.1		0	2	8.4	0.0	
3	1	4.9	0.6		3	1	9.1	0.5		3	1	16.1	0.4	17.6
4	1	7.3	0.6		4	1	10.7	0.1		4	1	16.9	0.0	0.7
1	2	3.3	0.1	3.25	1	2	4.3	0.3	6.0	1	2	8.4	0.5	4.4
5	1	4.2	0.2		5	1	4.9	0.9	3.0	5	1	8.6	0.9	
2	2	5.2	0.4		2	2	5.5	1.3		2	2	8.8	1.2	5.4
0	3	7.0	1.0		0	3	5.7	2.0		0	3	8.9	2.2	
3	2	7.5	1.4		3	2	7.1	2.5		3	2	10.2	2.5	
1	3	6.5	0.5		1	3	6.5	3.4	2.5	1	3	9.1	0.1	22.5
6	1	14.7	1.5		6	1	16.6	2.5	15.8	6	1	21.2	1.2	
4	2	10.6	0.3		4	2	9.3	1.8		4	2	11.9	1.2	
2	3	9.6	1.7		2	3	8.1	1.1		2	3	10.2	2.3	
1	4	4.3	0.5		1	4	5.5	0.5		1	4	10.1	3.0	7.2
		(a)					(b)					(c)		

Table 9.5 clearly summarizes the deviations of the laboratory experimental and numerical models from the linear analytical theory. The deviations are calculated from the difference from the models with the analytical result, normalized with the analytical value. The absolute values are tabulated.

It can be concluded that Virtual Mass model detects mode shapes at about 10% accuracy and RBF models at 3% accuracy levels. The c values for the RBFCM models were $0.6\,d_{\min}$, $0.9\,d_{\min}$ and $1.5\,d_{\min}$. For modes beyond (3,2), c values were modified to 0.5 $d_{\min}$, $0.5\,d_{\min}$ and $0.8\,d_{\min}$. The last mode was computed with adding one extra ring to the nodal layout.

9.5. Rectangular tanks:

The first studies for determining the mode shapes and frequencies for sloshing in rectangular basins was carried out by Lamb (1934). Abramson (1966) documented his findings and performed some experiments to indentify the mode shapes. The natural mode frequencies are defined in Abramson (1966) as:

$$\begin{aligned} &\sigma_{i,j}^2 / g = k_{i,j} \tanh(k_{i,j} h) \\ &k_{i,j} = \pi \sqrt{(i / L_1)^2 + (j / L_2)^2}, i + j \neq 0 \end{aligned} \tag{9.10}$$

where σ is the frequency of mode (i, j), L_1 and L_2 are the length and width of the tank and h is the height of the fluid.

In Faltinsen and Timokha (2009), the free surface profiles of the mode shapes for rectangular prismatic containers are derived by solving linearized sloshing problem by separating the spatial variables. Solutions are given in the form of Stokes freestanding waves:

$$\begin{aligned} &f_i^{(1)}(x) = \cos[i\pi(x + \frac{1}{2} L_1) / L_1] \\ &f_j^{(2)}(y) = \cos[j\pi(y + \frac{1}{2} L_2) / L_2], \quad i, j \geq 0 \end{aligned} \tag{9.11}$$

And the mode shape is given as:

$$f_{i,j}(x, y) = f_i^{(1)}(x) f_j^{(2)}(y) \tag{9.12}$$

Equation (9.12) provides basic mode shapes due to planar nodal lines.

Other than planar resonant standing waves, some more complicated mode shapes may be observed; especially when the basin is square. Some solutions may produce square-

like resonant standing wave coupling with in-phase oscillations of two identical low modes (Faltinsen *et al.,* 2003). Wave profiles will involve pairs of Stokes waves:

$$S_1^i(x,y) = f_i^{(1)}(x) - f_i^{(2)}(y)$$
$$S_2^i(x,y) = f_i^{(1)}(x) + f_i^{(2)}(y) \tag{9.13}$$

These mixed modes are denoted as ‘diagonal’ or ‘square’ modes by (Faltinsen *et al.,* 2003) and an in-depth analysis may be found there. Figure 9.7 shows the difference between the diagonal and planar modes. The observation in the experiments was that the higher diagonal modes in the square basin resembled the modes in circular basin. For example, Figure 9.7d can be perceived as a nodal circle. The subjects require more attention and research.

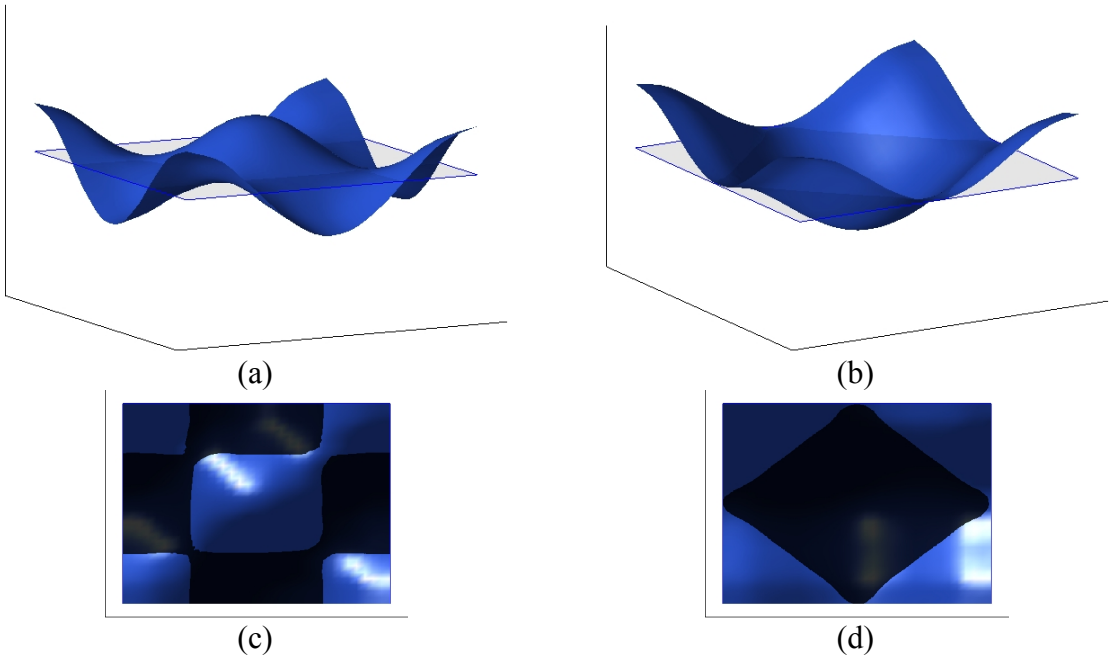

Figure 9.7. Demonstration of planar vs. diagonal (2,2) mode shapes in square basin; (a), (c): planar, (b),(d) diagonal.

Another surface profile defined in Faltinsen *et al.,* (2003) is the swirling wave patterns moving along the tank walls in clockwise or counterclockwise direction. They are identified with the mode function:

$$f_{i,j}(x,y,t) = f_1^{(1)}(x)\cos\sigma_{1,0}t \pm f_1^{(2)}(y)\sin\sigma_{0,1}t \tag{9.14}$$

It should be noted that a fixed excitation frequency may trigger one of the three types of mode shapes (planar, swirling or square-like) depending on the excitation amplitude/breadth ratio or depth/breadth ratio (Faltinsen *et al.,* 2003). These factors were not taken into consideration during the experiments. Therefore it has been extremely difficult to visually identify higher mode shapes, leaving room for a lot of human error.

In the laboratory experiments, two tanks were tested, one with rectangular basin and the other with square basin. The rectangular tank was excited on its two principal axes and the square tank was excited on the principal axis and on the diagonal axis.

In the rectangular tank, because of the low width / length ratio, some diagonal modes have also been excited, but could not be identified. In the square tank, diagonal shaking excited both the planar and diagonal modes.

The studies in this thesis aim at demonstrating the effectiveness of the RBFCM models, which has been successfully achieved. However, there were difficulties in the analysis on swirling and square-like sloshing patterns, their identifications and calculating their frequencies. Such a study should be a topic for a future research project that is focused solely on sloshing in square basins.

9.5.1. Numerical Model Calibrations:

9.5.1.1.Virtual Mass. The Virtual Mass models for the rectangular tanks were created in a similar manner with the cylindrical tanks. The tank geometries were taken the same as the laboratory tanks, and the physical properties of the rectangular tanks for the VMASS models were taken to be the same with the physical properties of the cylindrical tanks. The surface was meshed with 20×30 elements for the rectangular tank and 20×20 for the square tank.

9.5.1.2.RBFCM. In the RBF models for rectangular tanks, the initial free surface profiles were specified using Equation (9.12). The nodes were distributed uniformly and the optimum shape parameters were found in the range $1d_{\min}$ to $1.5d_{\min}$

9.5.2. Results

The mode shapes that were observed in the experiments were shaded and tabulated in Table 9.6 and Table 9.7. For the square basin case, the table is symmetrical to the diagonal axis, and only one half of the table is colored. The tables suggest that mode shapes for most of the lower mode number were observed during the experiments.

The computed errors are given in Table 9.8., and show the percentage deviation of the models from the analytical solution by computing the residuals and normalizing them with the analytical values. The table shows that there is a gradual increase in the errors for computing the mode frequencies for the higher modes. Also, all the models behaved poorly in the case with the square basin, and this is thought to originate from the complicated surface behavior in these containers. Some further research in mesh refinement and model optimizations may be required in a further research project to more accurately solve the square basin sloshing problem.

Table 9.6 Analytical mode frequencies for rectangular prismatic tank with $l = 15cm$, and $w = 10cm$

j	i=0	i=1	i=2	i=3	i=4	i=5	i=6
0	0.00	2.79	3.95	4.84	5.59	6.25	6.84
1	2.28	3.06	4.06	4.90	5.63	6.28	6.86
2	3.23	3.61	4.33	5.06	5.74	6.36	6.93
3	3.95	4.18	4.70	5.31	5.91	6.48	7.03
4	4.56	4.72	5.10	5.60	6.13	6.65	7.16
5	5.10	5.21	5.51	5.92	6.38	6.85	7.32
6	5.59	5.67	5.91	6.25	6.65	7.07	7.50

Table 9.7 Analytical mode frequencies for rectangular prismatic tank with $l = w = 15cm$

j	i=0	i=1	i=2	i=3	i=4	i=5	i=6
0	0.00	2.28	3.23	3.95	4.56	5.10	5.59
1	2.28	2.71	3.41	4.06	4.63	5.15	5.63
2	3.23	3.41	3.84	4.33	4.82	5.29	5.74
3	3.95	4.06	4.33	4.70	5.10	5.51	5.91
4	4.56	4.63	4.82	5.10	5.43	5.77	6.13
5	5.10	5.15	5.29	5.51	5.77	6.07	6.38
6	5.59	5.63	5.74	5.91	6.13	6.38	6.65

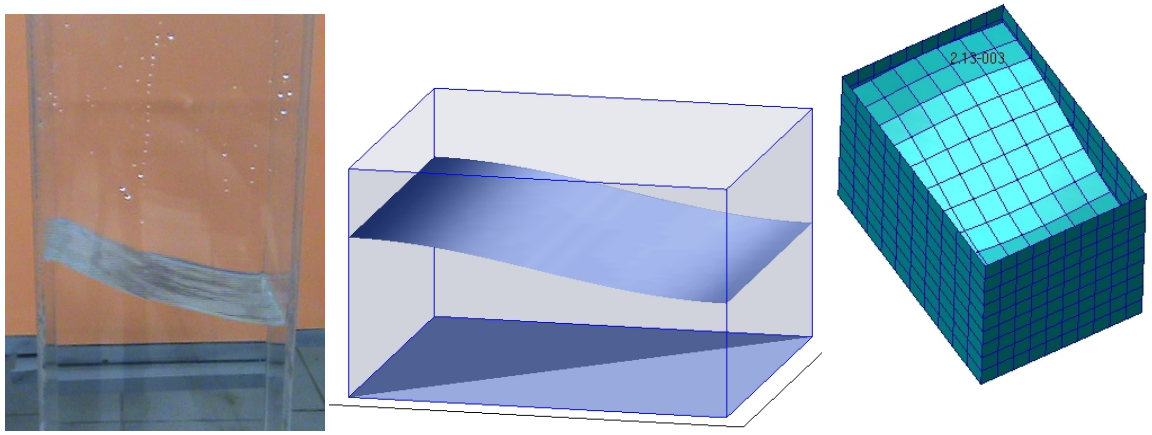

(a)

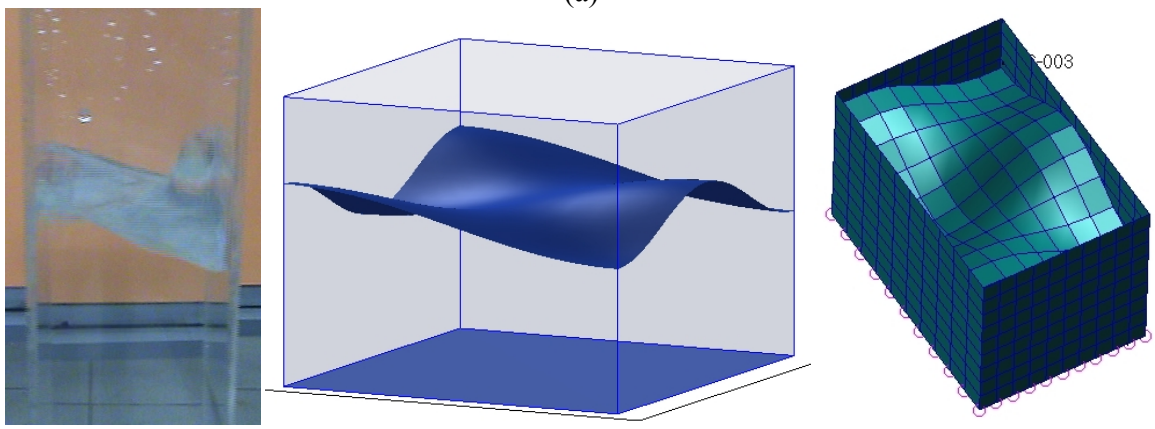

(b)

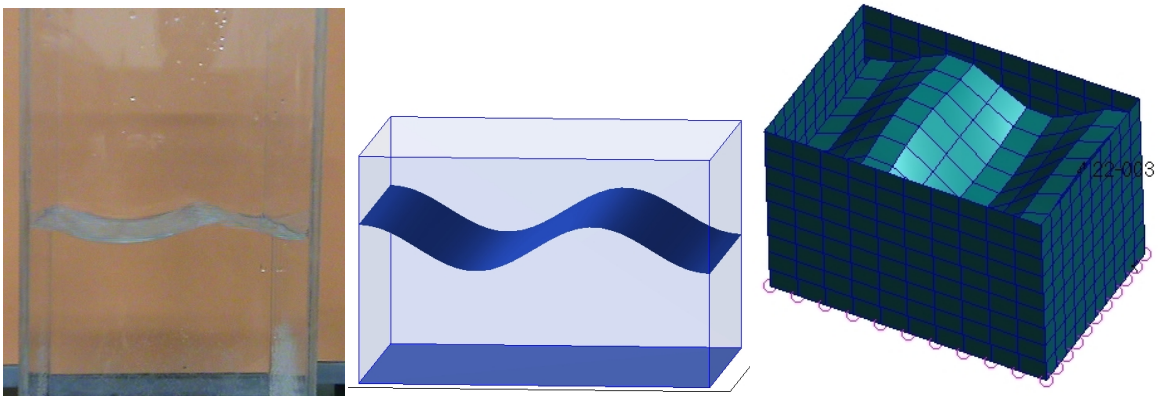

(c)

Figure 9.8. Comparisons of mode shapes from Laboratory experiments(left), with RBFCM(middle) and Virtual Mass models(right) (a): (1,0), (b): (2,1), (c): (0,3)

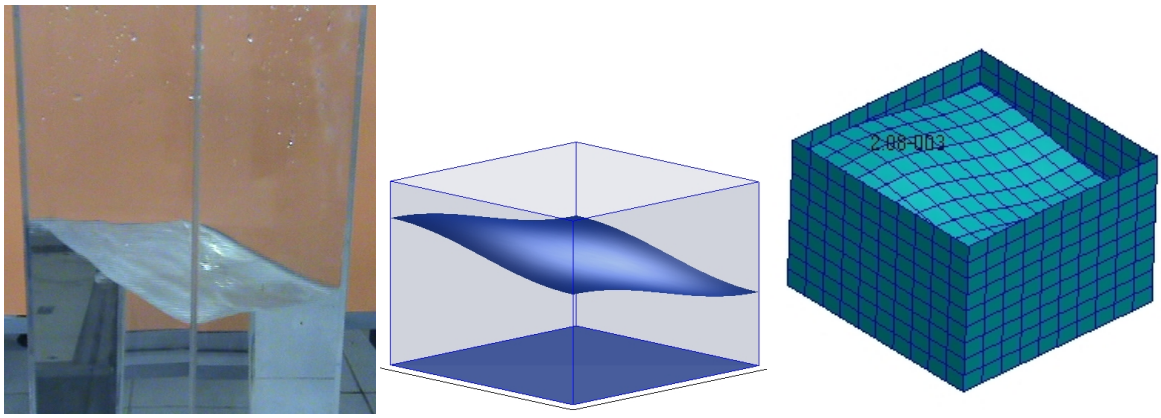

(d)

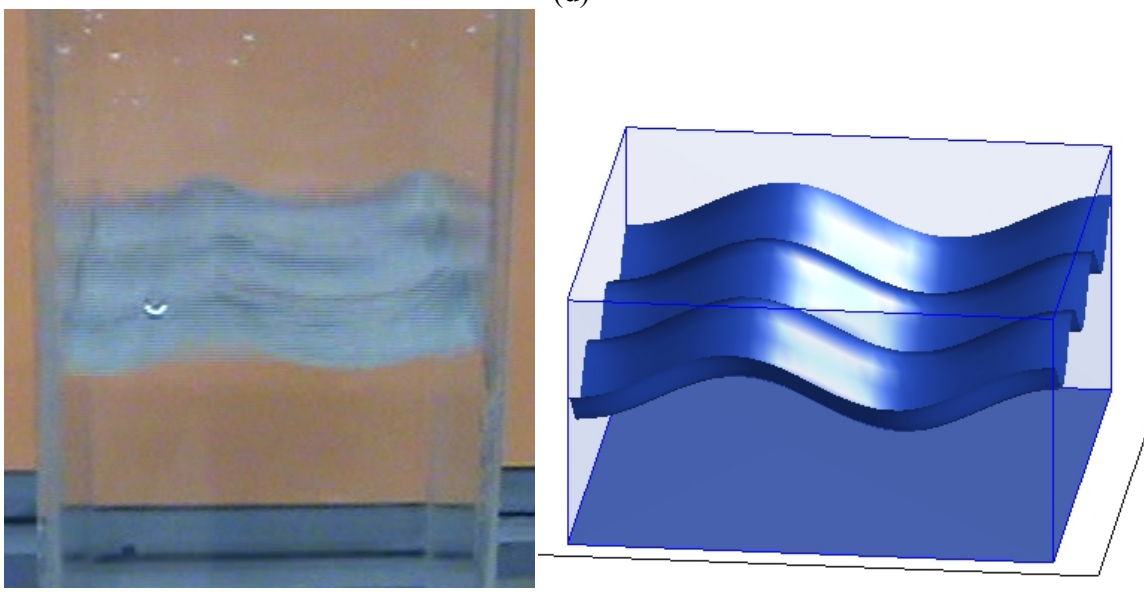

(e)

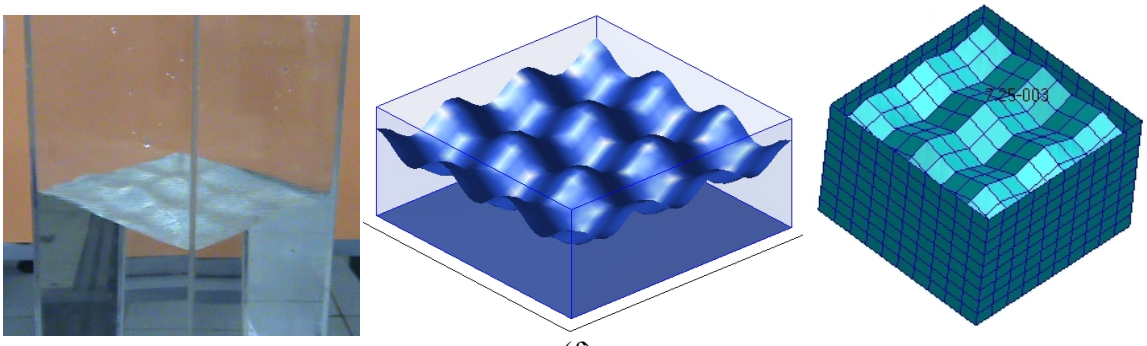

(f)

Figure 9.8. Comparisons of mode shapes from Laboratory experiments(left), with RBFCM models(middle) and Virtual Mass Models(right). (d): (1,1) diagonal, (e): (5,3), (f): (5,0) diagonal (Cont.).

Table 9.8. Model comparisons with percentage absolute relative error with respect to the linear analytical theory (a) $l = 15cm$, and $w = 10cm$ (b) $l = w = 15cm$.

MODE		%RELATIVE ERROR			MODE		%RELATIVE ERROR		
m	n	VMASS	RBF	EXP	m	n	VMASS	RBF	EXP
0	1	26.3	1.8	12.3	1	0	21.2	0.0	9.6
1	0	20.2	0.2	11.2	2	0	17.1	0.9	19.7
1	2	20.3	0.5	4.8	3	0	20.7	2.0	1.8
0	3	14.9	1.6	3.8	3	1	24.3	2.0	2.3
2	1	17.5	1.7	28.8	4	0	29.3	3.8	38.6
1	3	18.6	1.5	0.3	5	0	44.3	6.0	4.1
2	3	18.8	2.1	7.2	4	3	44.3	5.8	9.8
3	2	17.8	2.4	4.2	5	1	47.7	6.2	12.8
2	4	19.2	3.0	1.7					
0	5	21.5	2.7	7.8					
1	5	20.4	2.7	9.4					
3	3	22.6	2.8	11.8					
2	5	21.6	3.2	1.6					
3	4	22.7	4.4	4.1					
3	5		4.4	0.2					

(a) (b)

9.6. Earthquake Motions

The final numerical test on 3D sloshing performed in this thesis is an engineering application case. A realistic cylindrical tank with diameter 30m and fluid depth 10m is considered. The tank is modeled with both RBFCM and VMASS. For the VMASS model, the surface is meshed with 521 nodes and 500 elements, and in the RBFCM model, 121 nodes are used on the surface. Total number of nodes is 1369 for the RBFCM model and 1963 for the VMASS model. Real time earthquake motion is applied on the tank using the two models. The resultant free surface motion is analyzed to determine the maximum wave height from the analysis.

The earthquake signal used is from the 1999 İzmit Earthquake. Data from the Yarımca station is used. The data is acceleration vs. time data and it was sampled at 200 Hz. The Total length of the signal was 50 seconds.

The maximum sloshing wave amplitude is estimated as 1.86m in the VMASS model and 1.94m in the RBFCM model.

A difference of the model outputs are within 5%, and it can be said that the two analyzes yield similar results.

10.CONCLUSIONS

In the studies a 2D RBFCM model using fully nonlinear boundary conditions, and a 3D RBFCM model with linearized boundary conditions were developed to solve sloshing. The numerical tests performed on the 2D models show that an effective model was developed to solve 2D sloshing problems with low to medium amplitude free surface deformations. For 2D sloshing problems involving large free surface boundary deformations, the method yielded promising results leaving room for improvement, but demonstrated that it can be a competitor to popular sloshing models in the literature. The main challenge in modeling these problems was the estimation of derivatives near the boundaries, which is known as a global issue faced in all of the popular numerical methods. The problems were tried to be overcome using some experimental techniques like node clustering near the edges and reducing the number of RBF's which are documented in the appendix. This field is still under extensive contemporary research.

In the 3D sloshing analyzes, RBFCM models were supported with Virtual Mass models. They were benchmarked with the linear theory, and were observed to output comparable results for the analysis of a real tank modeling example. This shows that Virtual Mass method can successfully incorporate sloshing into a structures solver.

The models' demonstrated performances in solving the benchmark problems show that they can be used for engineering design purposes. Further fields of study will be to alter the tank shapes by means of changing the depth/breadth ratios of the tanks, adding baffles, or changing the overall geometry of the tanks. Parametric studies by modeling the tanks with these tools will lead to more optimum design considerations. Also, model coupling with structural models to model fluid structure interaction may be considered for future projects.

APPENDIX A: EXPERIMENTED MODELING FEATURES AND COMMENTS FOR HIGH AMPLITUDE CASES

The approach in the RBFCM modeling is to fit an RBF on the problem domain. It is guaranteed that the collocated information is satisfied in this fit. The primal challenge of modeling the high amplitude sloshing problem with this technique is the estimation of the derivatives on the boundaries. And the problem solution is highly dependent on these estimations.

As with all numerical methods, the poor behavior of the RBF's near the boundaries is an issue that has been reported in the literature numerous times. For example, In (Fornberg *et al.,* 2002), the issue is demonstrated by fitting constant equispaced data in 1D, as shown in Figure A.11.

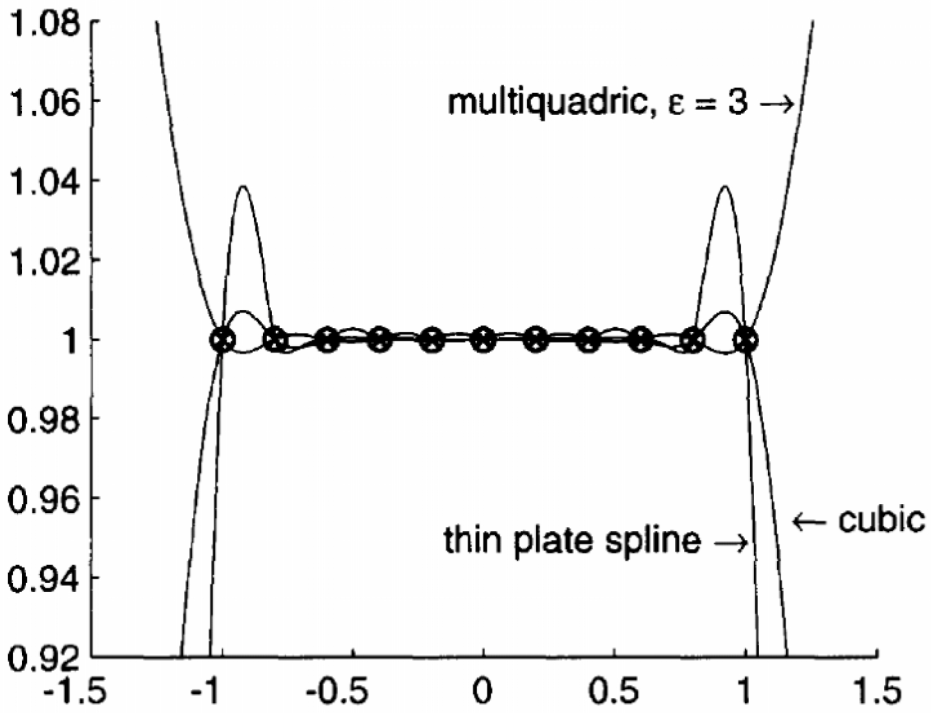

Figure A.1 RBF approximations of constant data over [-1,1] (Fornberg, 2002)

Figure A.1 demonstrates that even though the data is satisfied on the collocation points, the behavior of the RBF greatly affects the solutions close to the boundaries.

The problem is similar to the Runge's Phenomenon, which occurs in the field of polynomial approximation. A popular demonstrative example is to observe equispaced interpolation of the Runge function.

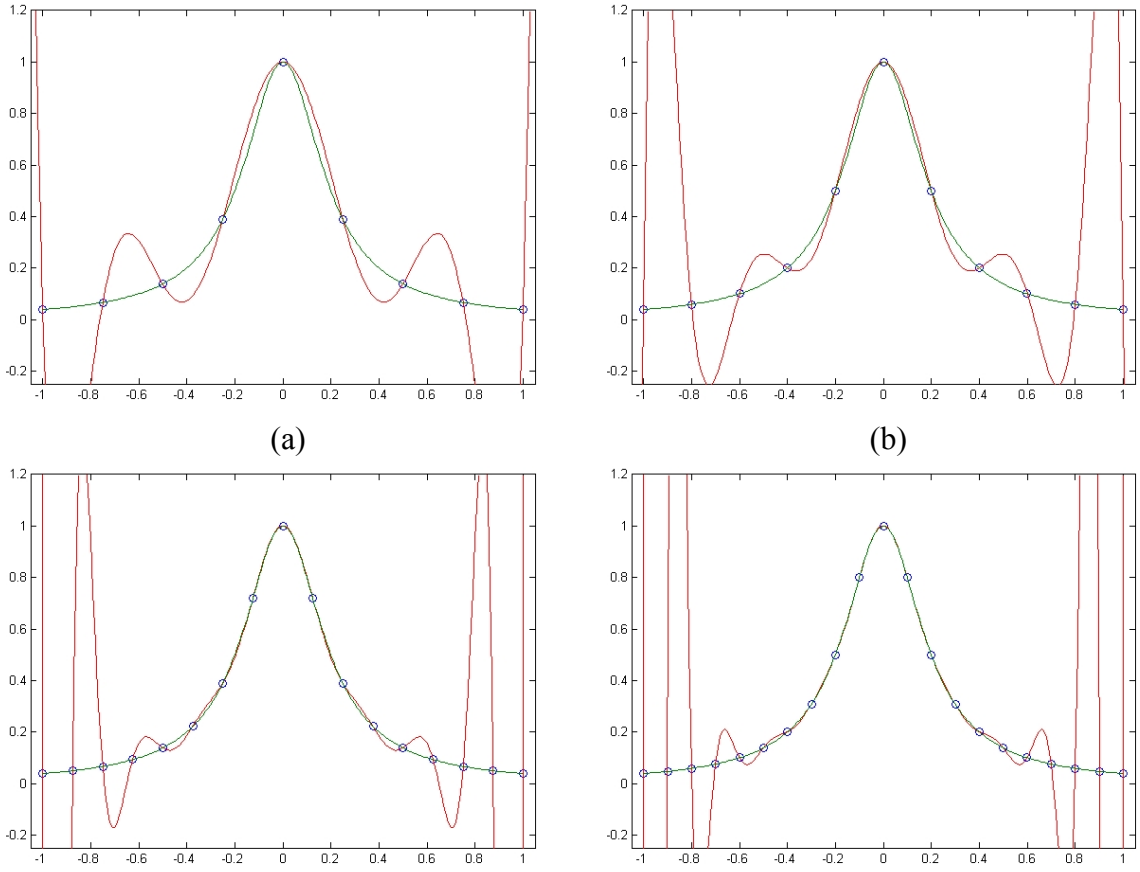

Figure A.2 Demostration of the Runge's Phenomenon by equispaced polynomial interpolation of $y = \frac{1}{1+25x^2}$ over the interval $[-1,1]$, (a) n=9, (b) n=11, (c) n=17, (d) n=21

Over the years many scientists offered techniques to improve behavior of the RBF's near the boundaries. In Fedoseyev *et al.* (2002), PDECB procedure and in Fornberg *et al.* (2002), Not a Knot procedure was offered. In Fornberg and Zuev (2007), RBF behavior on

Runge's Phenomenon was examined using different RBFs, variable shape parameters, and different nodal layouts. Other means to control RP or to improve the accuracy can be listed as,

- Node clustering near the edges, and spatially variable shape parameters (Fornberg and Zuev, 2007)
- Reducing the number of RBF's (Bishop, 1991), and setting the locations and the shape parameters of the rbfs free. Optimizing these parameters by iteration (Wu and Chang, 2011).
- Cardinal preconditioning (Brown 2005)
- Using the fundamental solution of the Laplace equation as the radial basis functions (Wu *et al.*, 2006)
- Enrichment of the RBF interpolant with singularity-capturing terms (Bernal 2008; Bernal *et al.*, 2009)
- Using methods like the level-set method (Vrankar *et al.,* 2010) or the Volume of fluid method for keeping track of the boundary

In the sloshing problem, the free surface boundary is subject to deformations, which may be high amplitude, and irregular for the nonlinear sloshing cases. Issues shown in Figures A-1 and A-2 are observed in 1D problems. When the dimension increases measures to improve accuracy become more complex.

There are many possible techniques that could be combined and used to improve the solutions. However, which combination yields the best results is simply not known a priori. The best combination differs for each case, and most of these techniques are not based on physical parameters. Therefore a brute force methodology is required to try and find the best combination that works.

In the following section, the comments on some of the utilized techniques are provided.

A.1. PDECB

An example of the effect of PDECB on the estimations near the boundary can be observed in Figure A.3a to Figure A.3d. Estimations of the Laplacian inside and outside the computational domain are plotted first without PDECB and then with PDECB.

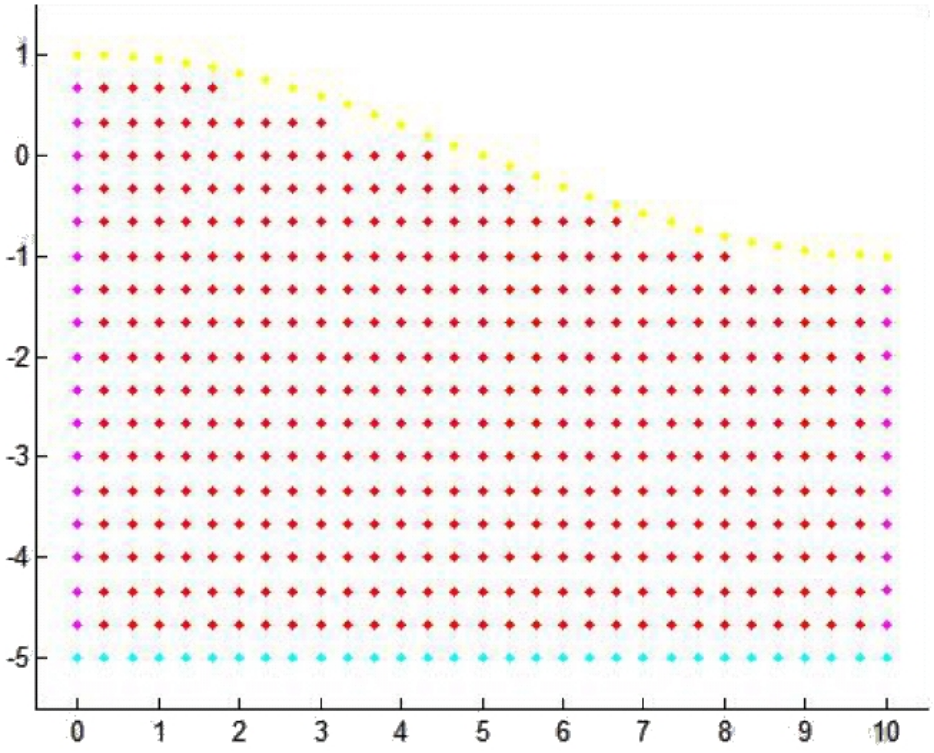

(a)

Figure A.3. Illustrative example of PDECB Procedure's Effect on the Estimation of the Laplacian; (a), (c): Nodal Layout, (b), (d): Laplace Estimation.

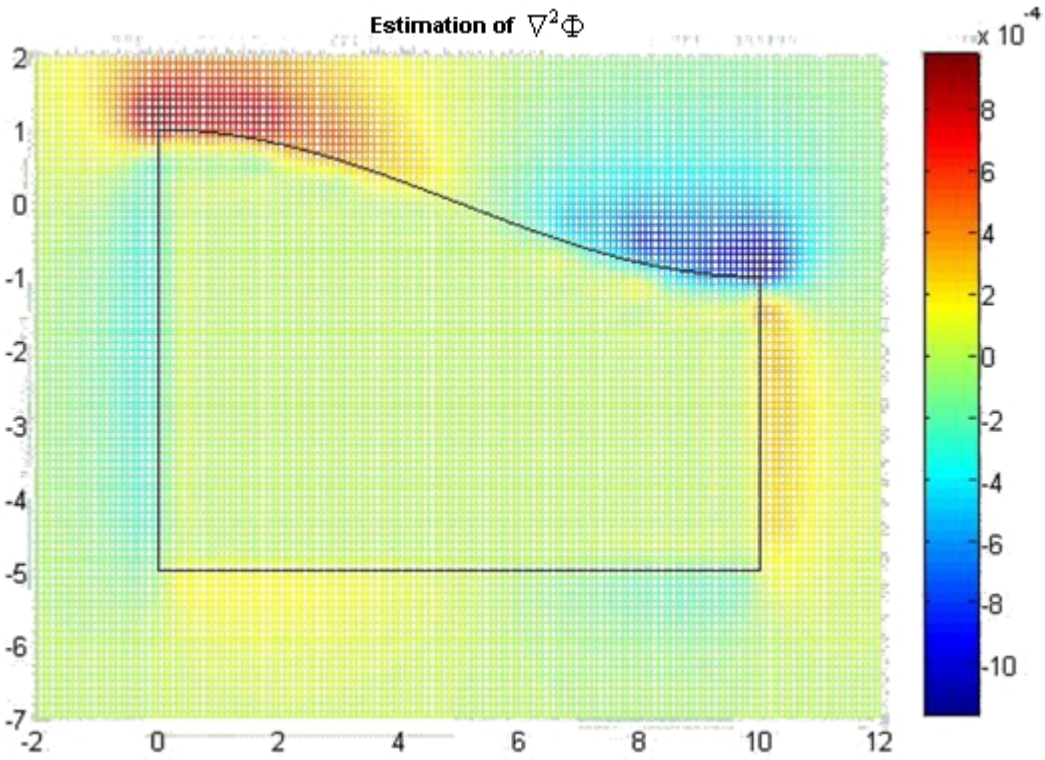

(b)

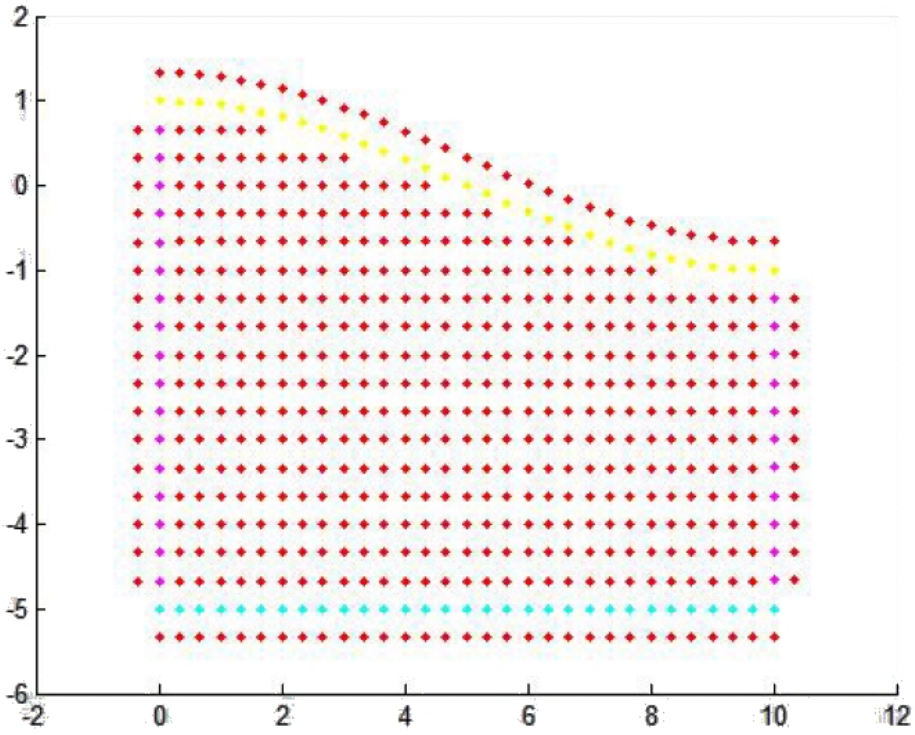

(c)

Figure A.3. Illustrative example of PDECB Procedure's Effect on the Estimation of the Laplacian; (a), (c): Nodal Layout, (b), (d): Laplace Estimation (Cont.).

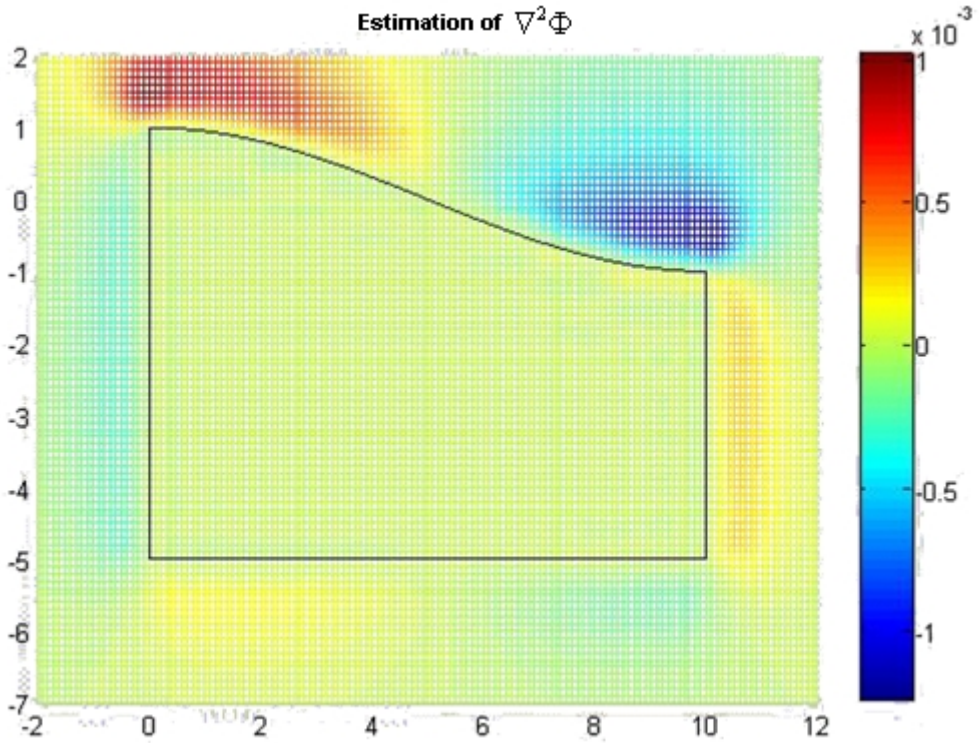

(d)

Figure A.3. Illustrative example of PDECB Procedure's Effect on the Estimation of the Laplacian; (a), (c): Nodal Layout, (b), (d): Laplace Estimation (Cont.).

In the first example it can be seen that extreme values of maxima and minima similar to that in Figure A-1 are present the estimations. In the second figure, these extremities moved away from the boundary, resulting in a more accurate representation of the Laplace equation inside the domain and on the boundaries. Experiments were carried out about the location of the additional RBF centers that were placed outside the domain. It was observed moving these centers farther away also moved the extremities far away from the boundaries, but the extremities got higher in value and had a worse influence on the boundary estimations.

A.2. Mesh Deformation Procedure

Different mesh deformation procedures were examined. The technique preferred was to evenly distribute a fixed number of nodes between the surface node and the ground node lying on the same axis. An example nodal layout on an extreme case is shown in Figure A-4.

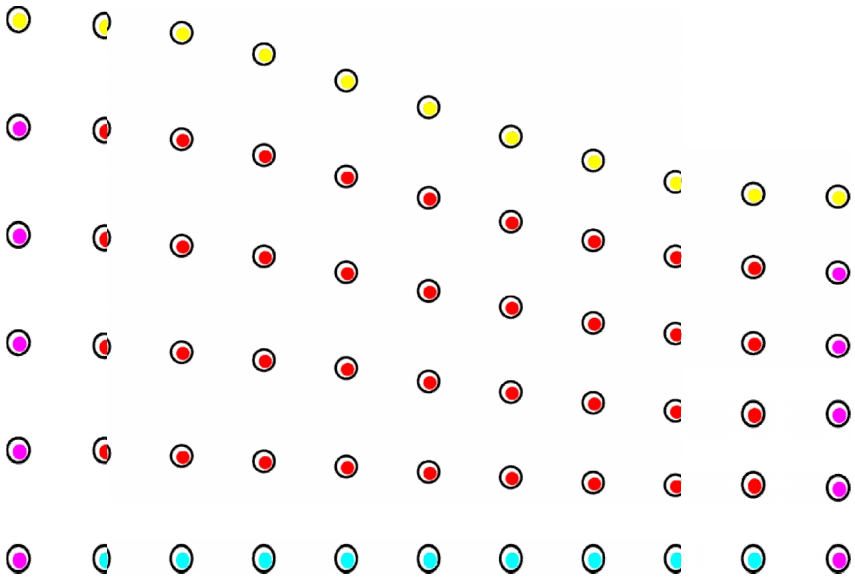

Figure A.4. Sample Nodal Layout Without the PDECB, ○ RBF Centers, • Collocation Centers.

Another technique tried was to maintain a range of minimum internodal distance in the vertical direction, and let the number of nodes between the surface and the bottom boundary vary. This technique maintained a more uniform distribution of the minimum internodal distances. However, the non uniformity in the location of the nodes caused problems especially on the boundary. Even though globally better internodal distances were achieved in this technique, special considerations were required near the boundaries. Therefore this effort was avoided.

During the model tests, it was observed that the most time consuming task in the time marching algorithm was the geometry regeneration phase. A technique that was experimented with was to fix location of some nodes and to free the remaining nodes. This technique was abandoned because it was observed that the previous deformation procedure performed better. But this technique was seen to be effective for increasing the speed of the code.

Supposing there are n number of free nodes m number of fixed nodes. One might decompose the system matrix $[F]$ into:

$$[F]=\begin{bmatrix} C & M_1 \\ M_2 & M_3 \end{bmatrix} \tag{A.1}$$

Where $[C]$ denotes the $m \times m$ matrix that is constant through the time marching phase. It is formed in the beginning due to the internodal relationships of stationary nodes. $[M_1]$and $[M_2]$denote the $n \times m$ and $m \times n$ matrices respectively that are modified due to the relations between the stationary and non-stationary nodes. And the matrix $[M_3]$is the $m \times m$ matrix that is formed due to internodal relationships of non-stationary surface nodes.

It was attempted to use the block matrix inverse algorithms to speed up the inversion process for $[F]$ by using the constant regions. However, for matrices of sizes above 100×100, there were instability issues, and future research on speeding up this process might be required for optimizing the model performance.

A.3. Separation of RBF and Collocation Centers

In the Section 4.1, it was stated that the location of RBF and Collocation centers did not need to be the same points. An example application of this flexibility was explained in the PDECB procedure.

It was decided to fully separate the RBF centers from the collocation centers and examine the model performances.

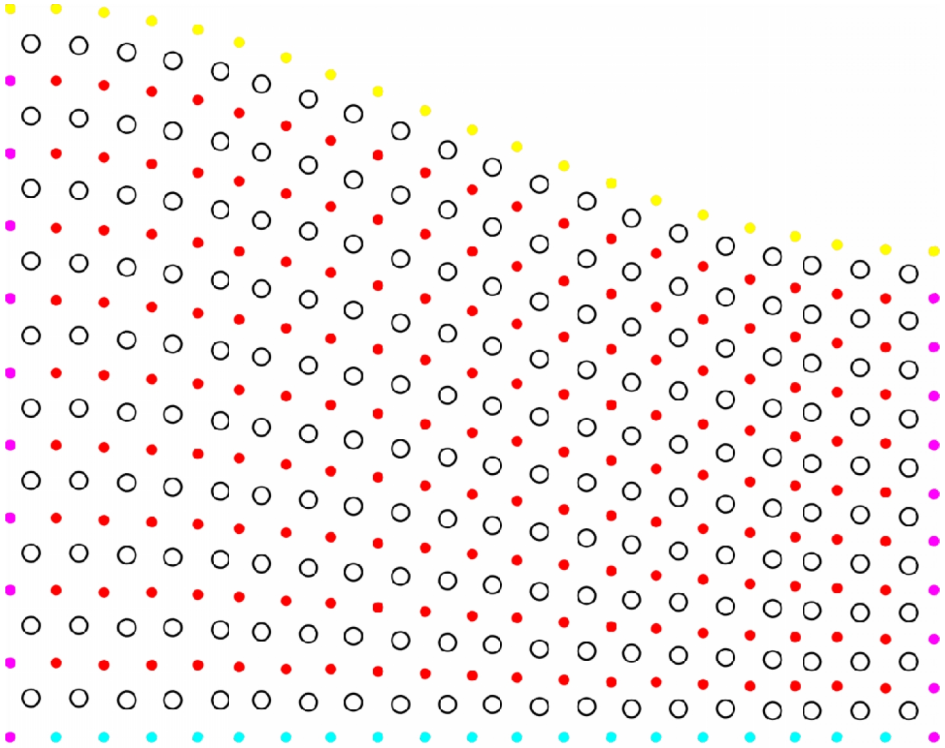

Figure A.5. Sample Nodal Layout Showing RBF Centers (circles) separated from the Collocation Centers (dots)

It was observed that this method of approach did not worsen the results, in fact added flexibility when choosing the location of the RBF centers for optimum performance.

Different examined cases were putting the RBF centers in the middle of the collocation centers, concentrating the RBF centers near the boundaries, or completely locating the RBF centers outside the computational domain. Out of these methods, the approach of RBF center concentration near the surface was observed to yield better results for our analyses.

A.4. Shape Parameter Optimization

Global shape parameters were used in this study; the same shape parameter was used for all of the RBF centers. However, it was necessary to update the global shape

parameter at every time step. Our first approach on this was to calculate a minimum internodal distance $d_{\min}$ at every time step, and then to use the global shape parameter as a multiple σ of this number. So in our models $c = \sigma d_{\min}$. Choice of σ was based on a trial and error approach, and a constant σ was used throughout the runs.

A more sophisticated approach to improve this method was to periodically optimize σ. This was achieved by estimating a known value from the problem using a range of different σ values. The estimations were compared to the known values, and the σ value yielding the least error was chosen as the optimum σ.

The known value that was estimated was the Laplacians of the velocity potential inside the domain, which would be equal to zero.

It was observed that performing this optimization every 5000th to 10000th time step had significant positive effects on the results. Optimizing too rarely affected the model stability and too frequently added to the computational cost of the model.

An approach developed to take this further was to place nodes on the boundary, and remove all the interior nodes. PDECB procedure was used to use the GE on the boundaries, and σ optimization was performed by minimizing the error for the GE estimation inside domain. This procedure yielded very fast and stable models, but an intense research is required to maintain accuracy in high amplitude sloshing models.

A.5. Varying the Number of RBF and Collocation Centers

Wu and Chang (2011) state that errors on the estimation of high order derivatives on the boundaries was due to Over Fitting phenomenon, and means to control these errors was to reduce the number of RBFs. It was decided to use the same approach and play with the number of RBF centers that were used in the models.

Having different number of RBF and collocation points in the model results in a non-square system matrix F. Supposing there are n_{rbf} number of RBF centers and n_{coll} number of collocation centers, re will be n_{rbf} number of columns and n_{coll} number of rows in the system matrix.

$$\begin{bmatrix} f_{11} & \cdots & f_{1n_{rbf}} \\ \vdots & \cdots & \vdots \\ f_{n_{coll}1} & \cdots & f_{n_{coll}n_{rbf}} \end{bmatrix} \begin{Bmatrix} \alpha_1 \\ \vdots \\ \alpha_{n_{rbf}} \end{Bmatrix} = \begin{Bmatrix} s_1 \\ \vdots \\ s_{n_{coll}} \end{Bmatrix} \tag{A.2}$$

Solving such a system is possible by the Least Squares approach, which was a built in functionality in MATLAB.

The observation was that the least squares approach was able to filter the instabilities near the boundary. However, there was also the danger of filtering out the valuable nonlinear behavior of the system during the process. It was observed that when n_{rbf} became less than 80% of the n_{coll}, the system started to output smoother but inaccurate results. Therefore caution is required to select the number of nodes present in the model.

Same approach was used for estimating the derivatives of the η on the free surface boundary, and for smoothing up the η values. The optimum frequency of performing this procedure was found to be every 1000th to 2000th time step.

A.6. Mass Conservation Correction

A method experimented in the studies was to keep track of the fluid volume and to periodically correct the fluid volume by scaling the surface amplitudes. A method similar to that used in Chen *et al.* (2012) is experimented. The scaling factor was calculated by first calculating the volume ratio θ:

$$\theta = 1 + \frac{1}{n}\frac{(V_0 - V_1)}{V_0}$$

where V_1 is the present and V_0 is the initial volume, n is a constant. The mass correction was performed by taking the free surface heights relative to the tank bottom, and scaling them with θ.

Using such a scheme produced better mass conservation, but not necessarily improved the results. That is because there are many other problem variables and numerical parameters that contribute to mass conservation errors. Further research is required to come up with a scheme that enforces mass conservation by controlling all these variables. In Chen *et al.* (2012), a scheme specific to multi-scaling Trefftz Method is developed and decent increases in accuracy are obtained.

In the present study, this scheme was used only on the very high amplitude resonant sloshing case, which had the most mass conservation error. Parameter n was taken to be 20, and was applied every 1000th time step. This effort reduced the mass conservation from 3.5% to 1.5% in the end of the runs. An increase in the parameter n gave better mass conservation, but decreased the accuracy of th results.

REFERENCES

Abramson, H. N., 1966, *The Dynamic Behavior of Liquids in Moving Containers With Applications to Space Vehicle Technology*, National Aeronautics And Space Administration, Washington, D.C.

Armenio, V., M. La Rocca, 1996, "On the Analysis of Sloshing of Water in Rectangular Containers: Numerical Study and Experimental Validation", *Ocean Engineering,* Vol. 23, No. 8, pp. 705-739.

Benjamin, T. B., F. Ursell, 1954, "The Stability of the Plane Free Surface of a Liquid in a Vertical Periodic Motion", *Proceedings of the Royal Society (London)*, Series A, No. 225, pp. 505–515.

Bernal, F, M. Kindelan, 2007, "RBF Meshless Modeling of Non-Newtonian Hele-Shaw Flow", *Engineering Analysis with Boundary Elements*, Vol. 31, pp. 863-874.

Bernal, F, G. Gutierrez, M. Kindelan, 2009, "Use of Singularity Capturing Functions in the Solution of Problems With Discontinuous Boundary Conditions", *Engineering Analysis with Boundary Elements*, Vol. 33, pp. 200-208.

Bernal F., M. Kindelan. 2009, "On the Enriched RBF Method for Singular Potential Problems", *Engineering Analysis with Boundary Elements*, Vol. 33, pp. 1062-1073.

Bishop, C., 1991, "Improving the Generalization Properties of Radial Basis Function Neural Networks", *Neural Computation*, Vol. 3, pp. 579–588.

Brown, D. L. Ling, E. Kansa, J. Levesley, 2005, "On Approximate Cardinal Preconditioning Methods for Solving PDEs with Radial Basis Functions", *Engineering Analysis with Boundary Elements*, Vol. 29, No. 4, pp. 343–353.

Buhmann, M. D., 2003, *Radial Basis Functions*, Cambridge University Press, Cambridge.

Carlson, R. E., and T. A. Foley, 1991, "The Parameter R2 in Multiquadric Interpolation", *Computers and Mathematics with Applications*, Vol. 21, pp. 29-42.

Celebi, M., H. Akyildiz, 2002, "Nonlinear Modelling of Liquid Sloshing in a Moving Rectangular Tank", *Ocean Engineering*, Vol. 29, pp. 1527-1553.

Chen, B. F, H. W. Chiang, 1999, "Complete 2D and Fully Nonlinear Analysis of Ideal Fluid In Tanks", *Journal of Engineering Mechanics*, Vol. 125, pp. 70-78.

Chen, B. F, 2005, "Viscous Fluid in Tank under Coupled Surge, Heave, and Pitch Motions", *Journal of Waterway, Port, Coastal and Ocean Engineering*, Vol. 131, No. 5, pp. 239-256.

Chen Y. W, W. C. Yeih, C. S. Liu, J. R. Chang, 2012, "Numerical Simulation of the Two-Dimensional Sloshing Problem Using a Multi-scaling Trefftz Method", *Engineering Analysis with Boundary Elements*, Vol. 36, pp. 9-29.

Cheng, A. H. D., M. A. Golberg, E. J. Kansa, G. Zammito, 2003, "Exponential Convergence and H-C Multiquadric Collocation Method for Partial Differential Equations", *Numerical Methods for Partial Differential Equations*, Vol. 19, No. 5, pp. 571–594.

Dean, R.G., P.S. Eagleson, 1966, "*Small Amplitude Wave Theory*", In A. Ippen (Editor), 1966, *Estuary and Coastline Hydrodynamics,* McGraw-Hill Book Co*.,* New York.

Erginbas, C., 2009, *Experimental Sloshing*, B.S. Thesis, Bogazici University.

Faltinsen O. M., 1978, "A Numerical Nonlinear Method of Sloshing In Tanks With Two-Dimensional Flow*", Journal of Ship Research,* Vol. 22, pp. 193–202.

Faltinsen, O. M., O. F. Rognebakke, I. A. Lukovsky, and A. N. Timokha, 2000, "Multidimensional Modal Analysis of Nonlinear Sloshing in a Rectangular Tank with Finite Water Depth", *Journal of Fluid Mechanics*, Vol. 407, pp. 201-234.

Faltinsen, O. M., O. F. Rognebakke, A. N. Timokha, 2003, "Resonant Three-dimensional Nonlinear Sloshing in a Square-base Basin", *Journal of Fluid Mechanics*, Vol. 487, pp. 1-42.

Faltinsen O. M., A.N. Timokha, 2009, *Sloshing*, Cambridge University Press, Cambridge.

Fang H., M. Rais Rohani, Z. Liu, M.F. Horstemeyer, 2005, "A Comparative Study of Metamodeling Methods for Multiobjective Crashworthiness Optimization", *Computers & Structures,* Vol. 83, No. 25–26, pp. 2121–2136.

Fang H., M.F. Horstemeyer, 2006, "Global Response Approximation with Radial Basis Functions", *Engineering Optimization,* Vol. 38, No. 4.

Fasshauer G. E., 1996, "Solving Partial Differential Equations by Collocation with Radial Basis Functions", in: *Me´chaute´ A.L. (Ed.), Proceedings of Chamonix*, Vanderbilt University Press, Nashville, TN.

Fasshauer, G., 2007, *Meshfree Approximation Methods with MATLAB*, World Scientific Publishers, Singapore.

Fedoseyev, A. I., Friedman, M. J., Kansa, E. J., 2002, "Improved Multiquadric Method for Elliptic Partial Differential Equations via PDE Collocation on the Boundary", *Computers and Mathematics with Applications*, Vol. 43, pp. 439-455.

Franke, R., 1982, "Scattered Data Interpolation: Tests of Some Methods", *Mathematics of Computation*, Vol. 38, No. 157, pp. 181-200.

Franke, C., R. Schaback, 1998, “Convergence Order Estimates of Meshless Collocation Methods Using Radial Basis Functions”, *Advances in Computational Mathematics*, Vol. 8, Number 4, pp. 381-399.

Fornberg, B. T. A. Driscoll, G. Wright, R. Charles, 2002, “Observations on the Behavior of Radial Basis Function Approximations Near Boundaries”, *Computers and Mathematics with Applications*, Vol. 43, pp. 473-490.

Fornberg, B, J. Zuev, 2007, “The Runge Phenomenon and Spatially Variable Shape Parameters in Rbf Interpolation”, *Computers & Mathematics with Applications*, Vol. 54, No. 3, pp. 379-398.

Frandsen, J. B., 2004, “Sloshing Motion in Excited Tanks”, *Journal of Computational Physics*, Vol. 196, pp. 53-87.

Frandsen, J. B. and A. G. L. Borthwick, 2003, “Simulation of Sloshing Motions in Fixed and Vertically Excited Containers Using a 2-D Inviscid Sigma-Transformed Finite Difference Solver”, *Journal of Fluids and Structures*, Vol. 18, pp. 197-214.

Fujii, K., Y. Tamura, T. Sato and T. Wakahara, 1990, "Wind-induced Vibration of Tower and Practical Applications of Tuned Sloshing Damper", *Journal of Wind Engineering and Industrial Aerodynamics,* Vol. 33, No. 1-2, pp. 263-272.

Gockel, M., 1977, *The Implementation of Fluid Capability in Nastran*, The Macneal-Schwendler Corporation, Los Angeles, California.

Goldberg, M. A., and C. S. Chen, 1997, *Discrete Projection Methods for Integral Equation*, Computational Mechanics Publications, Southampton.

Hardy, L. R., 1971, “Multiquadric Equations of Topography and Other Irregular Surfaces”, *Journal of Geophysical Research*, Vol. 76, pp. 1905-1915.

Hirt, C.W, B. D. Nichols, 1981, "Volume of Fluid (VOF) Method for the Dynamics of Free Boundaries", *Journal of Computational Physics*, Vol. 39, No. 1, pp. 201-225.

Hon, Y. C. and X. Z. Mao, 1997, "A Multiquadric Interpolation Method for Solving Initial Value Problems", *Sci. Comput*., Vol. 12, pp. 51-55.

Hon, Y. C., and X. Z. Mao, 1998, "An Efficient Numerical Scheme for Burgers' Equation", *Applied Mathematics and Computation*, Vol. 95, pp. 37–50.

Hon, Y. C., K. F. Cheung, X. Z. Mao, and E. J. Kansa, 1999, "Multiquadric Solution for Shallow Water Equations", *Journal of Hydraulic Engineering ASCE*, Vol. 125, pp. 524-533.

Hutton R. E., 1962, *An Investigation of Resonance, Nonlinear and Nonplanar Free Surface Oscillations of Fluid*, Ph.D. Thesis, University of California in Los Angeles.

Ibrahim, R. A, 2005, *Liquid Sloshing Dynamics, Theory and Applications*, Cambridge University Press, New York.

Jacobsen, L. S., R. Ayre, 1951, "Hydrodynamic Experiments with Rigid Cylindrical Tanks Subjected to Transient Motions", *Bulletin of the Seismological Society of America*, Vol. 41, pp. 313- 346.

Jeffreys, H., 1924, "The Free Oscillations of Water in an Elliptical Lake", *Proceedings of London Math*ematical *Soc*iety, Vol. 23.

Moiseev N. N., 1958, "On the Theory of Nonlinear Vibration of a Liquid of Finite Volume", *Journal of Applied Mathematics and Mechanics*, Vol. 22, pp. 612–621.

Kansa, E. J, 1985, "Application of Hardy's Multiquadric Interpolation to Hydrodynamics", In: *Society for Computer Simulation (SCS) multiconference*, San Diego, CA, USA, 23 Jan 1986, Lawrence Livermore National Laboratory, Ca.

Kansa, E. J., 1990a, “Multiquadrics – A Scattered Data Approximation Scheme with Applications to Computational Fluid Dynamics I: Surface Approximations and Partial Derivative Estimates”, *Computers and Mathematics with Applications*, Vol. 19, pp. 127-146.

Kansa, E. J., 1990b, “Multiquadrics – A Scattered Data Approximation Scheme With Applications to Computational Fluid Dynamics II: Solutions of Parabolic, Hyperbolic and Elliptic Partial Differential Equations”, *Computers and Mathematics with Applications*, Vol. 19, pp. 147-161.

Lamb, S. H., 1879, *Hydrodynamics*, Cambridge University Press, Cambridge.

Lamb, S. H., 1934, *Hydrodynamics*, Sixth Edition, Cambridge University Press, Cambridge.

Larsson, E., K. Ahlander, A. Hall, 2008, "Multi-dimensional option pricing using radial basis functions and the generalized Fourier transform", *Journal of Computational and Applied Mathematics*, Vol. 222 pp. 175–192.

Liu, D., P. Lin, 2008, “A Numerical Study of Three-dimensional Liquid Sloshing in Tanks”, *Journal of Computational Physics*, Vol. 227, pp. 3921-3939.

Madych, W. R., Nelson S. A., 1990, “Multivariate Interpolation and Conditionally Positive Definite Functions. II”, *Mathematics of Computation*, Vol. 54, No. 189, pp. 211-230.

Madych, W. R., 1992, “Miscellaneous Error Bounds for Multiquadricand Related Interpolants”. *Computers Math. with Applications*, Vol. 24, pp. 121-138.

Nakayama, T. and K. Washizu, 1981, “Nonlinear Analysis of Liquid Motion in a Container Subjected to Forced Pitching Oscillation”, *International Journal for Numerical Methods in Engineering*, Vol. 15 pp. 1207-1220.

Nakayama, T. and K. Washizu, 1981, “The Boundary Element Method Applied to the Analysis of Two-Dimensional Nonlinear Sloshing Problems”, *International Journal for Numerical Methods in Engineering*, Vol. 17, pp. 1631-1646.

Nguyen, V. P., T. Rabczukb, S. Bordasc, M. Duflotd, 2008, “Meshless Methods: a Review and Computer Implementation Aspects“, *Mathematics and Computers in Simulation,* Vol. 79, No. 3, pp. 763-813.

Ockendon, H. and J. R. Ockendon, 1973, “Resonant Surface Waves”, *Journal of Fluid Mechanics*, Vol. 59, Part 2, pp. 397-413.

Pal, P., S. K. Bhattacharyya, 2010, “Sloshing in partially filled liquid containers – Numerical And Experimental Study for 2-D Problems”, *Journal of Sound and Vibration*, Vol. 329, pp. 4466-4485.

Stoker, J.J, 1957, *Water waves, the Mathematical Theory With Applications*, Interscience Publishers, New York.

Tarwater, A. E., 1985, “Parameter Study of Hardy's Multiquadric Method for Scattered Data Interpolation”, *Technical report UCRL-54670*, Lawrence Livermore Nationaln Laboratory.

Viana S.A, D. Rodger, H. C. Lai., 2007, "Overview of Meshless Methods", *International Compumag Society Newsletter*, Vol. 14, pp. 3-6.

Vrankar, L., E.J. Kansa, L. Ling, F. Runovc, G. Turk, 2010, “Moving-boundary Problems Solved by Adaptive Radial Basis Functions”, *Computers & Fluids*, Vol. 39, pp. 1480-1490.

Waller, M. D., 1938, “Vibrations of free circular plates. Part 1: Normal modes”, *Proceedings of the Physical Society of London,* Vol 50, pp. 70-76.

Wendland, H., 2004, *Scattered Data Approximation*, Cambridge University Press, New York.

Wu, Z., 1992, "Hermite–Birkhoff Interpolation of Scattered Data by Radial BasisFunctions", *Journal of Approximation Theory*, Vol. 8, No. 2, pp. 1-11.

Wu, G.X., Q. W. Ma, and R. E. Taylor, 1998, "Numerical Simulation of Sloshing Waves in 3d Tank Based on a Finite Element Method", *Applied Ocean Research,* Vol. 20, pp. 337–355.

Wu, Z. and Y. C. Hon, 2003, "Convergence Error Estimate in Solving Free Boundary Diffusion Problem by Radial Basis Functions Method", *Engineering Analysis with Boundary Elements*, Vol. 27, pp. 73-79.

Wu, N.J, T. K. Tsay, D. L. Young, 2006, "Meshless Numerical Simulation for Fully Nonlinear Water Waves", *International Journal for Numerical Methods in Fluids*, Vol. 50, No. 2, pp. 219-234.

Wu. G. X., 2007, "Second-order Resonance of Sloshing in a Tank", *Ocean Engineering*, Vol. 37, pp. 2345–2349.

Wu, N. J, K. A. Chang, 2011, "Simulation of Free-surface Waves in Liquid Sloshing Using a Domain-type Meshless Method", *International Journal for Numerical Methods in Fluids*, Vol. 27, no. 3, pp. 269-288.

Wong S.M, Y.C. Hon, M.A. Golberg, 2002, "Compactly Supported Radial Basis Functions for Shallow water Equations", *Applied Mathematics and Computation*, Vol. 127, No. 1, pp. 79–101.

Zerroukat, M., H. Power, and C. S. Chen, 1998, "A Numerical Method for Heat Transfer Problems Using Collocation and Radial Basis Function*", International Journal for Numerical Methods in Engineering*, Vol. 42, pp. 1263-1278.